



Escola de Camins
Escola Tècnica Superior d'Enginyeria de Camins, Canals i Ports
UPC BARCELONATECH

SHM with DOFS of the TMB L-9 tunnel affected by nearby building construction

Treball realitzat per:

Judit Gómez i Esteve

Dirigit per:

Joan Ramon Casas Rius

Sergi Villalba Herrero

Màster en:

Enginyeria de Camins, Canals i Ports

Barcelona, 14 de juny de 2018

Departament d'Enginyeria Civil i Ambiental

TREBALL FINAL DE MÀSTER

Acknowledgements

First of all, I would like to express my sincere gratitude to master thesis director Prof. Joan Ramon Casas for proposing the interesting case study that this project presents and providing me with helpful knowledge and advice throughout the whole year. I also wish to thank external tutor Dr. Sergi Villalba, from Cotca S.A., for providing me access to all the necessary data regarding the case study, which was his own project, and for his insightful comments and recommendations.

I would also like to thank Vicente Alegre and the company Cotca S.A. itself, responsible of the monitoring case study that this thesis presents, for giving me the opportunity to participate in this project and for making the necessary arrangements to grant me access to the tunnel. The site visit was very much enriching and helpful regarding the understanding of the case study that this thesis presents since it allowed me to observe the DOFSs deployment and the data collection process at first hand.

A very special gratitude goes out to PhD student Mattia F. Bado, for giving me advice and ideas, offering to revise my work and allowing me to take part in his own research. Additionally, I want to thank the now Dr. António Barrias for introducing me to the fiber optic sensing field at the very beginning of this thesis.

I am very grateful to my boyfriend Lucas, who is also a MECCP student and presented his thesis at the same time as me, for his endless help and support. Those whole days and late nights redacting wouldn't have been the same without you by my side.

A special mention goes to my friend Pere for solving all my questions regarding Matlab coding.

Finally and very importantly, I am grateful to my family, who have provided me with the needed moral and emotional support through my whole life. To my parents Maria Àngels and Oriol, for affording my studies and for always making it clear that everything was going to be alright while also pushing me to achieve my goals. To my brother Miquel, who provided the required technical support by lending me his brand new computer screen, drawing in AutoCAD wouldn't have been that easy without it, and to my sister Júlia, for always 'brutally' encouraging me. To my grandparents, Isabel and Josep, for those long construction conversations sitting on their green sofa and for the eventual phone calls checking on me and telling me '*Ja falta poc!*'.

To all of you, thank you.

Abstract

This Final Master Thesis addresses the implementation of a Distributed Optical Fiber Sensor system (DOFS) to the TMB L-9 metro tunnel in Barcelona for Structural Health Monitoring (SHM) purposes as the former could potentially be affected by the construction of a nearby residential building. With this aim and the one of assessing the performance of this newly developed monitoring technology, an in-depth study on the collected strain readings is performed along with the development of innovative data post-processing techniques. Furthermore, the reliability of the installed DOFS system is studied by means of a comparison with a theoretical representative of the site's structural conditions. Finally, a new convergence computation methodology based on strain measurements and extracted from the Navier-Bresse system of equations regarding mechanics of deformable solids is proposed and evaluated.

Keywords: structural health monitoring; distributed fiber sensing; optical fiber; tunnel monitoring; civil engineering; convergence computation

Resum

Aquest Treball Final de Màster aborda la implementació de Sensors de Fibra Òptica Distribuïda (DOFS) per a la Monitorització de Salut Estructural (Structural Health Management, SHM) en el cas específic del túnel de la línia de metro L-9 de TMB a Barcelona que es troba potencialment afectat per la construcció d'un edifici a les proximitats del seu traçat. Amb l'objectiu d'avaluar l'eficiència d'aquesta nova tecnologia es duu a terme un estudi exhaustiu de les lectures recollides del qual s'extreu una tècnica per post-processar les dades on s'eliminen les mesures de deformació anòmales (Strain Reading Anomalies, SRAs) presents. La fiabilitat del sistema de DOFS instal·lat es demostra per mitjà d'una comparació amb models estructurals teòrics. Finalment, es proposa i s'avalua una nova metodologia per a l'obtenció de la convergència de la secció del túnel a partir de les mesures de deformació del seu contorn i basada en les equacions de Navier-Bresse en mecànica de sòlids deformables.

Paraules clau: monitorització de la salut estructural; sensors de fibra òptica distribuïda; fibra òptica; monitorització de túnel; enginyeria civil; càlcul de convergència

Resumen

Este Trabajo Final de Máster aborda la implementación de Sensores de Fibra Óptica Distribuida (DOFS) para la Monitorización de Salud Estructural (Structural Health Management, SHM) en el caso específico del túnel de la línea de metro L-9 de TMB en Barcelona que se encuentra potencialmente afectado por la construcción de un edificio en las proximidades de su trazado. Con el objetivo de evaluar la eficiencia de esta nueva tecnología se lleva a cabo un estudio exhaustivo de las lecturas recogidas del cual se extrae una técnica para post-procesar los datos en la que se eliminan las medidas de deformación anómalas (Strain Reading Anomalies, SRAs) presentes. La fiabilidad del sistema de DOFS instalado se demuestra por medio de una comparación con modelos estructurales teóricos. Finalmente, se propone i evalúa una nueva metodología para la obtención de la convergencia de la sección del túnel a partir de las medidas de deformación de su contorno y basada en las ecuaciones de Navier-Bresse en mecánica de sólidos deformables.

Palabras clave: monitorización de la salud estructural; sensores de fibra óptica distribuïda; fibra òptica; monitorización de túnel; ingeniería civil; cálculo de convergencia

Index

Summary of the thesis	1
1. Literature review	2
1.1. Introduction to SHM	2
1.1.1. Motivation for SHM.....	2
1.1.2. Existing SHM technologies.....	5
1.1.2.1. Specific SHM for tunnels.....	6
1.1.3. Issues of the conventional SHM technologies	8
1.1.4. Latest innovations in SHM sensors	9
1.2. Optical Fiber Sensors	11
1.2.1. Basics of OFS.....	11
1.2.2. Classification of OFS	12
1.2.3. Distributed Optical Fiber Sensors	14
1.2.3.1. Scattering.....	14
1.2.3.2. Reflectometry techniques	16
1.2.3.4. DOFS applied in civil engineering.....	17
1.2.3.5. DOFS applied in tunnels	20
1.2.3.5. Summary of DOFS advantages and limitations	26
2. Objectives.....	28
3. Case study: DOFS installation in L-9	29
3.1. Project description.....	29
3.2. Objectives of the SHM.....	32
3.3. Monitoring scheme and sensor installation	32
3.3.1. Monitoring scheme.....	33
3.3.2. DOFS installation.....	34
3.4. Construction timeline and monitoring period	37
3.5. Data collection: reading software and DOFS measurements	41
4. DOFS strain readings post-processing	45
4.1. Peak analysis	45
4.2. Strain Reading Anomalies (SRAs).....	49
4.2.1. Types of anomalies.....	50
4.2.2. Anomalies post-processing	53
4.2.2.1. Detection of anomalies.....	53
4.2.2.2. Removal of SRAs.....	56
4.2.2.3. Substitution by interpolation	60

4.3. Final post-processing algorithm.....	64
5. Displacements computation from DOFS strain readings	66
5.1. Theoretical background.....	66
5.1.2. Strain	66
5.1.2. Curvature.....	67
5.1.3. Rotations and displacements	68
5.1.4. Cylindrical coordinates	71
5.1.5. Approximation by Riemann	74
5.1.6. Final system of equations.....	75
5.2. Algorithm for displacement computation.....	77
6. Results and discussion.....	79
6.1. Expected structural effects	79
6.1.1. Unloading model.....	79
6.1.2. Loading model.....	81
6.1.3. Conclusive ideas.....	82
6.2. Observed behaviour of the section and reference points.....	82
6.2.1. Strains.....	82
6.2.1.1. 3Ds. Global analysis.....	82
6.2.1.2. 2Ds. Representative points	89
6.2.2. Displacements	93
7. Conclusions	99
7.1. Case study	99
7.1.1. DOFS performance	99
7.1.2. Displacement computation.....	100
7.1.3. Tunnel monitoring project.....	101
7.2. DOFS technology applied on real structures.....	101
7.3. SHM	102
7.4. Further research proposal	102
8. References	104
Annexes.....	109

Index of figures

Figure 1. Annual cost of infrastructure construction and maintenance in Europe (from [2])	2
Figure 2. Mianus River Bridge Collapse (from [3]).....	3
Figure 3. Injaka bridge collapse a) before and b) after (Mpumalanga, 1998) (from [4]).....	3
Figure 4. Small but timely renewal investments save money (from [6])	4
Figure 5. Need for instrumentation regarding tunnel structures (from [13]).....	6
Figure 6. Extensometric wire for tunnel monitoring (from [16])	7
Figure 7. Laser scanning of excavation surface of tunnel (from [17])	7
Figure 8. Punctual displacement measuring devices a) extensometer [18], b) inclinometer [18] and b) crackmeter [19]	8
Figure 9. Monitoring of a pedestrian bridge under different excitation events by means of GPS receivers (from [21])	9
Figure 10. Schematic idea on multi-image stitching and scene reconstruction (from [22]).....	9
Figure 11. Wireless tilt meters installed on cast iron tunnel segments before grouting works (from [23]).....	10
Figure 12. Structure of a typical optical fiber: 1. Core (5-10 μm), 2. Cladding (125 μm) and 3. Buffer or coating(250-900 μm)	12
Figure 13. Light guiding and total internal refraction in a multi-modal optical fiber (from [31])	12
Figure 14. Overview of fiber optic sensor technologies (from [11]).....	12
Figure 15. Spatial distribution detection of cracks with a) point OFS and b) distributed OFS (from [39]).....	13
Figure 16. Comparison between the use of point OFS (top) and distributed OFS (bottom) (from [39]).....	13
Figure 17. Typical DOFS measuring system (from [41])	14
Figure 18. Size comparison between optical fiber and traditional foil strain gauge (from [41])	14
Figure 19. Scattering and backscattering of light in an optical fiber core (from [20]).....	15
Figure 20. Wavelengths of the backscattered radiation (from [42]).....	15
Figure 21. Principle OTDR based on Rayleigh backscattering read by the Fiber Under Test (FUT) (from [30])	16
Figure 22. Luzzone dam in the Swiss Alps (from [53]).....	18
Figure 23. View of Götaälvbron (from [55]).....	18
Figure 24. Viaduct Road BP-1413 in Cerdanyola del Vallès (Barcelona) (from [49]).....	19
Figure 25. Deployed OBR system in Sarajevo Bridge (Barcelona) (from [46])	19
Figure 26. Positioning of OBR system in concrete cooling tower (from [49])	19

Figure 27. Sant Pau Hospital’s masonry vaults monitoring (from [46]).....	20
Figure 28. Optical fiber cable instrumentation at Royal Mail tunnel (from [59]).....	21
Figure 29. Plot of cumulative change in strain for ring R2950 at various construction stages (from [59]).....	21
Figure 30. Results of strain measurements on the Shinkansen tunnel (from [60]).....	22
Figure 31. Structure of the tunnel in Žilina (from [61]).....	22
Figure 32. Optical fiber implementation on iron bars of the braced girder on the primary lining (from [61]).....	23
Figure 33. Measurement of Brillouin frequency from 6 measurements (from [61]).....	23
Figure 34. FBG strain sensors location (from [62])	24
Figure 35. Change of strains at early construction stage of different local sensors (from [62])	24
Figure 36. Proposed radial displacement (δ) (from [14]).....	25
Figure 37. Laboratory experiment on convergence computation a) The reaction frame with connected metallic ring and inner reference sensors and b) detail of the sensors: 1. soldered cable and 2. glued cable (from [15])	25
Figure 38. Results on steel ring monitoring: a) orthoradial strain measures provided by glued sensors and Brillouin scattering and b) computed convergence from DOFS strain measurements and traditional position transducer readings (from [15]).....	26
Figure 39. DOFS market forecast (from [63]).....	27
Figure 40. Building site location (red), TMB L9 layout and access station Bon Pastor (own development with base image from [64]).	29
Figure 41. Tunnel cross section.....	30
Figure 42. Schematic cross section of L9 tunnel in relation to the building	31
Figure 43. Schematic plan view of L9 tunnel in relation to the building	31
Figure 44. 3-Dimensional representation of the DOFS monitoring scheme	33
Figure 45. Plan view of DOFS location with respect to building site.....	34
Figure 46. Fiber installation pictures on a) bonding of fiber to concrete surface using epoxy resin (provided by Cotca), b) protection of the fiber in a discontinuity with bubble wrap and duct tape (provided by Cotca) and c) scratching of irregular surface due to cement grout injections prior to fiber installation (own site picture N. 018)	35
Figure 47. Tunnel monitored section (own site picture N.032).....	35
Figure 48. Selection of pictures from the installed DOFS in the tunnel (pictures provided by Cotca)	36
Figure 49. Construction time-line (adapted from data provided by Cotca S.A.)	38
Figure 50. Typical strain measurement for a particular time [from Graph window in ODiSi software].....	42
Figure 51. Introductory strain reading specifications in exported .txt file.	42

Figure 52. Exported data in the form of vectors and matrices for post-processing.....	44
Figure 53. Typical strain measurements covering the whole analyzed monitoring period	45
Figure 54. Catalogued discontinuities in tunnel cross section fiber layout (from Annex 1)	47
Figure 55. Discontinuities in longitudinal tunnel segment of fiber layout (from Annex 1).....	47
Figure 56. Peaks identifying algorithm	48
Figure 57. Particular peaks in a 20cm interval	48
Figure 58. Strain reading along fiber in 4th October (initial measurements) and 7th November	49
Figure 59. Graphical representation of SRAs' theoretical definition.....	51
Figure 60. Example on HF and HL anomalies found in real case study's measurements a) positive strains (traction) b) negative strains (compression).....	51
Figure 61. Evolution of SRAs a) 4thOctober - 7thNovember b) 4th October - 25th March.....	52
Figure 62. Graphical representation of strain raw readings between 4th October and 25th March	53
Figure 63. Strain measurements of segment 10-50m between 4th October and 17th May for different SSQ thresholds	54
Figure 64. Jumps concept to detect anomalies	55
Figure 65. Example of trend lines	59
Figure 66. Original vs Interpolated matrix for combination 1 with $SSQ < 0.30$ and jumps in time $> 50\mu\epsilon$ deleted.....	61
Figure 67. Combination 1 with $SSQ < 0.30$ and jumps in time $> 50\mu\epsilon$ deleted.....	62
Figure 68. Original vs Interpolated matrix for combination 2 with $SSQ < 30$ and jumps in space $> 50\mu\epsilon$ deleted.....	62
Figure 69. Combination 2 with $SSQ < 30$ and jumps in space $> 50\mu\epsilon$ deleted.....	63
Figure 70. Combination 3 with polynomial fit of degree 5 and error $> 10\mu\epsilon$	63
Figure 71. Final treated data set a) from below and b) from above	64
Figure 72. Treated strain data by means of trend lines.....	65
Figure 73. Representation of location i deformation.....	67
Figure 74. Relative movement between points A and B	68
Figure 75. Deformations of infinitesimal element (adapted from [71])	69
Figure 76. XY-plane element (adapted from [72]).....	69
Figure 77. Segment of fiber employed to compute displacements.....	71
Figure 78. Change from Cartesian to cylindrical coordinates (adapted from [72]).....	71
Figure 79. Definition of arbitrary angle φ_i and initial φ_0	72
Figure 80. Simply supported beam under uniformly distributed load.....	79
Figure 81. Unloading / excavation model	80

Figure 82. Unloading / excavation model detail with coordinates of fiber	80
Figure 83. Loading model	81
Figure 84. Loading model detail with fiber coordinates	81
Figure 85. Strain evolution at all times and locations (same as Figure 72).....	83
Figure 86. 3-Dimensional representation of the DOFS monitoring scheme	83
Figure 87. Plan view of strain evolution at all times and locations.....	84
Figure 88. Strain evolution in 0-8m segment	84
Figure 89. Not bonded segment	85
Figure 90. Strain evolution in 8-14m segment	86
Figure 91. 8-14m fiber segment a) comparison of segments 2 and 4 (particularization of Figure 87) and b) site picture.....	86
Figure 92. Strain evolution in 14-23m segment	87
Figure 93. 14-26m segment setup with a) detail of tunnel plan view and b) site pictures of discontinuities	87
Figure 94. Strain evolution in 23-40m segment	88
Figure 95. Strain evolution in 40-50m segment	88
Figure 96. Last meters of the fiber	89
Figure 97. Representative points in a) tunnel cross section and b) structural loading model	89
Figure 98. Strain evolution of representative points from 4th October 2018 to 17th May 2019 (original data).....	90
Figure 99. Strain evolution of representative points from 4th October 2018 to 17th May 2019 (trendlines)	90
Figure 100. Construction works completed by the beginning of March.	91
Figure 101. Relation between the three joints regarding construction time-line in a) 18th March and b) 18th April	92
Figure 102. Strain readings along transversally monitored tunnel section at different times	93
Figure 103. Radial displacements along transversally monitored tunnel section at different times for case 0.....	94
Figure 104. Tangential displacements along transversally monitored tunnel section at different times for case 0.....	94
Figure 105. Computed total displacements along transversally monitored tunnel section at different times for case 0.....	95
Figure 106. Radial displacements along transversally monitored tunnel section at different times for case A.....	95
Figure 107. Tangential displacements along transversally monitored tunnel section at different times for case A.....	96

Figure 108. Displacements along transversally monitored tunnel section at different times for case B	96
Figure 109. Displacements along transversally monitored tunnel section at different times for case C	97
Figure 110. Displacements along transversally monitored tunnel section at different times for case C with radial displacement at 40m free	98

Summary of the thesis

This Final Master Thesis addresses the implementation of the Distributed Optical Fiber Sensor systems (DOFS) to perform Structural Health Monitoring (SHM) in the specific case of the existing TMB L-9 metro tunnel in Barcelona potentially affected by a superficial building construction.

Given the case and as a result of an agreement between the concerned parties, a continuous follow-up of the tunnel's strain and tensional state is proposed to be performed during the whole construction period of the building. To do so, a monitoring scheme with DOFS attached to the tunnel section is presented and will enable to obtain the strains of the concrete lining with a resolution in the order of 1 cm.

First of all, a bibliographic review on the motivation for SHM and its currently engaged technologies will be developed focusing on their structural and civil engineering applications. The particular technologies used in tunnel monitoring will also be introduced in reference to the case study. The theoretical foundations behind optical fiber sensing and the existing sensors typologies will then be introduced together with a brief presentation of some real applications of DOFS for health monitoring of structures. In the end of this introductory section, an assessment of the aforementioned technology will be carried out through the definition of their particular issues/unreliable behaviour when applied to real structures.

After the technology introduction, the current case study will be presented in detail describing the building construction project and its relation to the tunnel outline and possible affections. The sensor installation and monitoring scheme will be described and the construction time-line will be presented and related to the monitoring period. After that, the objectives that are aimed for through the realization of this project will be introduced.

The following chapter will be devoted to the data analysis and treatment. The anomalies and noise that the collected data presents and how these have been eliminated in order to produce higher quality data will be explained. A computation of radial and tangential displacements from the measured strains will be proposed with the aim of providing convergence monitoring.

The treated data will then be presented and interpreted by means of a basic structural study and a computational 2D Finite Element model of the tunnel and construction site. The measured strains will be correlated with the construction works that were taking place at the monitoring times and the measured tendencies analysed and assessed to ensure the structure's safety proving that the readings remain inside an acceptable domain. A methodology regarding convergence of the structure based on the collected strain readings will be presented and assessed showing a new promising applicability field of the DOFS.

Finally, the relevant conclusions of this Final Master Thesis will be extracted and future research paths will be proposed for further optimization and development of the DOFSs technology.

1. Literature review

1.1. Introduction to SHM

This section will cover the main aspects characterizing the need for Structural Health Management (SHM) as well as the classic technologies used for structural monitoring finally introducing this thesis' object of study, the Distributed Optical Fiber Sensors (DOFS).

1.1.1. Motivation for SHM

As clearly stated by Brownjohn [1], civil infrastructure provides the means for a society to function. The wide range of applications that civil engineering offers includes buildings, bridges, highways, tunnels, power plants, industrial facilities, geotechnical and hydraulic structures among others. Each one of these is subjected to multiple events that deteriorate and compromise their structural integrity in a unique way throughout their service lifetime exposing their future performance to several risks.

As can be seen in Figure 1, the construction boom in Europe during the second half of the 20th century translated into a large number of aging civil structures that need to be maintained today. In addition to this, the ones that are currently being built will soon start aging and face the same fate which leads to an increasing demand for structural management.

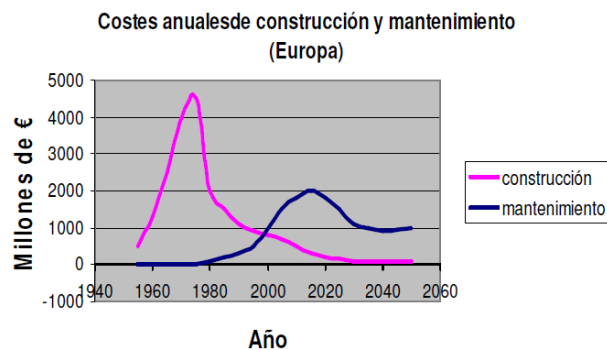


Figure 1. Annual cost of infrastructure construction and maintenance in Europe (from [2])

Aging infrastructure has significant social and economic implications, given its own gradual deterioration and the exponential increase of their service demand, which can lead to failure or even collapse if not well managed. The impact on society that a structural collapse can have is undeniable and, even more obvious, in light of recent catastrophic events such as the Ponte Morandi collapse (Genoa, Italy, 2018), the Florida International University pedestrian bridge collapse (Miami, Florida, US, 2018), the Istanbul building collapse (Istanbul, Turkey, 2019), among, unfortunately, many others.

Catastrophic events that happened due to lack of appropriate structural management are particularly serious given that there were techniques available that could have helped preventing and/or avoiding the structural collapse and the consequential human fatalities. For example, the Mianus river bridge collapse (Greenwich, Connecticut, US, 1983), where three people lost their lives and other three were injured, or the Injaka bridge collapse (Mpumalanga, South Africa, 1998), where 14 people died and 19 got injured. In particular, Mianus River bridge collapse was caused by unsatisfactory maintenance and Injaka Bridge collapse, by an ill-controlled manufacturing process. It was proven at the time that both events implied serious negligence on

the part of the management responsible personnel ignoring the structural signs warning about imminent failure.



Figure 2. Mianus River Bridge Collapse (from [3])



Figure 3. Injaka bridge collapse a) before and b) after (Mpumalangda, 1998) (from [4])

In existing infrastructure, collapse does not generally occur overnight unless it is caused by accidental extraordinary actions that the structure is not projected to endure even considering the over-dimensioning applied due to constructive and design uncertainties. These extreme accidental actions can involve collisions between the structure and high volume transports at high speed (trucks, ships or even airplanes), unexpectedly strong seismic activity or weather conditions regarding mostly wind and rain, serious calculus / project misconception, among others, all of which being highly unlikely to occur during the structure's service life, and, therefore, unaccounted for in the design phase.

All the remaining collapse causes can be avoided and/or controlled by means of appropriate SHM given that the structure will always present warning signs long before collapsing such as deflection, settlement, humidity, superficial erosion, cracks, among many others. Therefore, damage or collapse can be reverted and avoided by following the characteristic SHM phases mainly classified as: inspection, detection of structural damage, cause analysis, assessment of structural state and definition of the required course of action to reverse damaging actions and ensure safety.

A part from the logic and main reason for structural management, which is the aim for human safety, another strong reason backing it up is money. It is a fact that the current political and economic situation hinders new public infrastructure from being developed and precludes public budgets from rising up, which translates into a need for cost reduction. How structural management can help with that can be easily understood using the Sitter's "Law of Fives" [5]. The law states that every monetary unit not spent in an appropriate design of the structure or construction process will become 5 times its value when maintenance will be necessary. Again,

if this maintenance is not performed, then repairs equalling 5 times the maintenance costs will be required. And finally, if the repairs are not carried out, then renewal expenses can reach 5 times the repair costs. Therefore, 1 monetary unit will become 125 if not well managed.

A proof of how smart management through small but timely renewal investments save money at the end of the day is displayed in Figure 4. In the case of letting the asset deteriorate until it has to be replaced, \$60m are required to re-establish a good performance as opposed to the \$40m required when there has been a constant care and investment.

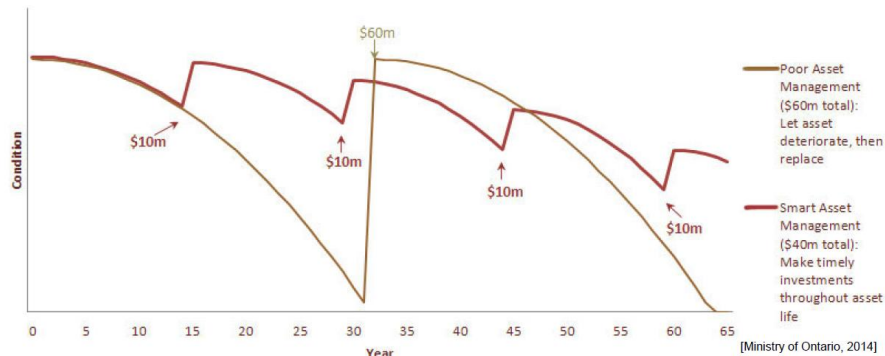


Figure 4. Small but timely renewal investments save money (from [6])

Consequently, in order to avoid catastrophe and increasing repair or replacing costs, civil structures have to endure, depending on their use, solicitations, risk and importance, among other factors, different safety and durability requirements that ensure a correct structural performance and the wellbeing of their users. With the aim of fulfilling those and in order to evaluate the structure's response under determined solicitations, a series of inspection, monitoring and maintenance protocols have to be carried out.

The effectiveness of such monitoring procedures relies in their ability to instantly detect alterations on the structure's performance, warn the involved personnel and follow the damage progress allowing for its control and prevention of further damage. A faster response allows for better in depth inspection, evaluation and, finally, determination of the course of action that minimizes the economic, social and environmental impact that the alteration may lead to. For this reason the nowadays tendency is to supplement intermittent inspection with automated, continuous and real-time monitoring technologies.

These ideas are what mainly boost the Structural Health Monitoring (SHM) research during the last decades. According to Housner et al. [7], SHM can be understood as the continuous or regular measurement and analysis of key structural and environmental parameters under operating conditions, for the purpose of warning of abnormal states or accidents at an early stage. Altogether, SHM is a damage identification strategy that provides the necessary information for a satisfactory structural maintenance.

It is interesting to mention that SHM goes further than the conventional vision of damage detection and structural diagnosis regarding the constitutive materials and the global infrastructure health. Moss and Mathews [8] and Mita [9] identified the cases where structural monitoring may be required:

- Validating modifications to an existing structure.
- Monitoring of structures affected by external works.
- Tracking long term movement or degradation of materials in critical structures.

- Providing feedback loop to improve future design based on experience.
- Assessing fatigue.
- Checking novel systems of construction and new structural forms.
- Assessing post-earthquake structural integrity.
- Enhancing effectiveness of resources as construction declines and maintenance needs increase.
- Moving towards performance-based design philosophy.

As can be seen, SHM has a very wide definition and can be implemented in different ways and cases. This enables the system to adapt its tools for performance monitoring to each unique structure and situation. However, all approaches of this strategy have common components as stated by Brownjohn [1]:

1. Structure
2. Sensors
3. Data acquisition systems
4. Data transfer and storage mechanisms
5. Database management leading to feature extraction
6. Data mining for feature extraction
7. Load/effect model development from study of data
8. Learning from past experience
9. Decision making based on identified features in combination with identified models

The main technologies that enable this system to function are described in the next chapter and the particular case study that follows it will clearly show how SHM works through these enumerated steps.

1.1.2. Existing SHM technologies

Given its objective to provide information on demand about any significant change occurring in a structure, SHM has been used for many years and can be deployed in different forms. Usually, the health evaluation of most structures, from bridges, tunnels and dams to buildings, is carried out with techniques ranging from visual observation and assessment of the structural condition to technology-led approaches.

SHM is founded in the base of robust, reliable and accurate sensing devices which are [10]:

- Inclinometers: measuring horizontal and vertical angular inclination. Usually used to monitor movement of large structures over time.
- Accelerometers: measuring acceleration and deceleration of dynamic systems. Commonly used to monitor induced acceleration and check the structural response, to check design calculations and ensure long-term safety.
- Load cells: convert forces into electrical signals and offer measurements of tensions, compression and shear forces. The majority involve precision strain gauges and are commonly used for load monitoring.

Other regularly practiced SHM approaches are based on electric strain sensors, GNS-based sensors, acoustic emission, wave propagation, etc [11].

1.1.2.1. Specific SHM for tunnels

Tunnelling activity is on the increase around the world not only in terms of work volume but also considering that the demands of modern transport networks require longer and wider tunnels than ever before through increasingly difficult ground conditions [12]. Moreover, the increasing awareness of the sensitivity of tunnels to seismic activity and the presence of tunnel length under densely populated areas require very high standards of safety. Therefore, SHM for tunnels appears to be particularly important.

Already in 1982, Dunnycliff [13] presented the conventionally required instrumentation for tunnel structural monitoring during construction and after and regarding the tunnel structure itself and its geotechnical surroundings.

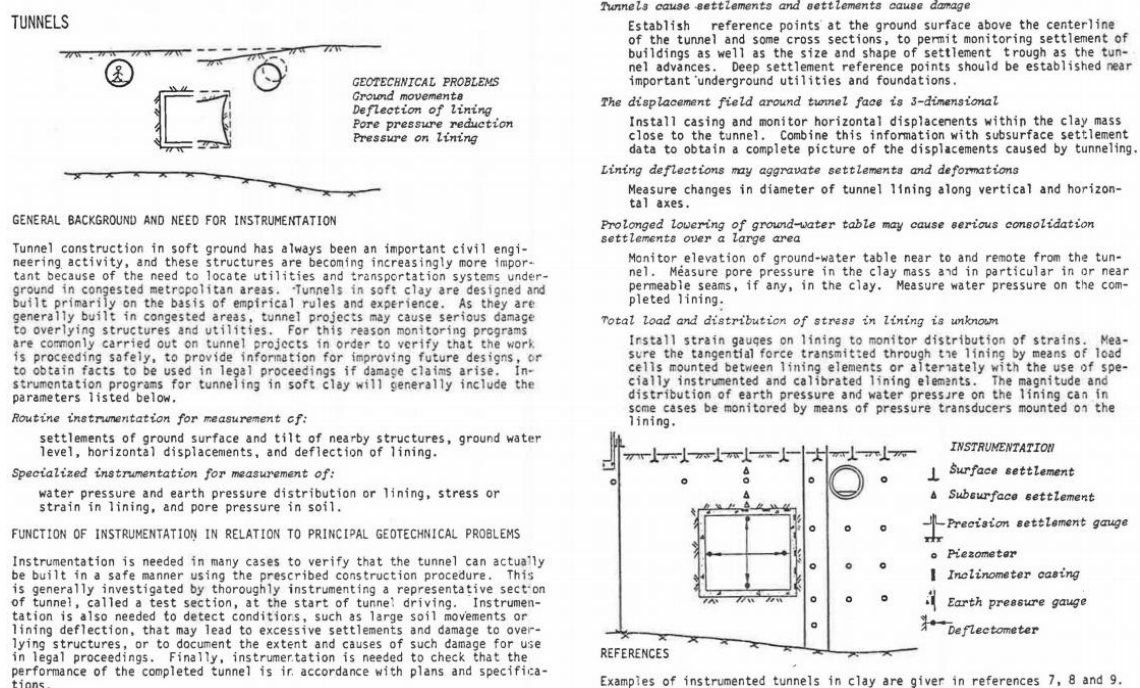


Figure 5. Need for instrumentation regarding tunnel structures (from [13])

Traditionally, the safety assessment of tunnels and underground structures, existing or under construction, focuses in ensuring safety regarding two areas: the underground structure itself and its surroundings (mainly controlled through surface monitoring). There are two possible cases in which this kind of structures would benefit from accurate monitoring: one considering the effects of the structure's construction on its surroundings and the other, looking at the structural response of the tunnel due to external actions applied in its surroundings and, consequently, on it. Both situations imply the alteration of the primary stable geotechnical balance which leads to stress concentration and redistribution that should be continuously monitored. Monitoring in these cases has to focus on both, the constructed/under construction structure and its geotechnical surroundings.

On the one hand, the structure surroundings can experience geotechnical variations that appear due to the construction of the tunnel itself (causing settlement or holes at ground level,

affections on the groundwater drainage, among others) or due to external effects (such as new ground level constructions, excessive rain periods, among others). These affections can be monitored by controlling pore pressure, earth pressure, deformation, superficial settlement, and all the factors characterizing the soil mechanics of the area. For that, a wide range of instrumentation is available: piezometers, observation wells, vibrating-wires, inclinometers, extensometers, single point monuments, heave and strain gages, among many others.

On the other hand, the structure will be subject to stress state variations both when it is being constructed and once completed due to external actions. Monitoring of the structural state of the tunnel usually consists on levelling measurements of the particular points of the tunnel or convergence measurements of the contour caused by external effects. This is usually achieved by means of optical or mechanical technologies such as extensometric wires or total station surveys [14].

Extensometric wires, also known as invar wires, are connected to opposite sides of the tunnel section at its internal surface allowing for the measurement of their elongation / compression with a 0.1mm resolution [15].

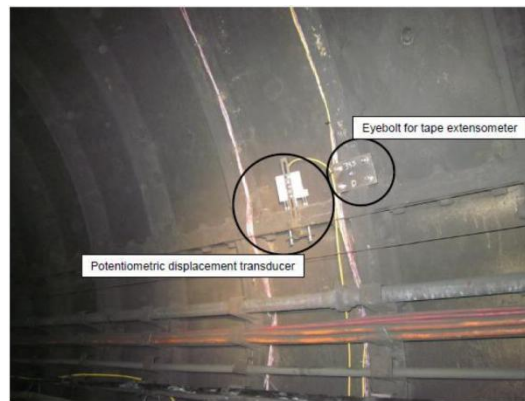


Figure 6. Extensometric wire for tunnel monitoring (from [16])

Total station surveys involve laser theodolites that allow for the acquisition of 3D scanned data on the tunnel geometry and usually focus on deformation measurement or feature extraction [17]. This technique is interesting since the change in the tunnel's profile is able to be fully characterized and the areas of the anomalous movement easily identified for posterior study.



Figure 7. Laser scanning of excavation surface of tunnel (from [17])

In Figure 8, some local tunnel monitoring tools are presented. Extensometers (a) are commonly used to punctually monitor the settlement of structures or displacements between substructures (for example, consecutive concrete lining segments). Crackmeters or fissurometers (c), being of a similar nature as the extensometers, are also used for structural monitoring since they provide insight into the time-related development of cracks, if these are present. Finally, inclinometers (b) are used, as mentioned before, to monitor angular inclinations of the tunnel inner surfaces.

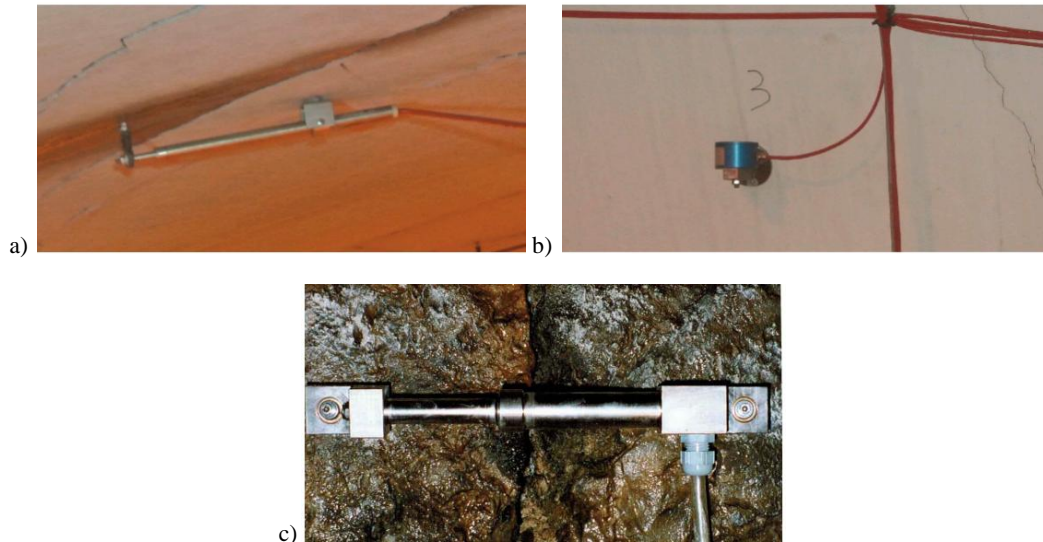


Figure 8. Punctual displacement measuring devices a) extensometer [18], b) inclinometer [18] and b) crackmeter [19]

1.1.3. Issues of the conventional SHM technologies

As stated in [10], conventional forms of inspection and monitoring are only as good as their ability to uncover potential issues in a timely manner. A clear advantage of the previously presented monitoring tools is their wide applicability, which is very useful given the uniqueness of each constructed infrastructure. However, the conventional SHM technologies present significant drawbacks that difficult structural assessment and need to be addressed.

One of the major difficulties with SHM technologies is managing the large volumes of data that the installed sensor scheme generates. Meanwhile, visual inspections and evaluations are obviously insufficient regarding the determination of the structural state of the studied infrastructure.

Another major drawback is that the mentioned monitoring schemes require, in general, the interruption of the infrastructure service or the ongoing construction /maintenance works, given their time consuming installation process, their strict installation requirements that ensure accurate readings and their significant spatial occupancy. Regarding, the measurements execution it is worth noticing that most of the conventional technologies do not involve an automated real-time measuring tool, i.e. most require specific activities every time a measurement is to be taken.

The last significant drawback is that the majority of the sensing tools developed and proven to be reliable so far, provide only localized measures and a large amount of sensors have to be installed in order to provide a global overview of the structure's condition consequently implying a major cost increase and difficult data management.

In conclusion, technological innovation regarding sensing tools and their data acquisition systems is crucial to ease structural assessment procedures in future projects regarding short and long term integrity.

1.1.4. Latest innovations in SHM sensors

Currently in the world of structural engineering, the use of recent technologies is receiving increasing acceptance to monitor a wide range of construction processes and new or aging existing structures. The service of an infrastructure that requires monitoring usually presents a significant social and economical benefit to society and becomes crucial to the appropriate development of the daily activities of the surrounding commerce and population.

The use of Fiber Optic Sensors (FOS), Global Positioning Systems (GPS), radars, MicroElectroMechanical Systems (MEMS) and Image Processing Techniques has opened the doors to the extraction of structural information that could not be acquired before [20]. Some examples of these technologies are presented in the following figures.

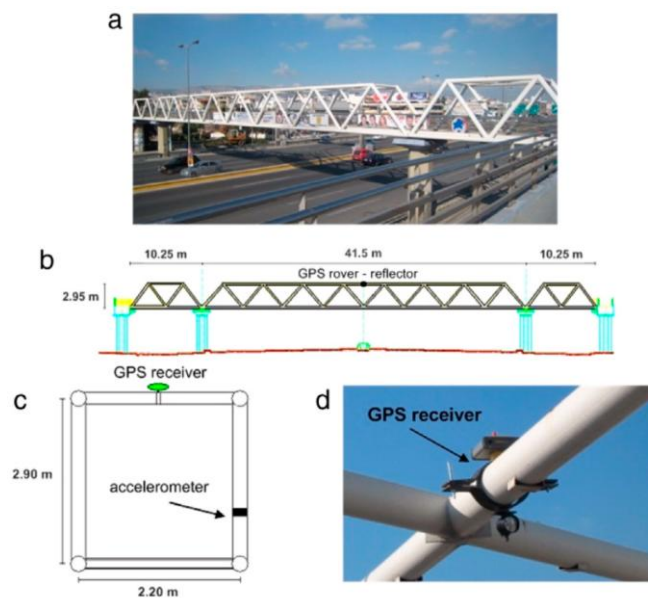


Figure 9. Monitoring of a pedestrian bridge under different excitation events by means of GPS receivers (from [21])

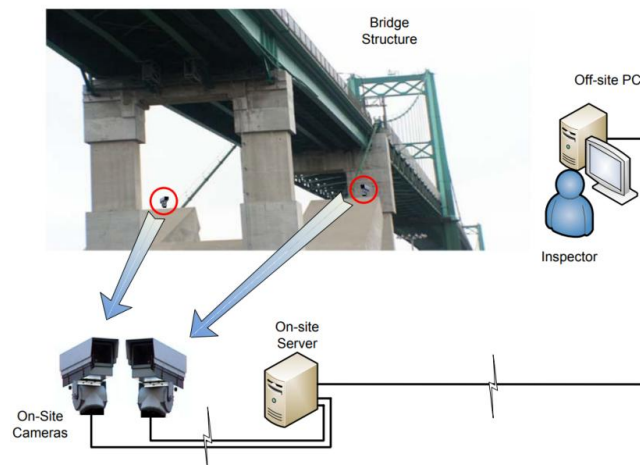


Figure 10. Schematic idea on multi-image stitching and scene reconstruction (from [22])

Regarding tunnel convergence monitoring in particular, several innovations have arisen in the last years, two examples of which are presented below.

A recent project regarding the London Underground's Jubilee line [23] in which a particular lining section experienced significant distortion due to passing through an ancient sand channel which hadn't been accounted for. This channel, completely dry during the tunnel construction in 1975, started becoming wet in 2010, causing the introduction of water and sand to the previously dried tunnel sections. In the end, the affected concrete lining segment had to be replaced and required for practical structural monitoring allowing for the execution of the replacement works. Conventional sensing technologies would imply a long installation process, significant economic requirements and a complex wires distribution that would have hindered the works. For that, Senceive's battery-powered wireless tilt meters, positioned around the cast iron segments of the tunnel lining were used to measure any rotational movement in each segment and derive from the collected data linear measurements of the lining movement.



Figure 11. Wireless tilt meters installed on cast iron tunnel segments before grouting works (from [23])

Another innovative solution to convergence monitoring is a system presented in [24] called Convergence by means of ANGular Sensors (CANG), which enables monitoring of the positions of a wire situated on the perimeter of the structure recording angles and lengths of each section of wire at all times determining the shape of the wire and the convergence values. Moreover, this system allows for minimal affections regarding use of the infrastructure and movement of personnel by freeing most of the usable cross-section. The pilot implementation of this technology was done in the Rellon road tunnel located on the *Autovía del Cantábrico* in Asturias.

As can be seen, there is a wide range of possibilities regarding monitoring technologies, either by means of conventional or innovative sensors with the possibility of combining them, to provide adequate SHM. The study of the monitored structural parameters as part of the SHM process relies crucially on the precision and resolution of the sensors and on the measuring automation and speed. Consequently, innovation and continuous improvement of the structural sensors are required to allow for easier, better and more reliable SHM deployment.

This idea of continuous innovation and improvement of SHM technologies and control processes is conceived by [25] as a way of making structures smart. This article proposes the main objectives that future research should focus on, which involve the development of three main areas: new sensitive materials to make new sensors, embedding and miniaturization technologies for sensor installation and systems for data reduction and diagnostic elaboration.

The need for technology development and automated structural data treatment that enable continuous and real-time structural monitoring with easy integrity assessment (enabling the conception of ‘smart structures’) is what encourages this research project. Focusing particularly on the Distributed Optical Fiber Sensors (DOFS) technology and studying a real application of these sensors on a tunnel, this thesis will attempt to ease the collected data interpretation and widen its applicability to convergence computation.

1.2. Optical Fiber Sensors

The first reference to Optical Fiber Sensors (OFS) dates back to the first half of the twentieth century regarding flexible endoscopes and boosting innovation in all of the medicine field [26]. After that, the development of long distance telecommunications technologies in the eighties allowed for the exponential growth of this technology from which a significant variability of sensing applications started being derived and to what we owe the modern age low-loss optical fibers [11]. The wide range of applications of this technology, from medical instrumentation and aerospace sensing to damage assessment and, consequently, structural health monitoring, ensured back then and to the present day its promising future.

Within the variety of monitoring technologies, SHM systems based on OFS have gained importance in the field during the last decades and their advantageous characteristics are becoming increasingly acknowledged.

As mentioned before, the most regularly practised SHM approaches present significant challenges in real world deployments [11]. Many sensor types can be embedded or attached to the structure, but only those based on fiber technology allow for integrated, quasi distributed or distributed measurements on or inside the structure and along extensive lengths [27]. It can be therefore stated that the main assets characterizing OFS when compared to traditional monitoring instruments are their reduced dimensions that allow for easy integration in structural components, their immunity from electromagnetic influences and chemical aggressions which significantly widens their applicability, their ability to form sensor chains using a single fiber allowing for distributed sensing and their rapid data transmission enabling real-time monitoring ([28], [29] and [30]).

1.2.1. Basics of OFS

The fundamental principle behind OFS is the propagation of light through a medium. This medium, in the case of OFS, is a cable of optical fiber which has a diameter of $125\mu\text{m}$ and its main components are the core and the cladding. Figure 12 displays the common structure of this type of cables and shows how the core, with a diameter of $5\text{-}10\mu\text{m}$, is embedded to the cladding.

Optical fibers are usually made from silica (SiO_2) and they are protected by a polymer-type material coating. The light travelling through the core is usually a monochromatic laser and it is guided through the core thanks to internal reflection: when light is travelling in the optically

dense medium that is the core and strikes a boundary at a particular angle (larger than the critical angle of the boundary), the light experiences total internal reflection and is, therefore, confined in the core (see Figure 13).

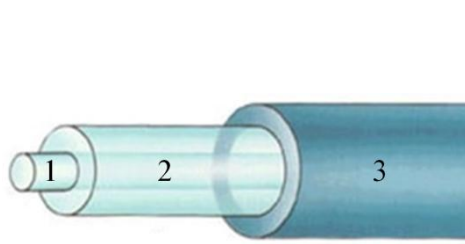


Figure 12. Structure of a typical optical fiber: 1. Core (5-10 μm), 2. Cladding (125 μm) and 3. Buffer or coating(250-900 μm)

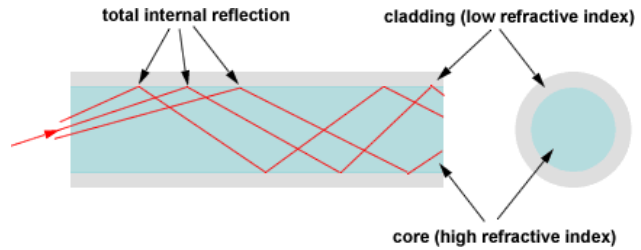


Figure 13. Light guiding and total internal refraction in a multi-modal optical fiber (from [31])

In the previously described process, attenuation is the key property of an optical fiber that affects light transmission. As stated in [11], [30] and [32], when an optical fiber is used for communication applications, attenuation has to be minimized to provide reliable signal transmission or reception. However, when it used as a sensor, attenuation has to be exploited to allow for the accurate reproduction of the external perturbations the fiber is exposed to.

1.2.2. Classification of OFS

According to [11] and [33], OFS can be categorized into three different groups: grating-based sensors, interferometric sensors and distributed sensors (see Figure 14).

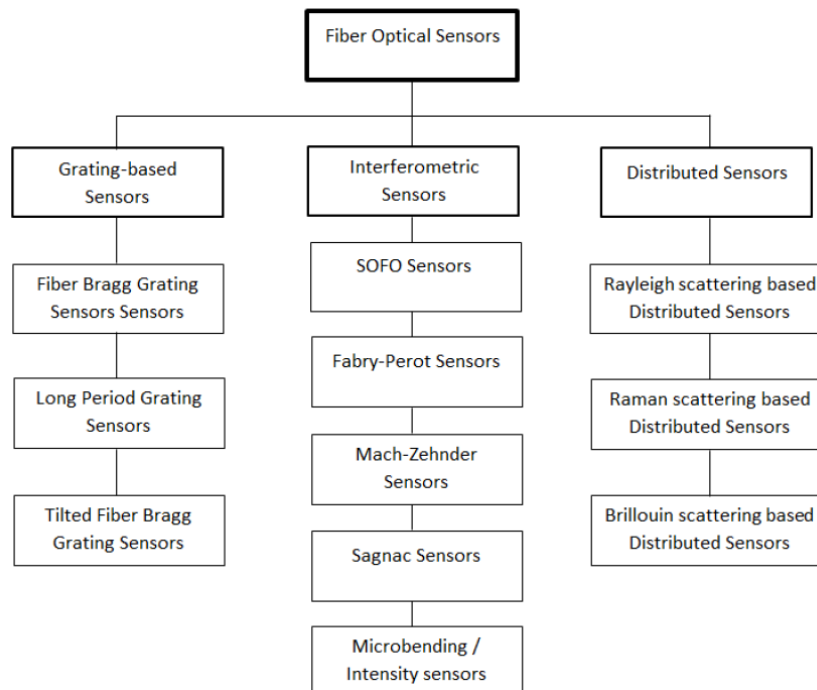


Figure 14. Overview of fiber optic sensor technologies (from [11])

Interferometric fiber sensors use the interference between two light shafts that have propagated through different optical paths of a single fiber or two different fibers [34]. They can be used to

measure many parameters including temperature, strain and distributed disturbance [35]. Grating-based sensors rely on periodic changes of refractive index of the fiber, thus being able to encode the measurand into wavelength ([36] and [37]).

Most OFSs, such as Fiber Bragg Grating sensors (FBG) [38] or Fabry-Perot sensors [29], are discrete and can only provide local measurements. Discrete short-gauge sensors provide useful and interesting data regarding local behaviour but might omit important information in structural areas that are not explicitly instrumented. Additionally, even though a particular failure is detected by means of a discrete sensor, pinpointing its location and magnitude can be tedious if it is not located exactly on the instrumented point (see Figure 15).

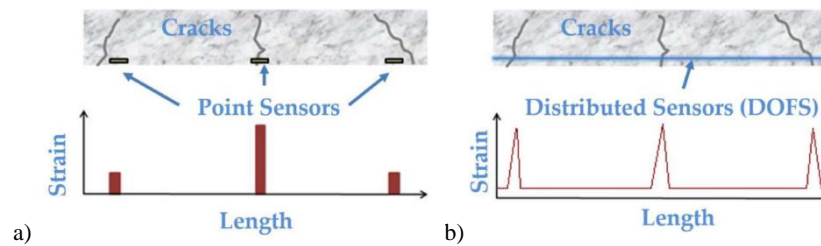


Figure 15. Spatial distribution detection of cracks with a) point OFS and b) distributed OFS (from [39])

To understand the global behaviour of a structure by means of discrete sensors, a high number of sensors would have to be installed producing a dense network of monitored points on the structure. This immediately translates into a very expensive and difficult to deploy SHM system with complex data acquisition and an excessive amount of wiring and measuring devices.

To deal with the mentioned limitations, optical fiber monitoring has been exploited to develop the last group of sensors, the Distributed Optical Fiber Sensors (DOFS), which are the focus of the present thesis.

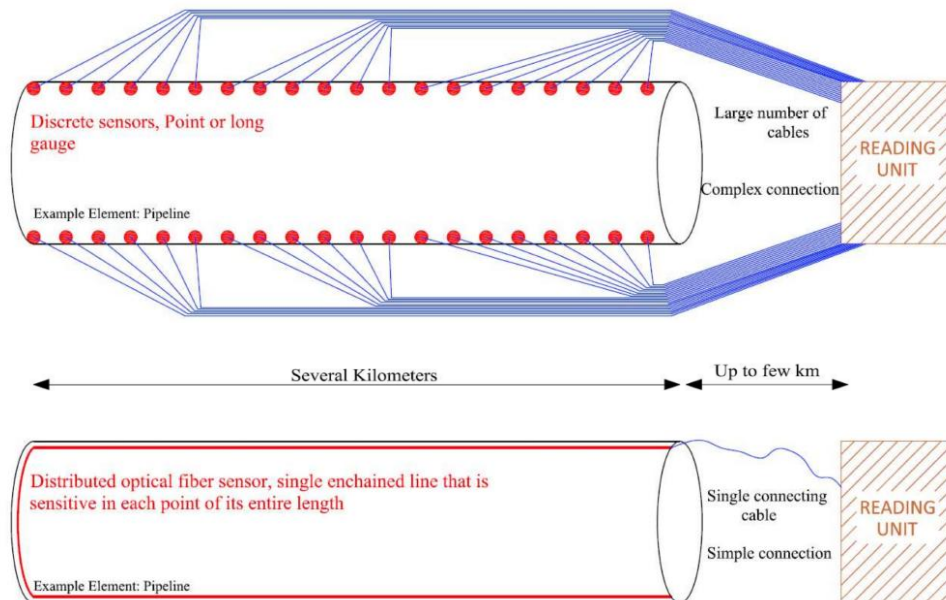


Figure 16. Comparison between the use of point OFS (top) and distributed OFS (bottom) (from [39])

It is worth noticing that distributed sensing can also be achieved with quasi-distributed FBG sensors centring several FBG sensors at different wavelengths through a technique named

Wavelength Division Multiplexing (WDM), and composing a FBG group in the same optical fiber [20]. However, this technique allows for measurement of a finite number of locations along the fiber path, WDM allows for approximately a 100 gratings to be multiplexed [11]. This quasi-distributed sensing technique is the most widely used in SHM projects and has been repeatedly applied in civil infrastructure monitoring projects, mostly in concrete bridges [40].

1.2.3. Distributed Optical Fiber Sensors

DOFS have the same advantageous characteristics as the rest of OFS but with the added value of allowing for distributed monitoring of strain and temperature variations along the entire optical fiber length. Additionally, this type of sensors only requires a single cable connection to communicate the collected data to the reading device [11].

The nature of this sensing tool allows for its bonding to the structural surface and even embedment inside the structural material. Therefore, when the structural elements experience changes in terms of temperature or strains, these are transferred to the fiber modifying its characteristics and causing the light travelling through it to experience perturbations. These perturbations are possible to detect mainly due to the light scattering, which is the most important light phenomenon to understand how DOFSs are able to conduct measurements.

Figure 17 and Figure 18 present the typical measurement tools needed to monitor a structure by means of DOFS.

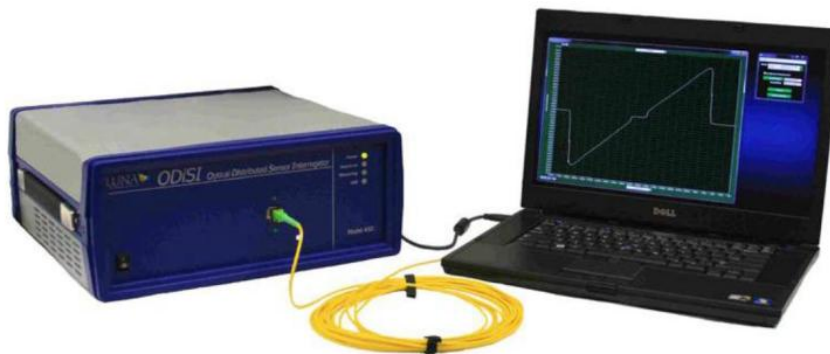


Figure 17. Typical DOFS measuring system (from [41])

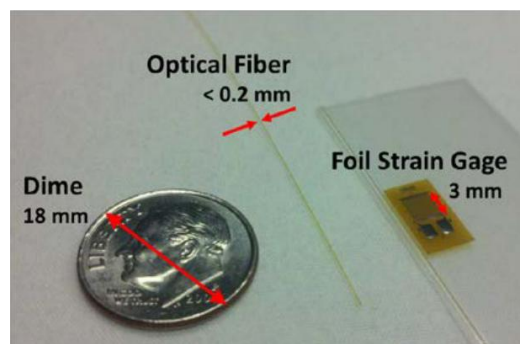


Figure 18. Size comparison between optical fiber and traditional foil strain gauge (from [41])

1.2.3.1. Scattering

Scattering can be understood as the light interaction with the optical fiber and it occurs when the optical properties of the core are modified at the arrival of the light wave (see Figure 19). When

an electromagnetic wave is projected into an optical fiber its propagation through the core medium interacts with the present particles it can either generate a second electromagnetic wave (scattering) or return towards the light source (backscattering). The later is the one used to acquire information regarding the perturbations that the fiber and, consequently, the structure are subject to.

Minimal fiber modifications can generate different light scattering processes depending on the interaction mechanisms between the propagating light pulse and the optical fiber [32]. The scattered spectral components include Raman, Brillouin and Rayleigh peaks (see Figure 20).

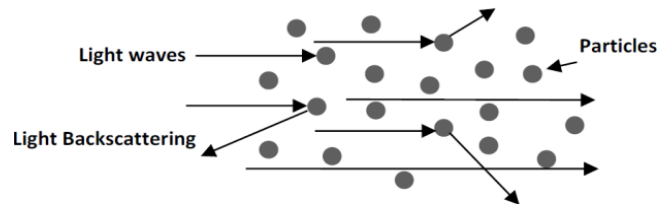


Figure 19. Scattering and backscattering of light in an optical fiber core (from [20])

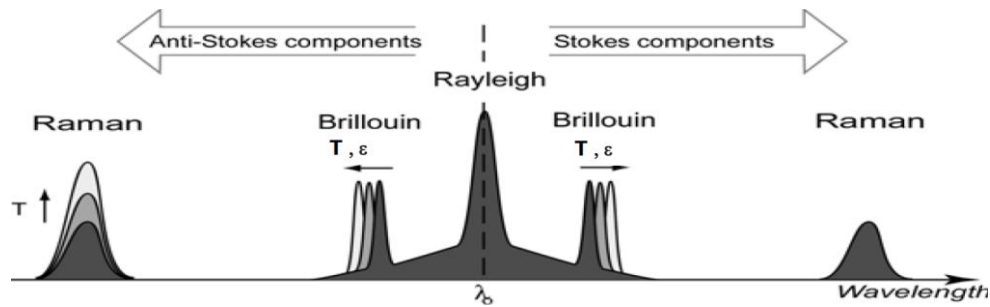


Figure 20. Wavelengths of the backscattered radiation (from [42])

As stated in [42], Brillouin scattered light depends on both temperature and strain and is very dependent on fiber density. The techniques based on it involve the measurement of a frequency which allows for higher accuracy and stability in the measurements at long term when compared to Raman-based techniques, which rely on intensity measures [32]. Raman scattering anti-Stokes component depends only on temperature and, since the intensity of this component increases with the time of arrival, combining it with the Stokes component can give information regarding temperature and position of the perturbation [32]. Finally, Rayleigh scatter is independent of most of the external physical characteristics and is generally used to measure propagation effects, which can also affect the two initially presented techniques (Raman and Brillouin) but these neglect them due to their direct relation with the temperature and strain fields [11].

The backscattering provides a set of data that can then be processed in order to obtain the physical variations that the fiber and, consequently, the structure are subject to. Different DOFS have been developed answering to different techniques regarding light impulses and generated backscatter reading consequently widening their applicability in SHM. The most widely used reflectometry techniques in DOFSs are generally presented below.

1.2.3.2. Reflectometry techniques

The first reflectometry technique to emerge and allow for truly distributed and continuous monitoring was the Optical Time-Domain Reflectometer (OTDR). It is a technique that involves the launching of a short optical pulse into a fiber and processing the amount of backscattered light through a photo detector as the light shaft propagates along the fiber [11]. By measuring the variations of intensity of the Rayleigh backscatter (happening due to the attenuation processes mentioned before) it can obtain the spatial variations experienced by the fiber. As shown in Figure 21, when the fiber is subject to an external perturbation, attenuation will appear in the perturbation location.

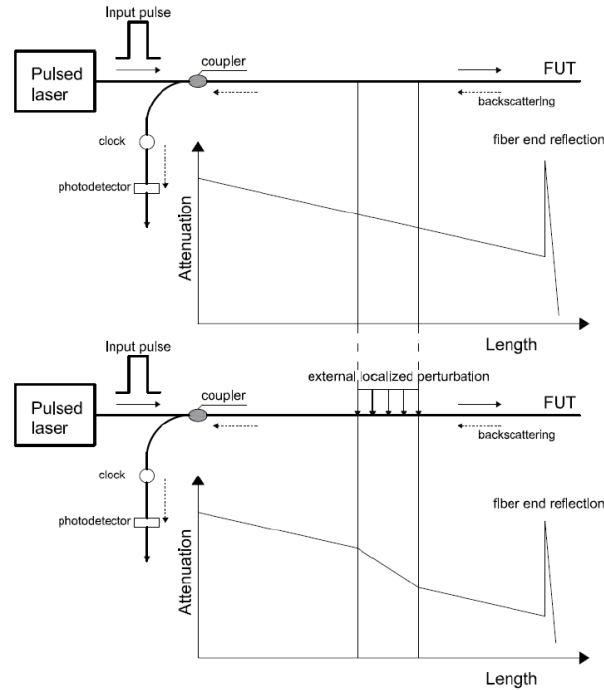


Figure 21. Principle OTDR based on Rayleigh backscattering read by the Fiber Under Test (FUT) (from [30])

The OTDR technique is characterized by a low spatial resolution of approximately 1m, which limits its applicability to SHM. Since increasing the spatial resolution implies lowering the pulse width and, consequently, reducing the detected backscatter, a balance needs to be found between spatial resolution and sensing range to optimize the performance of each deployment.

A part from Rayleigh, Raman and Brillouin scattering can also be used to provide distributed sensing. Brillouin scattering occurs from acoustic vibrations stimulated in the fiber and the techniques based on this component focus on the frequency shifts between the original pulse and the resulting Brillouin backscatter. The Brillouin Optical Time Domain Reflectometer (BOTDR) is based on the spontaneous Brillouin scatter while the Brillouin Optical Time Domain Analysis (DOTDA) on the stimulated. Even though Brillouin based techniques are the most widely used in SHM deployments, their applicability is limited by their low spatial resolution of 1m.

The system that answers to the high spatial resolution demands, of millimetre scale, is the Optical Frequency Domain Reflectometry (OFDR). These sensors are based on very narrow light pulses, which imply a considerable reduction of the backscatter signal that requires an increased receiver bandwidth to be detected. It is worth mentioning that the requirements that high spatial resolution implies result into very expensive technologies, such as the Optical Backscatter Reflectometer (OBR). The OBR is based on the detection of the spectral shift that

the backscatter pattern presents when the fiber is subject to external stimulus and, it can later be used to calculate the strain variations along the fiber

There have been many experimental laboratory tests and real applications that used the aforementioned technologies and have, consequently, allowed for the assessment of their performance under different conditions and the definition of their applicability. Barrias et al [11] developed Table 1 summarizing their characteristics, which includes the FBG quasi-distributed technique for comparison with the recently presented distributed systems.

Table 1. Performance of distributed and quasi-distributed sensing techniques (from [11])

Sensing Technology	Transducer Type	Sensing Range	Spatial Resolution	Main Measurands
Raman OTDR	Distributed	1 km [73] 37 km [74]	1 cm [73] 17 m [74]	Temperature
BOTDR	Distributed	20–50 km	≈1 m	Temperature and Strain
BOTDA	Distributed	150–200 km [13]	2 cm (2 km) [75] 2 m (150 km) [76]	Temperature and Strain
Rayleigh OFDR/OBR	Distributed	50–70 m [11]	≈1 mm [66]	Temperature and Strain
FBG	Quasi-distributed	≈100 channels	2 mm (Bragg length) [21]	Temperature, Strain and Displacement

As can be seen, Brillouin based sensors provide a significant measurement range that makes them very suitable for SHM deployment on large structures. However, when higher spatial resolutions are required other sensors become more convenient.

The OBR technique, which is the one used in the case study of this thesis, provides a good balance between cost and efficiency granting millimetric spatial resolutions at the expense of sensing range (only up to 70m).

1.2.3.4. DOFS applied in civil engineering

As mentioned before, the majority of OFS techniques deployed in the civil engineering sector involve discrete sensing. However, nowadays DOFS present more attractive features than those provided by local and quasi-distributed sensing systems.

Even providing a clear set of advantages regarding structural monitoring, DOFS techniques applied to SHM projects constitute a relatively recent field of study and there is a significant amount of research and development needed before they can become a reliable universal strain-reading method.

Nevertheless, several SHM systems based on this type of sensors have been deployed over the last decades in the civil engineering industry and, additionally, extensive work regarding the improvement of such sensors has been executed by means of laboratory tests. With the aim of providing an overview of the performance of such sensors in real structures some of the documented DOFS implementations involving SHM will be presented in this section.

DOFS applied on real structures

Nowadays, FBG discrete sensors represent the majority of optical fiber sensing techniques applied on civil engineering SHM and they have been extensively studied and discussed. Nowadays, as opposed to conventional sensors, DOFS clearly offer a superior cost-efficiency

performance and higher reliability. However, relatively few deployments of this technology have been executed due to their recent development.

Several experiments have been conducted to improve the sensors capabilities and assess their performance ([15], [20], [30], [32], [39], [43]–[51]). These publications have provided significant insight regarding DOFS applicability and provide key considerations for successful deployment.

Regardless of their newly development, some DOFS applications have been done in the last two decades in different civil engineering structures such as dams ([52], [53]), high rise buildings [43], bridges ([46], [49], [54], [55]), slopes [56], piles [57], pipelines ([52], [58]), among others. Other structures, such as historical buildings [46] and a concrete cooling tower [49] have been monitored as well by means of DOFSs. Some of these structures are presented below.

Already in 1999, a major **dam in Luzzone** (Swiss Alps) had to be raised to increase the power capability of the associated hydroelectric plant and the procedure required of monitoring for serving purposes [53]. The aim was to monitor the temperature variations horizontally after concreting in the raising plane section and it was done by means of a small optical telecommunication cable embedded to the concrete over the central layer of the largest slab.

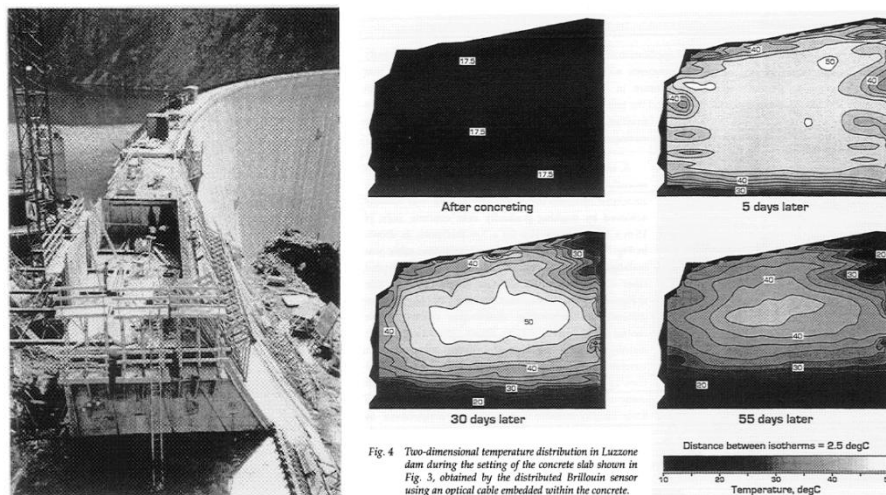


Figure 22. Luzzone dam in the Swiss Alps (from [53])

Between 2007 and 2009, monitoring tests by means of DOFS and system BOTDA were conducted to **Götaälvbron bridge** (Gothenburg, Sweden), built in the late 1930s due to the prior appearance of fatigue cracks and because 15 more years of service life were required [55].



Figure 23. View of Götaälvbron (from [55])

The same monitoring system was tested in Streicker bridge (Princeton, US) [54].

In 2010, a bridge load test performed in a **Cerdanyola del Vallès viaduct** (Barcelona) was used to investigate the effectiveness an OBR system [49] (see Figure 24). A few years later, the same system was used to provide SHM to the **Sarajevo bridge** (Barcelona) in order to monitor the structure during a deck enlargement rehabilitation [46] (see Figure 25). This project was carried out through several months in different seasons, which allowed to address the relevant issue of DOFS that is temperature affections proposing a compensation methodology.



Figure 24. Viaduct Road BP-1413 in Cerdanyola del Vallès (Barcelona) (from [49])



Figure 25. Deployed OBR system in Sarajevo Bridge (Barcelona) (from [46])

The same OFDR technique was applied in the crack monitoring project of a 120m high concrete cooling tower [49]. The structure was instrumented in order to monitor the crack pattern due to wind forces and temperature effects and to observe the behaviour of the repaired structure. The high spatial resolution that this technique provides was crucial in this deployment.

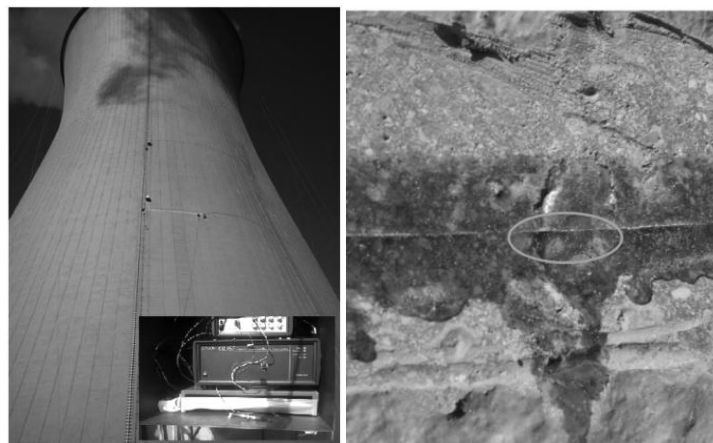


Figure 26. Positioning of OBR system in concrete cooling tower (from [49])

An additional structural application of the OFDR technique was deployed by the same team in the historical building that is **Sant Pau hospital** (Barcelona) [46]. After a complete structural assessment of the building it was concluded that two brick masonry columns had to be replaced

by new steel columns (encapsulated after the works to preserve the visual scheme). Being a hospital, the works had to take place with the building in full service. For that reason and being the building a UNESCO world heritage site, the monitoring of several masonry vaults was conducted during the works period providing continuous control of the possible affection resulting from the rehabilitation works.

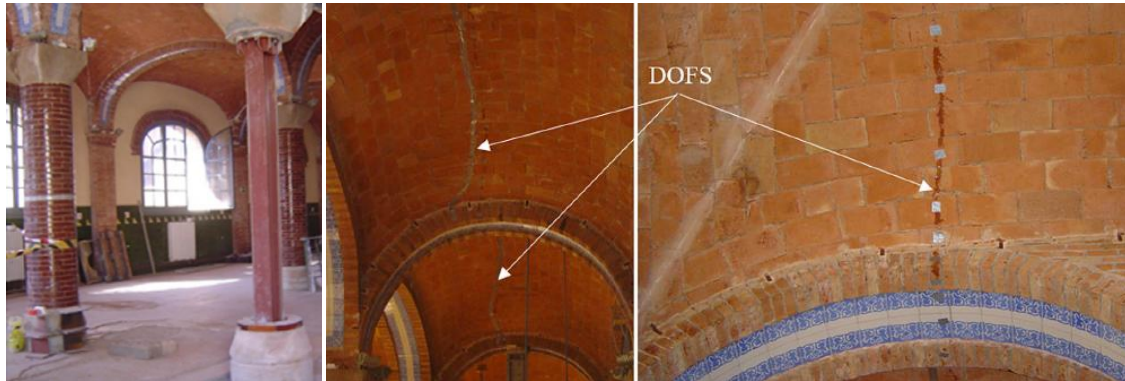


Figure 27. Sant Pau Hospital's masonry vaults monitoring (from [46])

1.2.3.5. DOFS applied in tunnels

Given that the nature of this research project is tunnel monitoring by means of DOFS, the documented application of such sensors in tunnels is presented separately in this section.

In urban environments with dense edification and complex underground networks it is inevitable for existing and new tunnels to be affected by or affect new underground or ground level constructions. In this cases, i.e. when a particular structure can be subject to external loading effects, it is crucial to deploy adequate SHM to ensure safety.

Tunnel monitoring by means of DOFS has been deployed in structures equally during construction works and under operation and with the aim of providing real-time information regarding the integrity of the structure. The following documented applications demonstrate the potential benefits that DOFS monitoring provides regarding SHM.

Additionally, since the a section of this thesis is devoted to extending the DOFS applicability to convergence monitoring, some tunnel monitoring applications discussing that matter will be presented as well.

Tunnel monitoring

During the construction of the large Crossrail platform tunnel in London, the **Royal Mail tunnel** was found in the surrounding alterable area being located directly above the to be constructed tunnel line at Liverpool Street Station [59]. In this case, Brillouin Optical Backscatter Reflectometry (BOTDR) was used, the attachment of the DOFS was performed through continuous gluing with the layout shown in Figure 28. The relatively innovative monitoring technique was complemented by the installation of an Automated Total Station with the aim of comparing their respective readings.

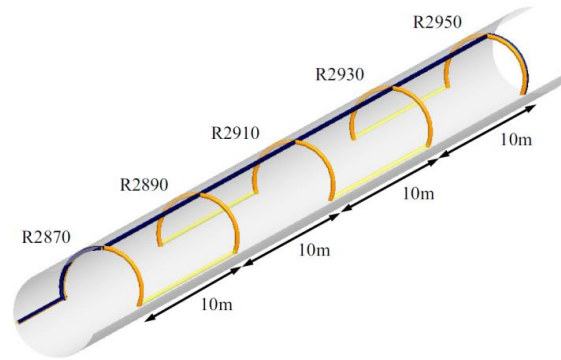


Figure 28. Optical fiber cable instrumentation at Royal Mail tunnel (from [59])

It is worth noticing that temperature compensation was applied to the performed strain readings to separate the mechanical and thermal components of the readings by means of a segment of the fiber unattached to the structure, i.e. only affected by temperature variations, running alongside the strain sensing cables.

In the end, the corrected strain readings showed a clear strain profile (see Figure 29) that matched the conventional displacement measurements of the Total Station and showed clearly the crown settlement and the flexible behaviour of the Royal Mail tunnel as most of the measured strains were recovered after the tunnelling face had advanced away from the measuring point.

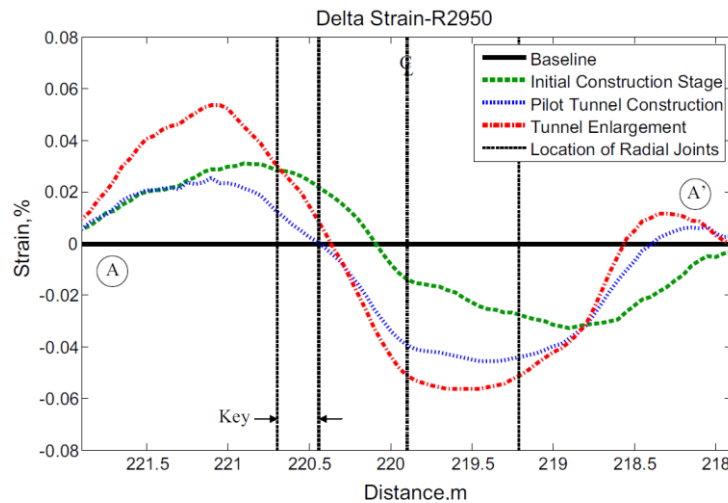


Figure 29. Plot of cumulative change in strain for ring R2950 at various construction stages (from [59])

Another successful deployment of DOFS was performed in the **Shinkansen tunnel**, where the Japanese Bullet Train runs [60]. Following a laboratory experiment regarding the monitoring of concrete lining segments by means of DOFS and Electric conductible paint, a field experiment was executed in the mentioned tunnel to assess the performance of such sensors in real world conditions. No affections were planned to take place in the surroundings of the monitored location, being the aim of the monitoring procedure the assessment of the sensors performance under tunnel service conditions such as strong wind pressure by train running or surrounding rock pressure. The experiment took place during approximately three years and some of the periodically performed strain readings are shown in Figure 30 showing that the measured values were continuously stabilised. The long term applicability of DOFS using the BOTDR technique

was, therefore, proven stating in the paper conclusions that the utilised method had sufficient applicability to damage surveillance of tunnel linings.

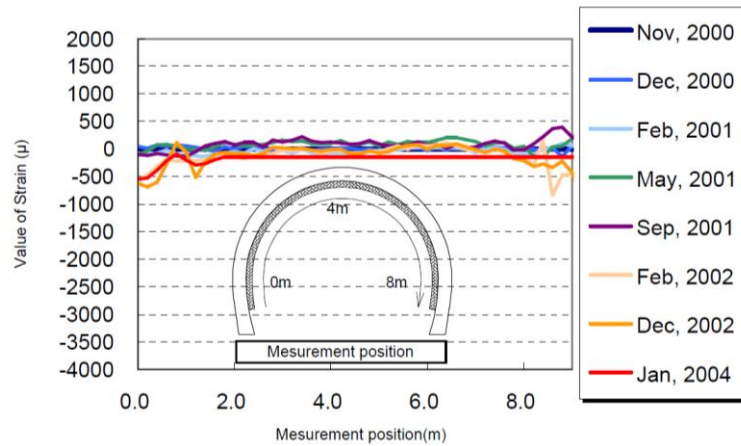


Figure 30. Results of strain measurements on the Shinkansen tunnel (from [60])

The aforementioned SHM deployments involved already constructed structures affected or not by external actions with sensors bonded to the inner structural surface. However, structural assessment is also needed during construction.

The monitoring process of a **highway tunnel in Žilina (Slovakia)** by means of distributed fiber-optic technology is presented in [61]. The article describes and analyses real measurements performed within a period of 5 months covering the whole process of building a new tunnel. Being located in unstable agricultural land, forests and meadows, the 867m long structure was to be surrounded by claystone and clayey soil. The soil conditions already anticipated issues related to the excavation progress and unstable overburden of the structure and, for that, Metrostav (the construction company) required the monitoring of the development of the load changes over time.

The tunnel was excavated using the New Austrian Tunnelling Method (NATM), also known as sequential excavation method, in which the entire profile of the tunnel is not excavated at once but one section at a time. This process allows to take advantage of the bearing function of the rock mass and to optimize the tunnel lining installation by means of geotechnical monitoring. The tunnel lining consists of two parts, the primary lining (built right after the excavation works) and the secondary lining (usually a ferro-concrete shell and quite often involving the use of prefabricated components) separated by a waterproofing spacer (see Figure 31).

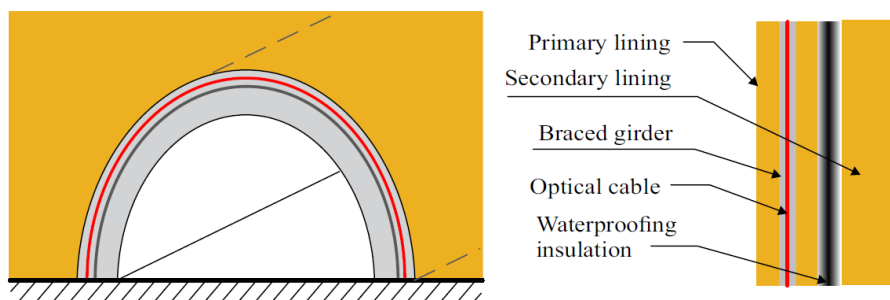


Figure 31. Structure of the tunnel in Žilina (from [61])

The optical fiber was placed on two iron bars of the braced girder of the tunnel, which became a part of the primary lining after being strayed with concrete (see Figure 32). The installed distributed sensors were based on Brillouin scattering (BOTDR).

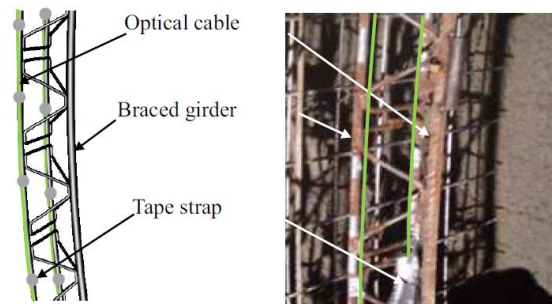


Figure 32. Optical fiber implementation on iron bars of the braced girder on the primary lining (from [61])

After the DOFS deployment the measurements took place over 6 days comprised in a period of 5 months. Each measuring day was chosen depending on the accessibility of the tunnel and in it 25 measurements were performed being the obtained results later averaged for subsequent post-processing.

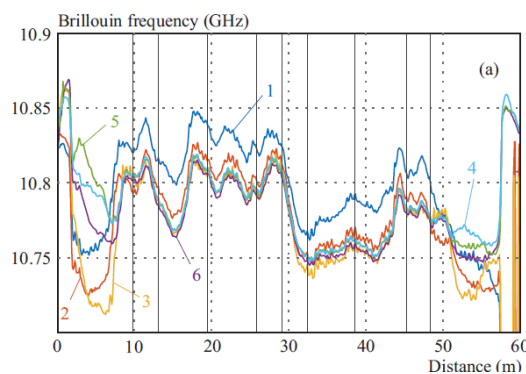


Figure 33. Measurement of Brillouin frequency from 6 measurements (from [61])

Since the objective is to determine the changes in load, the interpretation of Brillouin frequency variations was considered enough; if it increases there is a load increase and the same in the other way. The evolution of the frequency during the monitoring period was easily explained by the concrete cooling (due to initial hydration) and posterior shrinkage. Therefore, DOFS reproduced the structural behaviour correctly. After the initial measures, the frequency seems to stabilize implying that the surrounding rock mass is relatively at rest. However, it is concluded that, movement of rock mass is a long term matter and, for that, sensors will continue to operate until the end of construction works in 2017 (surpassing the publication date of article [61]).

Another monitored tunnel construction was performed in the tunnel of **Xinyi line from the Taipei Mass Rapid Transit** (MRT) [62]. In this case, the problematic regarding this construction was: the construction involved soft ground shield tunnel lining, a system that had been relying on semi-empirical procedures and might have been too conservative, the earth pressures involved couldn't be accurately computed adding uncertainty to the tunnel design and, finally, the closeness to other underground constructions given the dense tunnel network. For that, a monitoring scheme was proposed to measure the strains of the tunnel lining. Even though, this project in particular does not involve DOFS, only FBG sensors, it is considered to be an interesting optical-fiber monitoring deployment thus it is presented here as well.

The local sensors were installed as shown in Figure 34, embedded to the concrete segments and attached to the steel reinforcement whose section was later filled with epoxy.

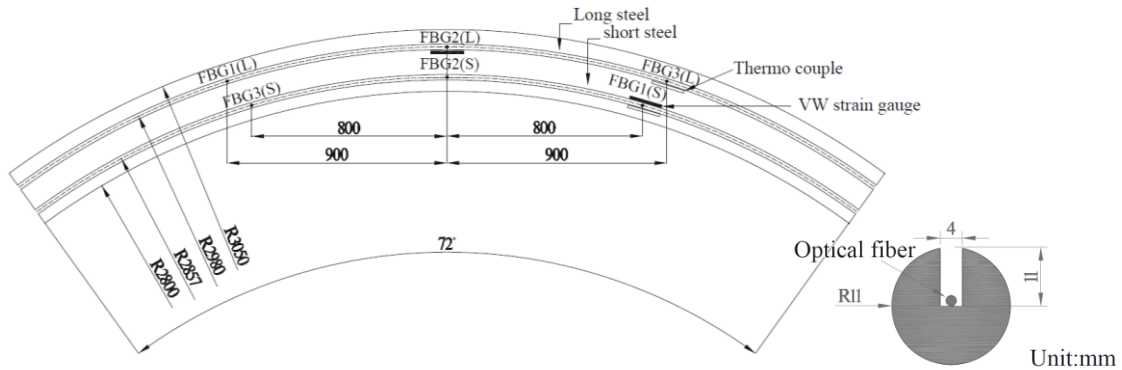


Figure 34. FBG strain sensors location (from [62])

The local sensors have to be placed strategically in order to monitor the desired effects, they require high precision of installation and cataloguing to allow for appropriate interpretation of the results. Moreover, the deformation of the monitored section is hard to extract from the readings (see Figure 35). In the mentioned article it is only concluded that there are fluctuations at the beginning due to assembling of panels and backgrouting and that two of the outer sensors experiment tensile stress while the rest are subject to a modest earth pressure and thus compressed. The problem lies in that what is happening between the sensors is not known and they are not too separated from each other to experience such different behaviour thus definite conclusions on the section deformation cannot be extracted. However, since the aim of this project was to roughly evaluate the effects of the shield tunnel boring machine advancing and the posterior effects of earth pressure on the concrete lining and not the tunnel section deformation itself, FBG can provide a general overview on the tendency. DOFS installed in parallel to the tunnel axis would have provided much interpretable results on the tunnel axial behaviour and a single transversal section monitored continuously would have given a clear idea of the global deformation of the tunnel section.

All in all, the collected values seem to make sense showing compression at a later stage earth pressure (not seen in Figure 35 since it only presents early stage monitoring). A positive outcome can be extracted which is the fact that nearly five years after construction, the sensors are still functioning.

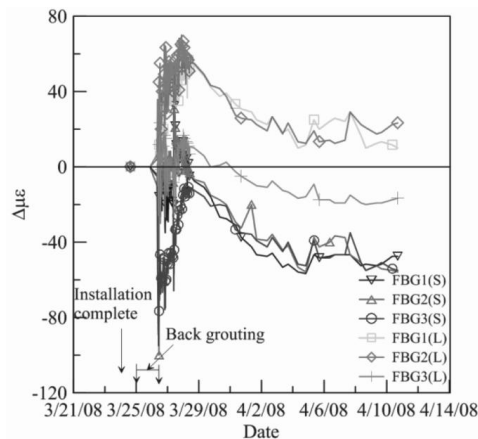


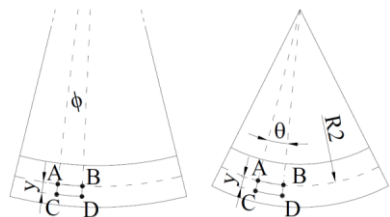
Figure 35. Change of strains at early construction stage of different local sensors (from [62])

From the presented articles and other successful deployments that haven't been mentioned, it can be extracted that DOFS provide an easy to deploy monitoring technique and sets of data that are interpretable, with which an in-depth evaluation of the concrete lining section behaviour can be conducted.

Tunnel convergence computation

A part from tunnel monitoring and interpretation of strain readings, this report additionally focuses on extending the applicability of the DOFS by proposing the convergence computation based on the readings themselves. In that matter, few publications have been developed but two were found particularly interesting and worth mentioning.

A technique exploiting fiber Bragg grating sensors has been conceived using a particular method for convergence monitoring called **Extensometric Method for Monitoring Convergences in Tunnels (MEMCOT)** [14]. This technique, tested in the **Rossio tunnel** (Lisboa, Portugal), continuously assesses the displacement of the tunnel support by measuring deformations along the contour by means of strain gauges. Applying a mathematical model based on the Theory of Bending Initially Curved Bars, the article shows that it is possible to model quantitatively the radial displacement using the axial strain that is being measured. A formula for the radial displacement non-linearly depending on the point strains, the neutral fiber height and the initial radius of the tunnel is proposed but there is no presented application.



$$\varepsilon_{CD} = \frac{\Delta \ell_{CD}}{\ell_{CD}} = \frac{(R_2 + y)\phi - (R_1 + y)\theta}{(R_1 + y)\theta} \quad (1)$$

$$R_2\phi = R_1\theta$$

$$\delta = R_1 - R_2 = \frac{\varepsilon_x R_1 (y + R_1)}{\varepsilon_x R_1 + y(1 + \varepsilon_x)}$$

Figure 36. Proposed radial displacement (δ) (from [14])

In another publication Piccolo et al. [15] propose and demonstrate the feasibility of the interpretation of the orthoradial strain measurements obtained by a DOFS to obtain the structural convergence using an inverse analysis associated with the finite element model. They do provide an application of the proposal through a **laboratory experiment** on a steel ring of 762mm of diameter connected to a reaction frame (Figure 37). In the experiment, Brillouin and Rayleigh based sensors performances are compared as well as their bonding methods (glued or soldered). Additionally, the obtained displacement results, based on DOFS strain monitoring, are compared to the displacements captured by MEGATRON sensors (position transducers).

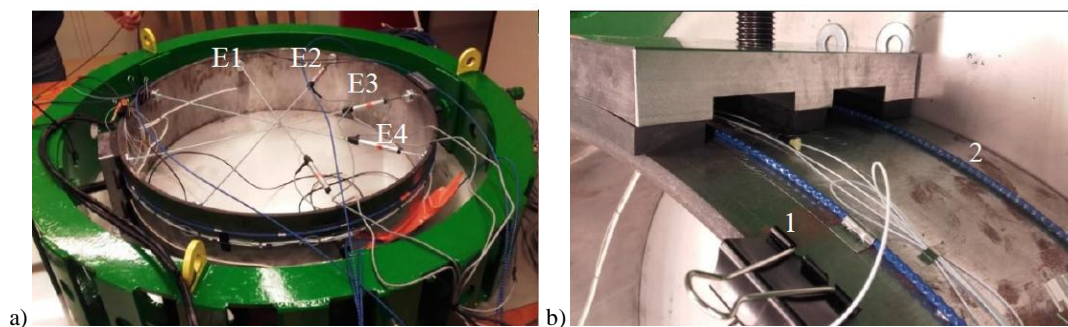


Figure 37. Laboratory experiment on convergence computation a) The reaction frame with connected metallic ring and inner reference sensors and b) detail of the sensors: 1. soldered cable and 2. glued cable (from [15])

Figure 38a) presents the best orthoradial strain monitoring performance which is obtained with Brillouin scattering and glued sensors. The performance of the three left optical fiber sensing techniques is good but presents higher level of noise. The convergence computations, after the inverse finite element analysis, are shown in Figure 38b). As can be seen, the computed values are very accurate, with a millimetre precision, which opens the door to a new promising application of DOFS.

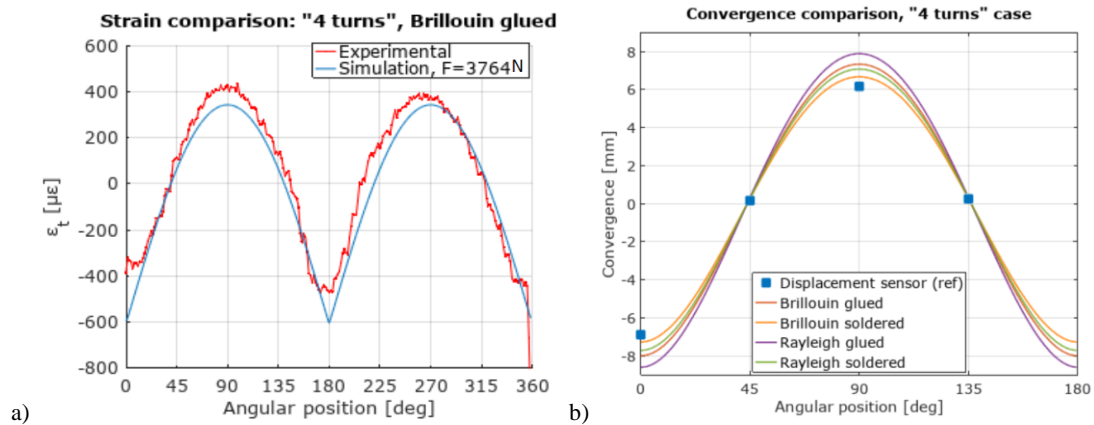


Figure 38. Results on steel ring monitoring: a) orthoradial strain measures provided by glued sensors and Brillouin scattering and b) computed convergence from DOFS strain measurements and traditional position transducer readings (from [15])

1.2.3.5. Summary of DOFS advantages and limitations

After the presentation of numerous laboratory real applications of DOFS, it is clear that they present numerous assets that appoint them as one of the best options to deploy adequate SHM. Indeed, they could be considered as the latest upgrade of the optical fiber sensing field. A list summarizing the extracted advantages and limitations of such sensors is presented bellow.

Advantages:

- **Reduced dimensions**, which ease bonding and embedment on structural elements and improve the reproduction of the structural behaviour.
- **Easy installation process**, i.e. they only require cleaning the surface to monitor and bonding the fiber to it by means of an adhesive.
- **Lower installation and maintenance costs** than other sensors.
- **Accurate readings** and superior efficiency.
- **Distributed monitoring**. They allow for 1-D continuous monitoring as opposed to local measurements easing the deformation interpretation and the damage pinpointing processes.
- Wide range of **applicability** to all kind of continuous structural surfaces subject to damage in civil, structural and aerospace engineering.

- **Immune** to / Still reliable under electromagnetic influences and aggressive environments. The readings only depend on strain and temperature, and the later can be compensated.
- **Rapid data collection** and transmission.

Limitations:

- **Cost.** They require a high initial investment regarding software, monitoring devices and optical fiber sensors.
- It is a **new/under research** technology, which translates to no standardized guidelines on how to ensure success in every deployment.
- Frequent appearance of **anomalies** in the DOFS measurements.
- Lack of completely reliable DOFS/structural support **bonding** technique.

Regarding the limitations, it is important to mention that they are all caused by the DOFS's own innovative aspect. The forecast report presented in March 2019 [63] states that the distributed fiber optic sensor market stood at \$651 million in 2014, then, the overall market contracted through 2016 due to the fall in oil prices which presented a modest recovery in 2017 until late 2018. Recently, another oil price drop has impacted the market which diminishes the previously predicted tendency. The total distributed fiber optic sensor market that was projected (January 2017) to be \$1,008 million in 2021 is now projected to be \$821 million in 2021 **reaching \$1,033 in 2023** (see Figure 39).

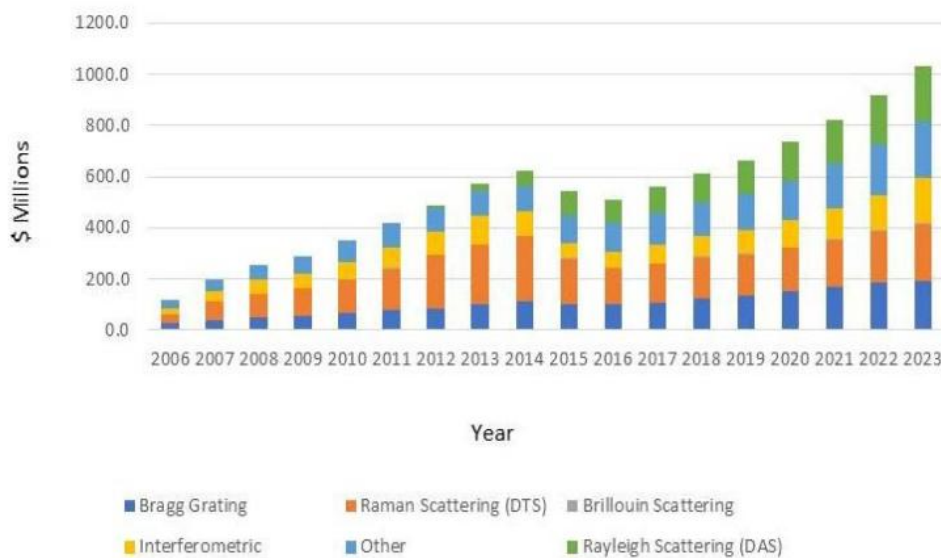


Figure 39. DOFS market forecast (from [63])

The market tendency is clear and it will lead to further research and investigation regarding the improvement of this SHM technology thus the resolution of the currently existing limitations.

2. Objectives

After the introduction of this Final Master Thesis, a list of its main objectives can be presented below:

- To demonstrate the potential of the Distributed Optical Fiber Sensor technologies in the field of Structural Health Monitoring, specifically studying their performance in damage detection in concrete structures through a case study.
- To improve the case study's extracted data by performing an analysis of peak strains and anomalies and substituting them with coherent values.
- To correlate the treated data with the building construction time-line and a structural study of the case by means of a simple theoretical model based on Finite Elements in order to verify the measurements of the DOFS.
- To analyse the strain readings in the different monitored segments to ensure the structure's safety proving that the computed values remain inside an acceptable domain.
- To propose a computation method to obtain the convergence of the tunnel section from the strain readings and assess its performance.

The following sections will be devoted to the exposition of how the mentioned objectives are fulfilled in the course of an academic year. Firstly, the case study will be presented in detail in section 3, the developed data treatment method will then be described in section 4, and an explanation of the displacements computation from the post-processed data will take place in section 5. Finally, section 6 will contain a presentation of the obtained results, which will be interpreted, and an assessment of the methodology adopted in this Final Master Thesis.

3. Case study: DOFS installation in L-9

The city of Barcelona has faced, over the last years, several problematic situations regarding underground infrastructure. The fatidic ground collapse in the Carmel neighbourhood in January 2005 due to the TMB metro line L-5 extension works marked a turning point in public infrastructure execution regarding control and monitoring commissions. Since then, all construction works and projects taking place in the metropolitan area of Barcelona are subject to more strict and exhaustive inspection protocols for which in depth structural justifications, geological studies and monitoring protocols have to be presented backing every constructive offer ensuring safety regarding the construction site and its surroundings or possible subsequent affections.

The object building of this thesis is being constructed in the Bon Pastor neighbourhood of Barcelona and it is no exception to the aforementioned safety regulations particularly considering that its extension is partially covering the TMB L-9 metro tunnel layout. For that, the structural affections of the construction process on the underground infrastructure are studied, in this case, by means of structural monitoring.

With the aim of contextualizing the particular DOFS' application that this TFM focuses on, the following sections will aim to describe in detail the constructive project itself and the proposed monitoring system.

3.1. Project description

The building under construction is located between Novelles, Tallada and Sant Adrià streets, forming an angle of approximately 60° with the 4th section of the L9 Metro Sagrera TAV-Gorg tunnel's layout. As can be seen in Figure 40, the South-East corner of the building is found over the tunnel's layout.

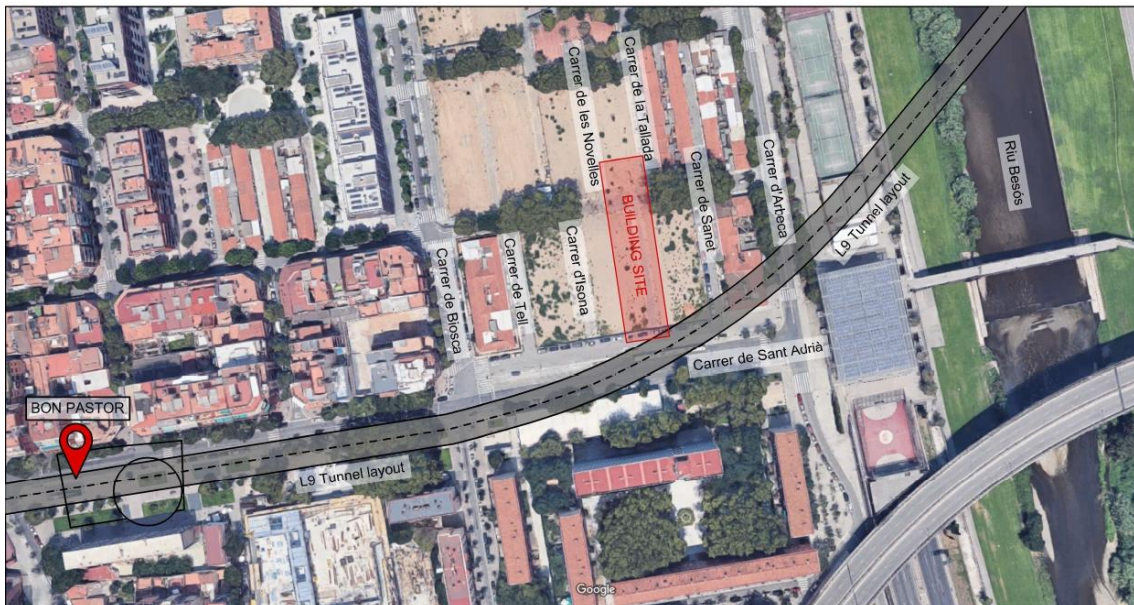


Figure 40. Building site location (red), TMB L9 layout and access station Bon Pastor (own development with base image from [64]).

The TMB L-9 is a 47.8km long (43.71km of which are underground) automated (driverless) metro line aimed at connecting the perimetral metropolitan areas of el Prat de Llobregat, l'Hospitalet de Llobregat, Badalona and Santa Coloma de Gramenet to the metro service of Barcelona [65]. The currently active segments of L-9 are the south segment (from Barcelona - El Prat Airport T1 to Zona Universitaria, approx. 20km long) and the north segment (from La Sagrera to Can Zam, approx. 11.1km long) both being characterized by a service frequency of 6 minutes. The central segment is not finalized at the moment but is expected to be operative by year 2023[66]. Given the magnitude of such infrastructure, the need for structural safety assurance is more than understandable.

The tunnel structure was executed by means of a Tunnel Boring Machine with an Earth Pressure Balanced shield type to ensure operability in soft soil [67] and, as the perforation proceeds the 35cm thick tunnel ring is executed resulting into an 11.60m diameter tunnel that enables the construction of the stations and auxiliary installations in the tunnel itself. Such vast diameter allows for the he trains to run at two levels, i.e. one above the other being separated by a supplementary slab (see Figure 41).

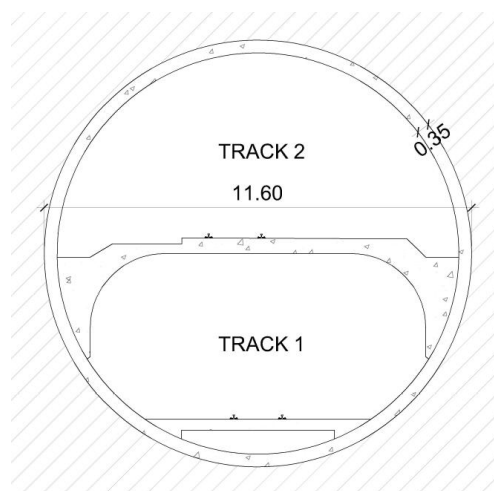


Figure 41. Tunnel cross section

The project object L-9 segment to be studied belongs to the north line and can be found between metro stations Bon Pastor and Llefià being located closer to the first one.

The new structure, located slightly above the L-9 tunnel layout can be defined as a residential building composed by a basement floor aimed at parking space, ground floor and four floors above it rising up to approximately 18.10m above ground level. As can be seen in Figure 42 and Figure 43 in detail, the building site's dimensions are approximately 83x20m (1660m²) of which roughly 37m² can be found right above the L9 tunnel section covering, at the most critical location, half of the tunnel layout.

It is worth noticing that the excavation works of the new structure stretch to -3.90m underground, in other words, an approximate total soil volume of 6500m³ is removed during the excavation works in order to execute the foundations of the building. The lowest point of the building structure, i.e. lower surface of 80cm thick concrete foundation slab, is at -3.90m. Being the highest point of the underground structure at -18.30m, an approximately 14.40m thick soil layer is found to be separating both structures.

Even though more detailed geometry drawings on the case study can be found in Annex 2 the following figures are presented to ease the explanation

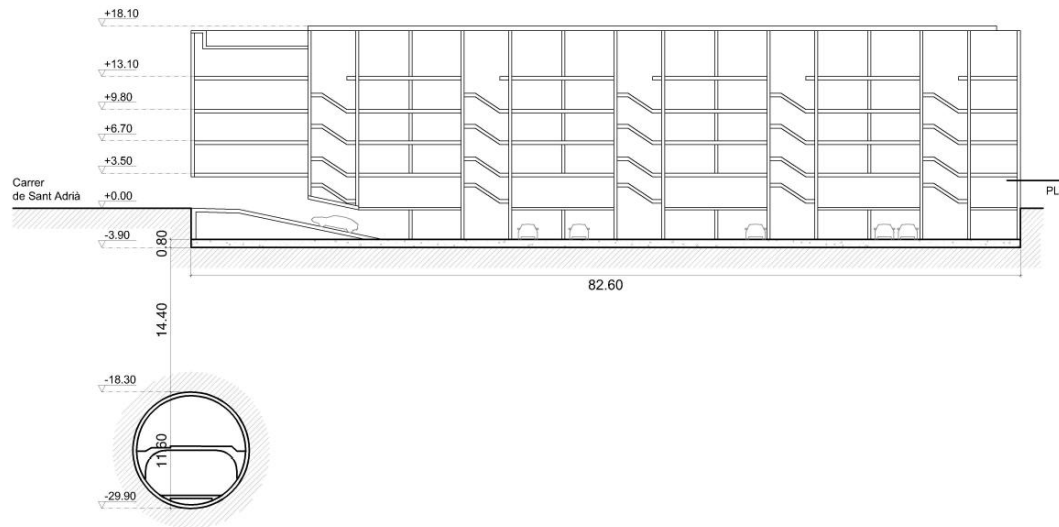


Figure 42. Schematic cross section of L9 tunnel in relation to the building

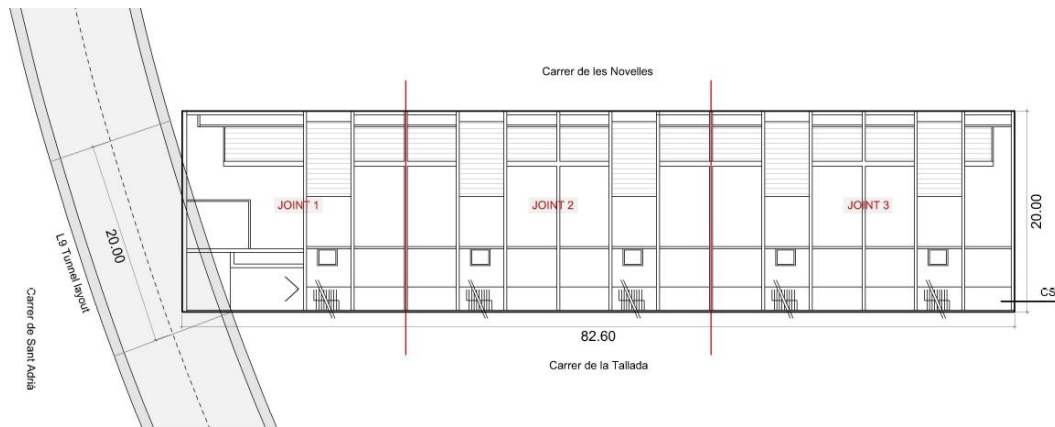


Figure 43. Schematic plan view of L9 tunnel in relation to the building

The construction site is divided in three areas of execution and the corresponding joint numbers seen in Figure 43 are a reference to the constructive order of the structure. Joint 1, the closest to the tunnel layout, is the most advanced section of the building in terms of constructed surface during the whole project length as will be seen later in the model construction time-line developed in posterior sections. The reasons behind the joint construction order are safety related in an attempt to diminish the possibility of any adverse effects if the deformation and tension tolerancies are exceeded in the underground structure at some point during the construction period. Therefore, larger unloading / loading effects are expected to be noticed in the tunnel during the beginning of the project execution rather than the end. By the time joint 3 is being developed fairly small effects, none at all or only the effects posterior to soil consolidation are expected.

The 20m long measurement along the tunnel axis in Figure 43 is aimed at delimiting the affected segment of the underground structure, i.e. tunnel length to be monitored and controlled during construction.

As a result of the problem's nature, the structural assessment specialized company Cotca S.A. became responsible for the tunnel's structural monitoring project. To perform a continuous follow-up of the tunnel's strain and tensional state, a DOFS based monitoring scheme of the tunnel's section was proposed and is described in the following sections.

3.2. Objectives of the SHM

The key objectives in all Structural Health Monitoring (SHM) projects are safety and the cost optimization in case of failure that early detection allows for. With a building being constructed above the tunnel layout several considerations have to be taken into account.

The fact that the corner of the building site covers the tunnel layout unsymmetrically to the tunnel axis could induce the thought of differential loading over the tunnel, meaning that the cross section might not deform symmetrically since the tunnel sector right under the building could come to endure higher decompression / compression effects (depending on the construction works) than the sector under the street.

However, as can be seen in Figure 42, there is a 14.40m thick soil layer separating both structures which could imply a relatively long consolidation period after the loads are applied in the construction site and a redistribution of those diminishing the differential effect.

Theoretical models can be executed to predict the strain and tensional state of the underground structure during the building construction period; however, it is hard to reproduce the exact situation and several approximations and assumptions have to be considered regarding soil layers and characteristics, possible consolidation and redistribution of loads, existing structures initial equilibrium states, among others. Therefore, the objectives of complementing the theoretical models and calculations with monitoring tools are ensuring structural safety by:

- Increasing damage detection probabilities by simply observing and assessing the measured data.
- Easing decision making processes in light of damage detection through assessment of historic and present measurements.
- Calibrating the existing theoretical models consequently improving their prediction abilities.

3.3. Monitoring scheme and sensor installation

As mentioned before, the proposed monitoring scheme involves the use of DOFS, concretely, by means of an OBR ODiSI-A (**O**ptical **D**istributed **S**ensor **I**nterrogator) manufactured by LUNA Technologies. After the case study and assessment, Cotca S.A. proposed the attachment, along the accessible underground structure surface, of the sensing optical fiber that allows for continuous measurement of strains with a 1cm resolution.

Even though this SHM tool is relatively recent, the already presented applications, some involving the same company, proved the good performance of DOFS regarding strain measurements in real concrete structures, which led Cotca S.A. to opt for them again.

The following sections will be devoted to, firstly, present the proposed monitoring scheme regarding where to install the DOFS and, secondly, describe the installation process of the optical fiber bonded to the concrete.

3.3.1. Monitoring scheme

The presented monitoring scheme involves the installation of a strain sensing optical fiber bonded to the inner structure of the tunnel for it to reproduce the deformations experienced by the structure due to the unloading / loading processes happening 14.40m above in the construction site. The geometry of such monitoring scheme is presented in Figure 44.

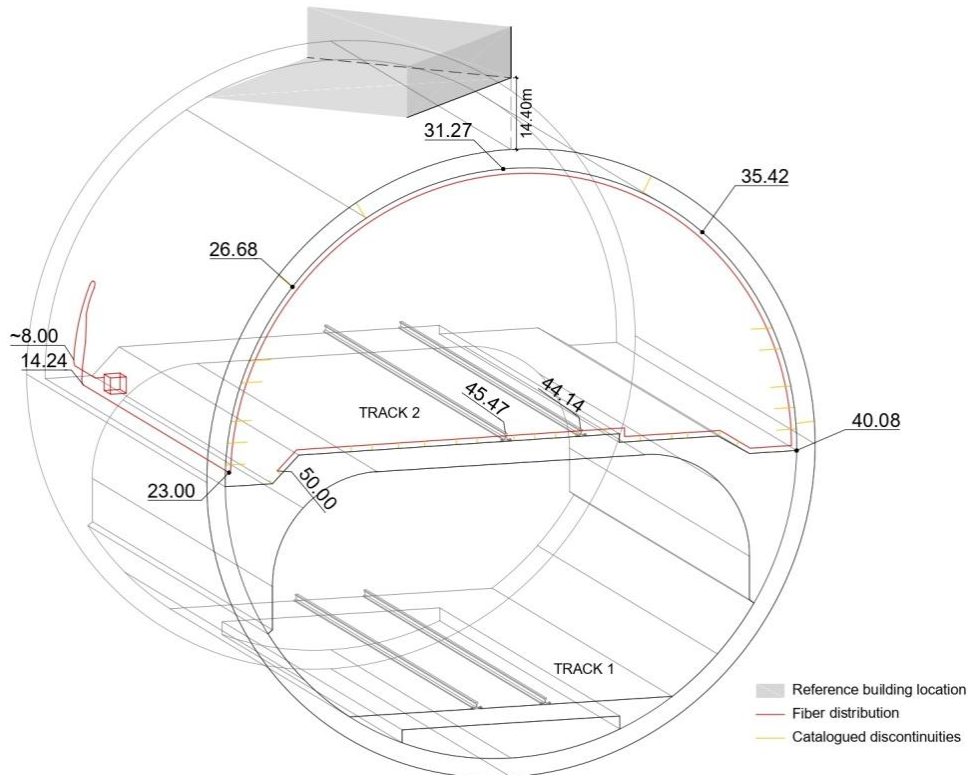


Figure 44. 3-Dimensional representation of the DOFS monitoring scheme

In the previous figure, the optical fiber is represented in red and the numerical values around it are a reference to the distance between the indicated point and the beginning of the fiber, i.e. distance to the monitoring device. The orange lines represent the catalogued discontinuities, which refer to points in which the bonding of the fiber to the concrete surface is not guaranteed mainly due to difficult accessibility. As will be seen in the installation procedure description, these discontinuities are usually found in corners, joints, under rails, behind pipes, among others, preventing the required attachment to the structure from being executed and consequently compromising the quality and reliability of the readings in that point.

Notice that only the structural surface surrounding track 2 is monitored, meaning the upper half of the tunnel ring's inner surface and the upper fiber of the central slab. It is logical to focus on, firstly, the upper track of the structure since the loading effects come from above and, secondly, the inner surface of the structure being the only physically accessible option. However, it might have been more interesting covering the lower fiber of the slab since it is the one in tension and, therefore, prone to crack forming at higher levels than the upper fiber (in compression). However, no kind of drilling procedures performed in the slab to allow the fiber access to the

lower slab surface were permitted by the tunnel structure responsible unit due to safety concerns. Consequently, the attachment of the fiber was performed in the upper surface of the slab.

Locating the DOFS forming a perpendicular plane to the tunnel axis and right under the South-East corner of the building, as seen in Figure 45, appears to be the most logical distribution. The reasons behind are, in the first place, the critical section, i.e. the one expected to suffer larger effects, is completely monitored and, also, since all measured points belong to the same plane, the deformation of the structure is easier to interpret and further computations of convergence based on the measurements can become straightforward.

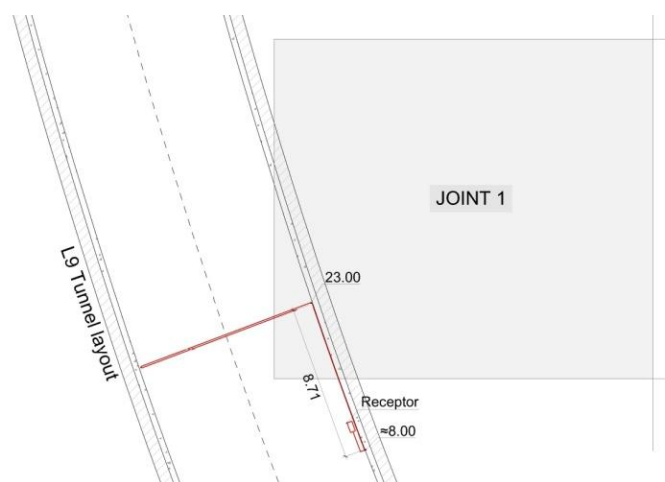


Figure 45. Plan view of DOFS location with respect to building site

The chosen optical fiber length is 50m, which allows for further monitoring length than just the approximately 30m long inner perimeter of the track 2 section. For that, it is proposed to bond the fiber in parallel to the tunnel axis along the side that corresponds to the building for the next 8.71m of fiber. Finally the fiber slightly begins to cover another section and, for the last 8m before the connection to the ODiSI device, it doesn't remain attached.

As commented in the DOFS real applications section, the non attached fiber segments are not reproducing structural strains in the readings along them. However, they are useful to check temperature variations and how the strain readings along the bonded fiber segments are affected by them.

3.3.2. DOFS installation

In order to properly install the optical fiber and ensure its good performance, it has to be appropriately bonded to the structure. The usual procedure implies a delicate preparation of the concrete surface, which, being the nature of the structural material significantly heterogeneous, can become tedious. Firstly, the concrete surface is polished with simple sandpaper to refine existing irregularities present in the fiber's layout. Then, rubbing alcohol and special products against grease, air humidity and direct moisture should be applied on it. The whole fiber length can then be fixed to its position by means of punctual adhesives being later covered by a thin layer of epoxy resin that bonds it to the concrete lining (see Figure 46a).

In the tunnel, as in every other structure, independent management activities take place involving personnel that isn't necessarily aware of the monitoring project taking place in that

section, which means that the installation is at risk of accidental damage. The measuring device and computer can be easily stored and protected from damage in a locked unit. Regarding the fiber installation, protective measures need to be applied to avoid possible damage. In the case study, duct tape was applied covering the whole length of the fiber and additional protective measures were taken regarding the floor, for being a passable area, and the fiber discontinuities, for the presence of punctual non-bonded segments in which physical integrity can be easily compromised (see Figure 46b).

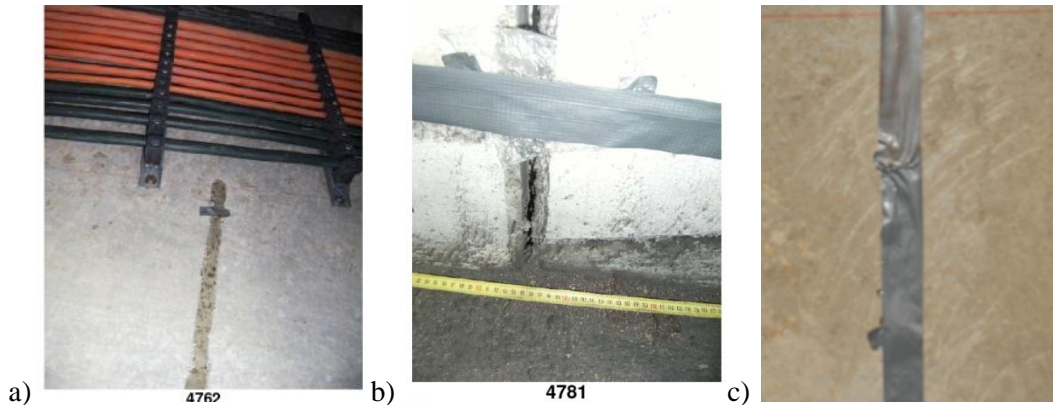


Figure 46. Fiber installation pictures on a) bonding of fiber to concrete surface using epoxy resin (provided by Cotca), b) protection of the fiber in a discontinuity with bubble wrap and duct tape (provided by Cotca) and c) scratching of irregular surface due to cement grout injections prior to fiber installation (own site picture N. 018)

Having to execute these steps along all the fiber installation length means that in some cases heights of approximately 5m had to be safely reached (keystone of the tunnel), for that, a small scaffolding structure was used.

The following images show some of the DOFS deployment results, but only a selection of the available pictures is presented here with the aim of helping through the explanation (a wider and clearer collection of pictures can be found in Annex 1).

Figure 47 presents the optical fiber installation overview close at all times to the guiding red line; the measuring device can be identified in the red box on the right wall of the tunnel. The fiber protective layers are observed as well in the upper surface of the slab and going under the rails.

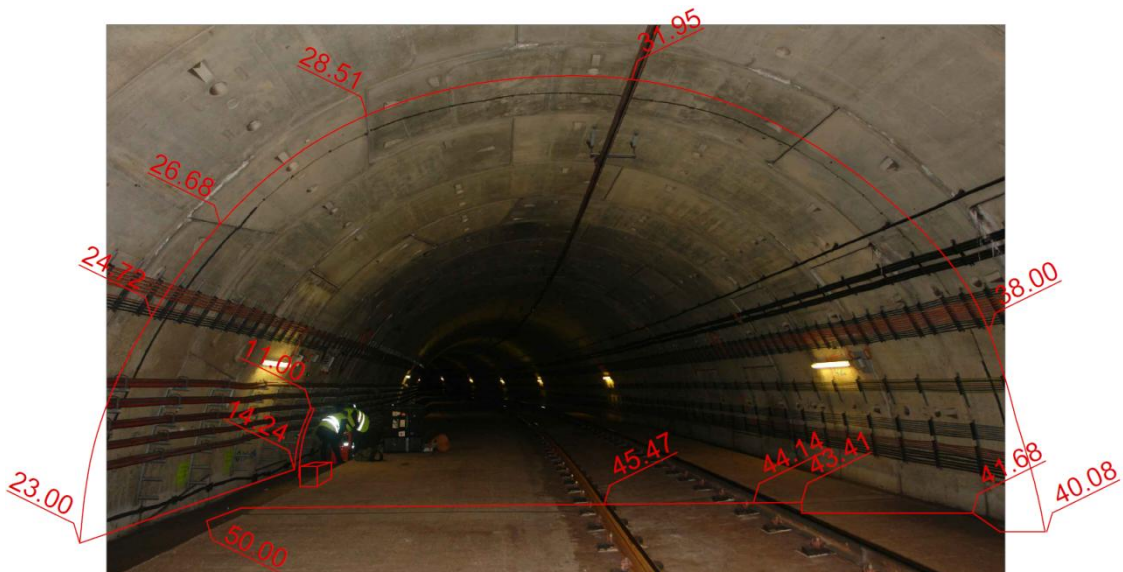


Figure 47. Tunnel monitored section (own site picture N.032)

The optical fiber segment can be seen in the next pictures following its installation from the location 50m till the measuring device.

1. Initial point of the fiber (4731)
2. Under the rail (4739)
3. Corner formed by horizontal slab and tunnel ring (4746)
4. Tunnel's concrete structure and catenary ~5m above slab, notice the clear joints (4765)
5. Tubes and pipes (4768)
6. Corner where the optical fiber changes from sectional / transversal monitoring of the vault to longitudinal monitoring of the tunnel (47469) .
7. Detail of fiber going through a joint (4780)
8. Monitoring equipment (4798)

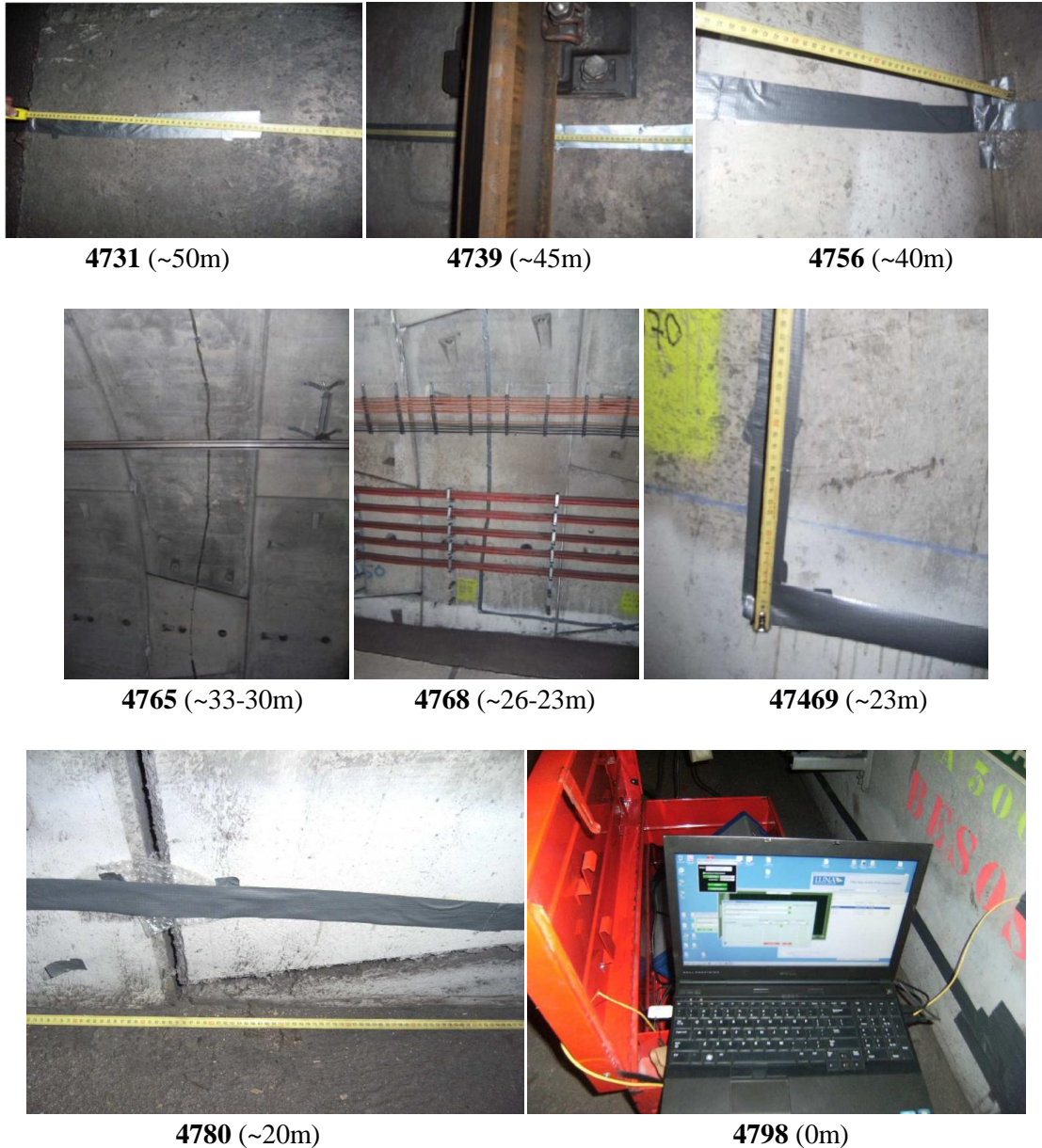


Figure 48. Selection of pictures from the installed DOFS in the tunnel (pictures provided by Cotca)

As can be seen in the figures and in Annex 1, several points of the fiber are subject to bonding discontinuities, that is, lack of attachment to the concrete surface. Since these points are not physically bonded to any surface, the readings performed on them are rather useless and, most

of all, harmful as they significantly affect the obtained strain profiles with excessively large and unexpected peaks.

It is important to mention that the manual measurements on the fiber length (see measuring tapes in the pictures of Figure 48) were executed in order to reproduce accurately the layout of the fiber so that the collected data can be properly interpreted. This enabled as well the cataloguing of bonding discontinuities along the fiber (presented in Annex 1), most shown in the pictures being corners, floor irregularities, steps, joints between concrete elements, behind pipes and bellow rails, which will later allow for the interpretation of unreasonable readings.

The reading quality of these particular points will be later assessed in section 4 where the collected data will be post-processed. However, it must be said that without the discontinuities characterization an important part of the data post-processing would become much more tedious.

3.4. Construction timeline and monitoring period

The construction company provides the **timeline** of the building works through eventual e-mails defining the objective of the following two weeks. Based on the received information, a model timeline has been developed in order to correlate the strain measurements evolution and the construction works taking place and to check if the structure response is consistent with the actions being applied. The schematic model timeline can be found in Annex 3, nonetheless a summary of the main works is provided bellow.

The excavation works started in the 8th October 2018 and in 6th November the 90% of the excavation had been completed supposedly finishing around mid-November. The following actions are classified according to the Joint they belong to with the aim of easing the explanation.

Joint 1 works

The concreting of joint 1 foundation slab was finished by the 20th December 2018 and the execution of the basement walls and pillars and **Ground Floor Slab (GFS)** by 14th February 2019. Between 2nd March and 5th April the ground floor walls and pillars and the **1st Floor Slab (1FS)** were completed as well as the formwork of the first floor. Finally, by the 18th April the **2st Floor Slab (1FS)** was completed.

Joint 2 works

The joint 2 foundation slab was completed around the 11th January 2019 and by the 18th March the structure of the basement floor was finished together with the **Ground Floor Slab (GFS)**. The formwork and reinforcement installation of the **1st Floor Slab (1FS)** is supposedly accomplished by 18th April.

Joint 3 works

The joint 3 foundation slab was completed by the 18th Marc 2019 and the basement floor walls and pillars and **Ground Floor Slab (GFS)** by 18th April.

A visual scheme is presented in representing schematically the mentioned works after the excavation conclusion around 9th November.

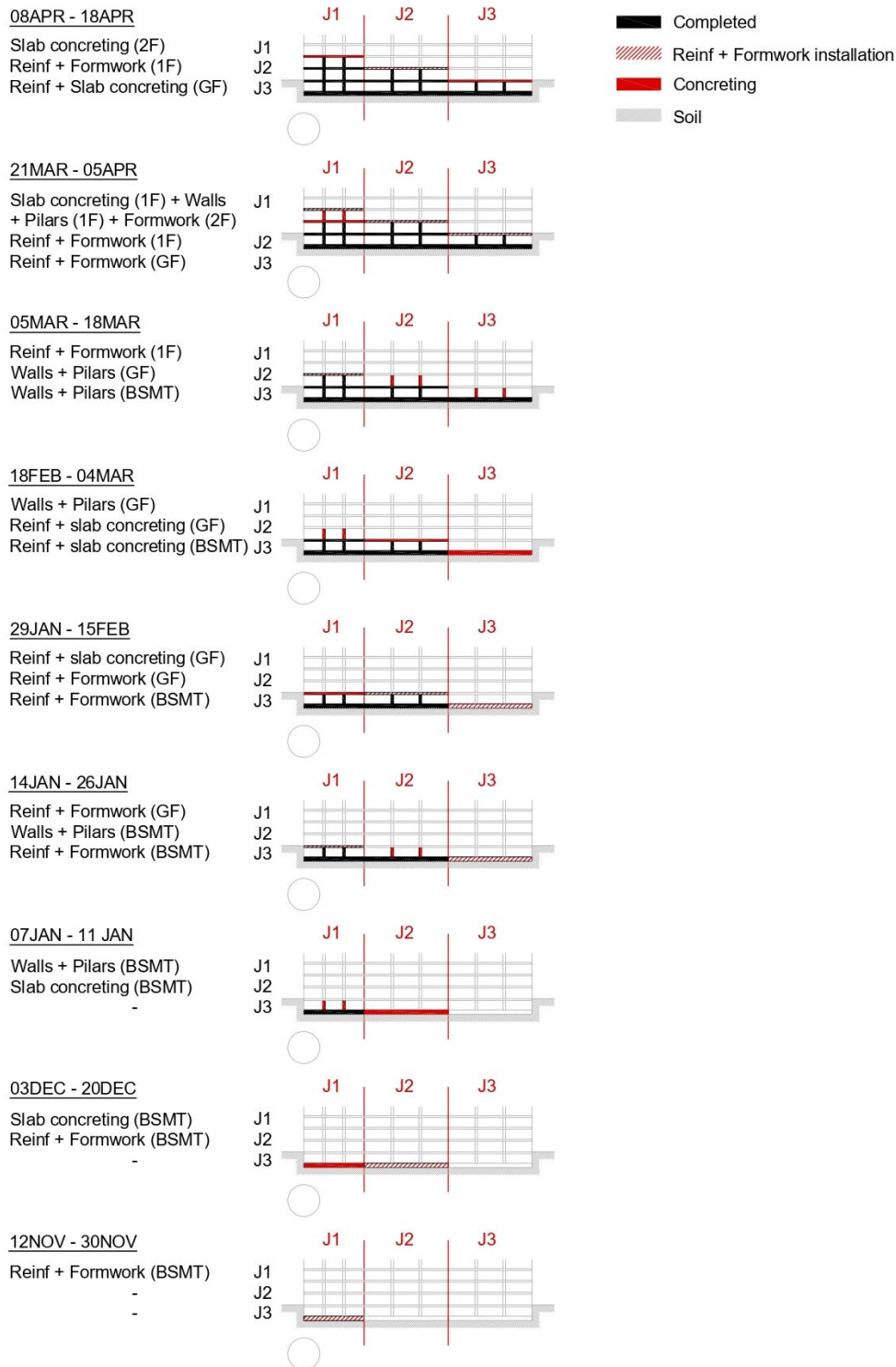


Figure 49. Construction time-line (adapted from data provided by Cotca S.A.)

Notice firstly that, all works start being executed in the area corresponding to joint 1 (the one located right above the tunnel layout) and that, as can be seen in the works description, joint 1 is the most advanced in terms of constructed surface at all times. The main reason behind this constructive scheme is safety assurance. Indeed, joint 1 is the site zone that will have the largest repercussions on the tunnel structure given its location. Therefore, it might be helpful starting with it because, in an eventual case of ‘failure’ (understood as a particular strain threshold being exceeded on the tunnel ring’s inner surface), it would be easier to return to the previous equilibrium state than in the case of having joint 2 and 3 developed at the same level as joint 1.

Additionally, given that the excavation is one of the main actions applied to the soil and, consequently, to the tunnel, it is interesting to refill that ‘void’ by constructing firstly over joint 1 to oppose the decompressive action of the excavation. This would allow returning to an equilibrium state that is similar to the initial one and reducing the time interval in which the tunnel structure has to work under conditions that might not have been accounted for during its design phase.

Note as well that there is a significantly low construction activity in joints 2 and 3 during the period from 19th February and 18th March, which may be reflected in the readings in the form of a reduction in the strain evolution slope.

It is important to mention that the time interval between a construction work being executed, i.e. an action being applied on the soil, and a response being perceived in the strain readings can be very wide. Indeed, we are supposedly talking about a 14.4m thick clayey soil layer separating the building foundations and the tunnel concrete lining, which translates into a long consolidation period before the load is transferred to the tunnel structure.

The **monitoring periods** are defined with the aim of covering the main construction periods separately: excavation, foundation, execution of ground floor, first floor, etc. It is not necessary to evaluate the whole construction period continuously given that the separate measures can already give the strain evolution tendency by interpolation of the missing intervals.

It has to be considered as well that the expensive measuring device and software, belonging to Cotca S.A., is part of other projects / laboratory tests on which the company is simultaneously working. Therefore, the tunnel non-monitoring periods are used by the company to cover other projects.

The monitoring intervals of this case study are presented bellow and they are explicitly marked in the model timeline of Annex 3 for a better visualization on the determined actions the structure was enduring when monitored.

- From 4th October to 7th October: every **30 minutes**.
- From 18th October to 7th November: every **6 hours**.
- 13th December: 2 measurements separated by **30 minutes**.
- 24th January: 2 measurements separated by **30 minutes**.
- From 21st February to 25th March: every **15 minutes**.
- From 16th April to 17th April: every **30 minutes**.
- 17th May: 5 measurements separated by **10 minutes**.

The December, January and April monitoring periods will be commented in particular given their problematic outcomes.

The very first reading records the initial state of the fiber (baseline measurement) measuring and storing its Rayleigh scatter signature. All the following measurements are displayed as a difference relative to the baseline when the fiber’s physical length and index of refraction experience changes due to temperature or strain variations.

The initial readings, recorded during the days preceding the start of the excavation works, that are **4th and 7th October**, allow for an evaluation of the tunnel initial state, i.e., the factors that affect the structure in its normal service state. External effects that might be detected in this

period prior to the beginning of works at ground level involve, mainly, metro traffic, if caught in any measurement. Even though no works are being executed in this period, it would be possible to observe other variations due to fiber installation discontinuities, particular locations where the fiber is not completely bonded to the structure, or anomalies, excessively large measures with no physical meaning, being both non-reliable readings in terms of mechanical interpretation.

The excavation monitoring period, taking place from **8th October to 9th November**, aims to record the effects of the excavation works on the structure and is, therefore, comprised between 18th October and 7th November.

During the **December 2018** monitoring period, the measurements should have covered two weeks (at the least) which would have included the reinforcement and formwork installation of the foundations and the concreting of the Joint 1 foundation slab.

The **January 2019** monitoring period should have covered the execution of pillars and walls on the basement floor in joint 1 and the reinforcement and formwork installation of the **Ground Floor Slab (GFS)** in joint 1 and of the foundations in joint 2.

However, reading failures significantly affected the two aforementioned monitoring periods. The failures' causes remain undetermined for each case; however, they all implied a rebooting process regarding the measuring instrument (Optical Distributed Sensor Interrogator) or the attached laptop PC which translated into the ongoing monitoring process being interrupted and cancelled. The reading failures mainly happen as a result of voltage dips, direct disconnection from the electricity grid due to maintenance procedures in the tunnel or even, a punctual failure of the measuring devices themselves.

These failures would not be much of a problem if the monitoring processes were to be continuously checked which gives light to the main inconvenient this project has had to face. The main drawback was clearly the lack of wireless accessibility to the measuring device of any sort of warning process that would have enabled a real-time check of its performance, the detection of failures and the wireless download of stored data and the consequent repairing actions to avoid the loss of data.

Since no wireless connection could be provided at the time (that particular metro line segment does not yet include optical fiber network), physical access is the only remaining option to check the measuring instruments and download the recorded data. However, this alternative is complicated given that the location of the monitoring section is in a metro tunnel. The accessing personnel have to withstand schedule restrictions making night-time (from 2am to 5am, when the trains are not running) the only available time interval for access. Other factors, like ongoing maintenance operations in the tunnel and access protocols and restrictions established by TMB do not facilitate the procedures either.

The second to last monitoring period comprised in this thesis includes the **end of February and most of March**, which would cover the execution of the **1st Floor Slab (1FS)** of joint 1, basement floor and **Ground Floor Slab (GFS)** in joint 2 and foundations of joint 3. The repercussions of the 'non-monitored' previous works regarding December and January will logically add up to the readings of this period and an approximated profile will be extracted for them.

Note that during this period, as mentioned before and as reflected in the model timeline (Annex 3), there is a reduction of construction activity in joints 2 and 3. That might be reflected in the readings in the form of a tendency variation in the strain evolution posterior to the 21st February (as the soil takes time to consolidate and transmit the load to the structure of interest).

Finally, the **mid-April** monitoring period is the last one comprised in this thesis. The device was supposed to cover a month of construction works after the 16th April with readings every 30 minutes, however, as happened with the December and January periods, the device failed due to undetermined reasons when two days had passed after the setup. Luckily, the recordings of the two initial days were recovered in the programmed data collection visit a month later. Even though being very short, this period allows for the underground structure control regarding the construction of the **2nd Floor Slab (2FS)** of joint 1 and the **Ground Floor Slab** in joint 3 as the strains tendency can still be interpolated.

In the programmed data collection visit of the last monitoring period, in **17th May**, I, as the author of this thesis, was allowed access to the tunnel to actually see the object structural monitoring project of this thesis. In that date, some of the photographic content presented in this thesis was acquired and the monitoring software was re-started computing five extra readings on site in order to check the current structure state and the effect of the works executed during the end of April and beginning of May.

All in all, given that there are no expectations of serious structural failure, the fact that some of the intended monitoring periods were not accomplished is not crucial. The aim of the study is to evaluate the tunnel's structural response and, for that, the non-monitored period's response can be extrapolated through theoretical models and the tendencies of posterior readings. The only issue that these missing / very short monitoring periods arise is the increased difficulty regarding the assessment of the effect of particular works, such as the execution of the foundation and floor slabs, on the tunnel.

3.5. Data collection: reading software and DOFS measurements

The strains along the tunnel ring's inner surface and slab's upper fiber are being monitored through a 50m long DOF sensor (bonded to the concrete surface) by means of an OBR ODiSI-A (**O**ptical **D**istributed **S**ensor **I**nterrogator) manufactured by LUNA Technologies [41]. The ODiSI uses swept-wavelength coherent interferometry to measure temperature and strain using optical fiber as a sensor and it offers the possibility to test the structure at numerous specific points of interest over the required extended area with user-configurable sensing locations and gauge lengths.

The spatial resolution selected for this case study is **10mm** and the time interval between measurements depends on the monitoring period (see previous section).

The software will then provide strain measurements along the whole length of the fiber with a resolution of 1cm and for every corresponding time. It has to be considered that, while the commercial fiber length is defined as 50m, its sensing length is slightly longer (50.23m) as can be seen in the extracted data and in Figure 50.

Figure 50 presents a typical strain reading in a particular time (in this case, it is one of the initial measurements from the 4th October). It can be observed that the behaviour of the first ~10m of fiber is different than the rest because, as mentioned in the monitoring scheme section (3.3.1),

the first 10m are not bonded to the structure and its purpose is, rather than providing accurate strain readings, being able to identify changes in the measurements due to external factors (mainly temperature).

The different segments of the fiber are shown as well, being the longitudinal ring segment the one deployed in parallel with the tunnel axis and the transversal ring and slab segments the ones installed in the tunnel axis perpendicular plane under the building construction site. One can already start seeing that the longitudinal segment is subject to more irregularities than the others which makes sense given that the fiber deployment in this area came across several physical discontinuities (see Annexes 1 and 2). However, the data will be analysed and interpreted further on in the results section where the behaviour of each segment will be evaluated in detail.

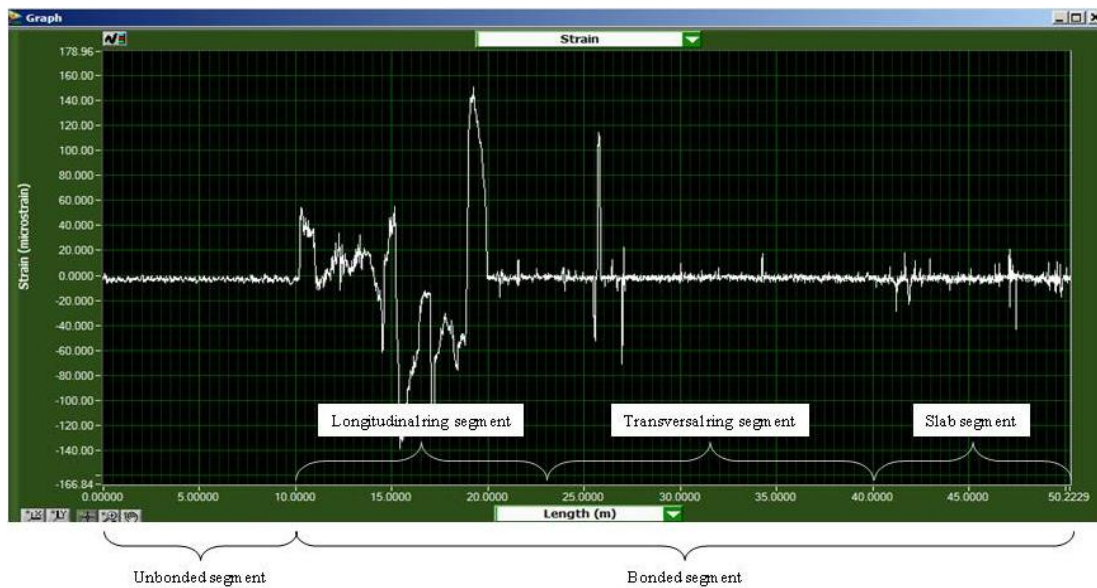


Figure 50. Typical strain measurement for a particular time [from Graph window in ODiSi software].

The raw data is exported from the monitoring software as a file with .odb extension and using the conversion program provided by LUNA Technologies (ODiSi-B Post Processor Software) a .txt file with strain (or temperature) measurements is obtained. The initial part of the .txt file includes the specifications of the measurements that have been executed (see Figure 51).

```

04october_default channel_Strain.txt: Bloc de notas
Archivo Edición Formato Ver Ayuda
Header Lines 43
<?xml version="1.0" encoding="UTF-8" standalone="yes" ?>
<!DOCTYPE boost_serialization>
<boost_serialization signature="serialization:archive" version="9">
<InstalledFiber class_id="0" tracking_level="1" version="3" object_id="_0">
  <Name>tunnel9</Name>
  <SerialNumber>F502017LUNA006761</SerialNumber>
  <Length_ns>495.94644</Length_ns>
  <GroupIndex>1.4801</GroupIndex>
  <LastConfig>default profile</LastConfig>
  <Location_ns>18.077715</Location_ns>
  <StrainCoeffs>
    <count>5</count>
    <item>0</item>
    <item>-6.6680002</item>
    <item>0</item>
    <item>0</item>
    <item>0</item>
  </StrainCoeffs>
  <TempCoeffs>
    <count>5</count>
    <item>0</item>
    <item>-0.80138773</item>
    <item>0</item>
    <item>0</item>
    <item>0</item>
  </TempCoeffs>
  <Port>0</Port>
</InstalledFiber>
<Channel class_id="1" tracking_level="1" version="3" object_id="_1">
  <Name>default channel</Name>
  <Color>16777215</Color>
  <ChannelType>0</ChannelType>
  <MeasurementType>0</MeasurementType>
  <Baseline>LineaBase04oct2018</Baseline>
  <RemapLocation_ns>0</RemapLocation_ns>
  <Orientation>0</Orientation>
  <StartLocation_ns>0</StartLocation_ns>
  <EndLocation_ns>495.94644</EndLocation_ns>
  <GaugeLength_cm>1</GaugeLength_cm>
  <Spacing_cm>1</Spacing_cm>
</Channel>
</boost_serialization>

```

Figure 51. Introductory strain reading specifications in exported .txt file.

The main considerations one has to take into account regarding the initial code are the optical fiber name and serial number (which will allow for posterior identification of the file), the baseline measurement considered and the defined gauge length and spacing of the measurements. These must be checked every time the newly extracted data is aimed to be post processed, since these devices are used simultaneously in different projects and measures could become accidentally mixed up.

Finally, following the initial introduction, the exported file presents the measuring locations of the fiber, from 0m to 50m separated by 1cm, and, below, the collected data is displayed with each reading being preceded by the date and time of the measurement.

The final processed data is transformed and represented in the form of matrices in order to facilitate the required post-processing using the matrix based computer environment known as Matlab [68]. The set of data has 3 main components whose definitions are complemented by Figure 52.

- Length vector

5023x1 vector with components from 0.00m to 50.23m every 0.01m representing each sensing point along the fiber where the measurements have taken place.

- Time vector

Column vector whose dimensions depend on the measurements that have been processed up to the present time. At the end of this master thesis, i.e. after the monitoring periods comprised between 1st October 2018 and 1st June 2019, the dimensions of this vector were 3290x1. Each component of this vector specifies the date and time of the performed measurement and has the following form: 2018-10-04T01:20:19.289892 (meaning reading performed on October 4th at 1:20am).

- Strain matrix

Matrix that comprises the strain readings along the whole fiber for a particular time in each row. As mentioned before for the time vector, at the end of this project the matrix dimensions were 3290x5023.

A part from strain readings, the previously mentioned software allows for **Spectral Shift Quality (SSQ)** measurements as well. The SSQ is described by the software providers, as a measure of the strength of the correlation between the measurement and baseline reflected spectra as in Equation 1 below.

$$SSQ = \frac{\max(U_j(v) * U_j(v - \Delta v_j))}{\sum U_j(v)^2} \quad (2)$$

where:

$U_j(v)$ is the baseline spectrum for a given segment of data

$U_j(v - \Delta v_j)$ is the measurement spectrum under a strain or temperature change

* is the cross-correlation operator

In other words, it is a function that determines the quality/reliability of the strain reading by correlating the original baseline measurement and the measurement spectra normalized by the maximum expected value. According to its definition, the SSQ value will then remain between 0 and 1, where 1 translates into perfect correlation and 0 into uncorrelated. LUNA Technologies [41] states that data sets will be accurate if the SSQ is above about 0.15; if it is lower, it is very likely that the strain or temperature change has exceeded the measurable range.

The software then provides an additional set of data, the SSQ matrix, in the form of a matrix with the same dimensions as the strain matrix and whose components are the SSQ values associated to each strain reading.

In this thesis, the SSQ function is used during the strain readings post-process and is proposed as one of the tools that enables any user to effectively classify the obtained measurements depending on their reliability and allows for a reliable post-process.

The final data to be post-processed and analysed is schematically presented in Figure 52.

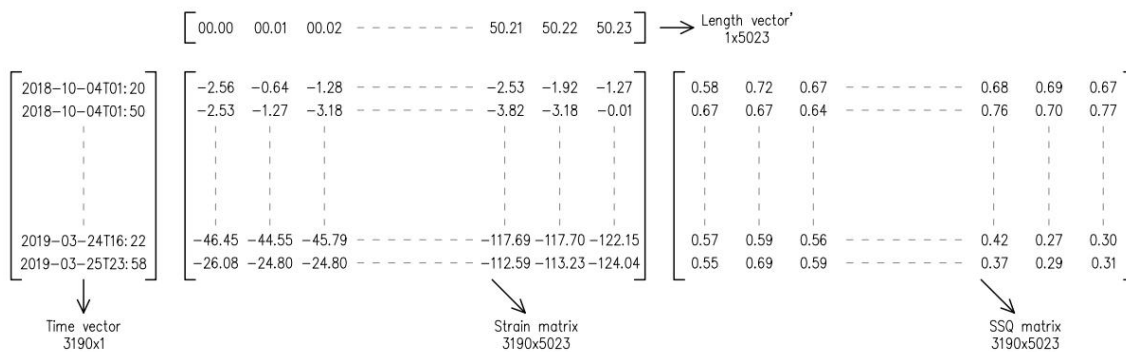


Figure 52. Exported data in the form of vectors and matrices for post-processing.

4. DOFS strain readings post-processing

The first step right after the DOFS measurements are completed and all the strain data is collected is to study and post-process the collected readings. As can be seen in Figure 53, the raw strain data can be hard to interpret due to the presence of excessively large peaks. It can be deduced even though an initial tendency towards compression from dark red to dark green (which seems to be the lowest measurement) and then going up with the lighter greens reproducing decompression. However, nothing else can be deduced from that.

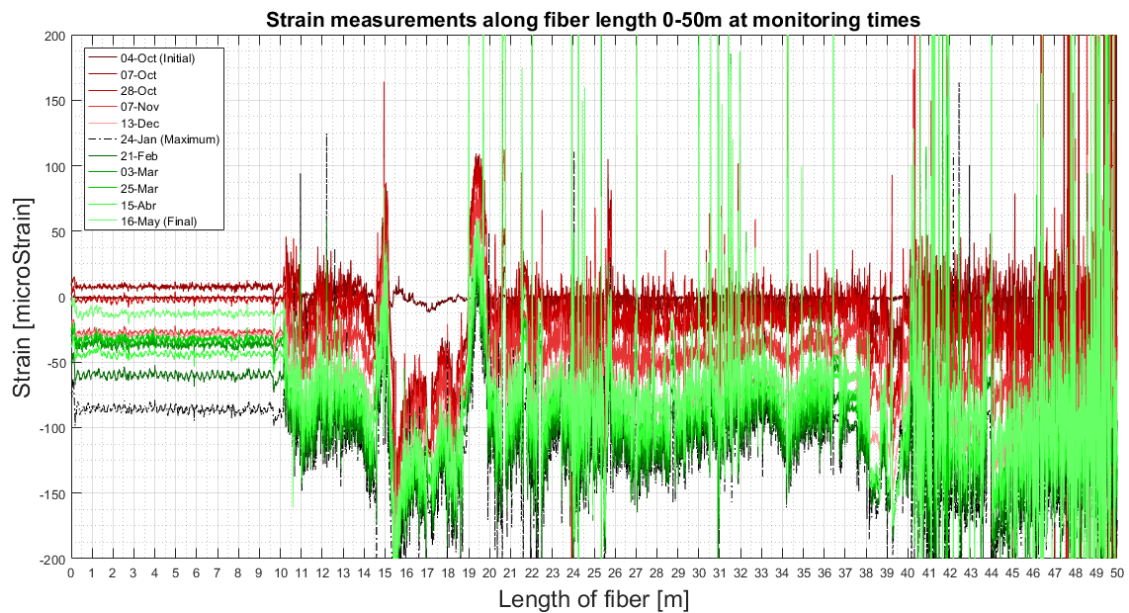


Figure 53. Typical strain measurements covering the whole analyzed monitoring period

This section of the project is aimed at transforming DOFS raw strain measurements to a more trustworthy and interpretable set of data. As mentioned before in the introductory section of this thesis and stated by Bado et al. [48], DOFS are currently prevented from becoming a reliable universal strain-reading method mainly because of two reasons: the lack of a reliable DOFS/structural support bonding technique and the frequent appearance of anomalies in the measurements in the form of abnormally high strain peaks that distort the strain profiles.

Since the mentioned peaks, either due to bonding or reading failures, prevent the possibility of getting reliable measurements in their location and time and their immediate surroundings, they should be avoided and/or deleted in the data post-processing phase. With the aim of counteracting the effect of the lack of bonding in the critical zones of the fiber installation (corners, joints, under rails, behind pipes, among others) an initial peak analysis is executed and detailed in the following section. After that, the amount of Strain Reading Anomalies (SRAs) in the set of data at our disposal will be reduced by developing and applying a post-processing algorithm presented in section 4.2 and 4.3.

4.1. Peak analysis

Firstly, an analysis of the collected data has to take place. The objective is to identify possible anomalies in the readings caused by existing discontinuities in fiber installation, that is, critical locations of the monitored structure where the effectiveness of the bonding technique might have been reduced or where the spatial conditions did not allow for it to be applied at all.

This initial analysis is carried out identifying and correlating measured strain peaks with catalogued discontinuities during the installation (see Annex 1).

The peak analysis takes place after each monitoring period to check if the appearing new strain peaks coincide with catalogued discontinuities, which would explain the abnormally high value, and to verify the behaviour of the peaks that have already been identified and characterized in the previous periods.

A part from the peaks identification (when and where do they occur), for which an algorithm has been developed, this part of the data treatment is not automated. The peaks have to be studied independently because they are all different, only the ones in close proximity (temporally or locally) can be considered as a result of the same event or cause.

One has to consider as well that not every installation discontinuity is catalogued given that it might not have been detected during the deployment of the optical fiber or due to a posterior failure of the bonding technique in certain locations. Therefore, uncharacterized peaks could still be the result of existing DOFS/structural support discontinuities. However, given that these “missed” peak locations will still be characterized by an abnormal behaviour, they will still be detected and treated in the next treatment phase (explained in detail in sections 4.2 and 4.3).

What is considered as an abnormal value?

In this particular case study, given the loading conditions of the structure, one can assume that high variations of strains between two consecutive readings are abnormal. That situation is usually characterized by sudden loading variations, which is not at all our case, and moreover considering the 14.4m thick layer that separates the load application surface and the structure of interest.

Considering the loading and geometric conditions of the case study, high strain measurements are not expected either. A range of $\pm 200\mu\text{strains}$ can be considered as a generous interval in which the strain readings along the fiber should remain. Consequently, for the available set of data a threshold of $200\mu\text{strains}$ is established as to define an abnormal peak, i.e. a peak to analyse.

Utility of the peak analysis

After an in depth study of most of the readings a correlation can be found between some data peaks and the location of the catalogued discontinuities. Of course, as mentioned in the introduction of this section, not all peaks are explained through this theory; these will be treated further on.

With the purpose of easing the peaks interpretation, a listing of the catalogued discontinuities regarding the fiber bonding and their locations has been developed (see Table 2 and Table 3) and is complemented by Figure 54 and Figure 55, which present the defined discontinuities on the fiber layout.

Table 2. Catalogued discontinuities list (cross section)

Location [m]	Discontinuity ID	Location [m]	Discontinuity ID
49.52	01: Corner	40.08	08: Corner
50.00-40.00	02: Slab's irregular surface	39.58	09: Concrete segment joint
45.47	03: Rail	39.50-38.60	10: Tubes

44.14	04: Rail	34.03	11: Concrete segment joint
43.50	05: Step	28.51	12: Concrete segment joint
41.68	06: Corner	26.68	13: Concrete segment joint
40.98	07: Corner	25.70-23.75	14: Tubes

* Additional care has to be taken between fiber lengths 40-50m and in regarding peaks since the bonding concrete surface in the slab presents superficial irregularities for not being prefabricated.

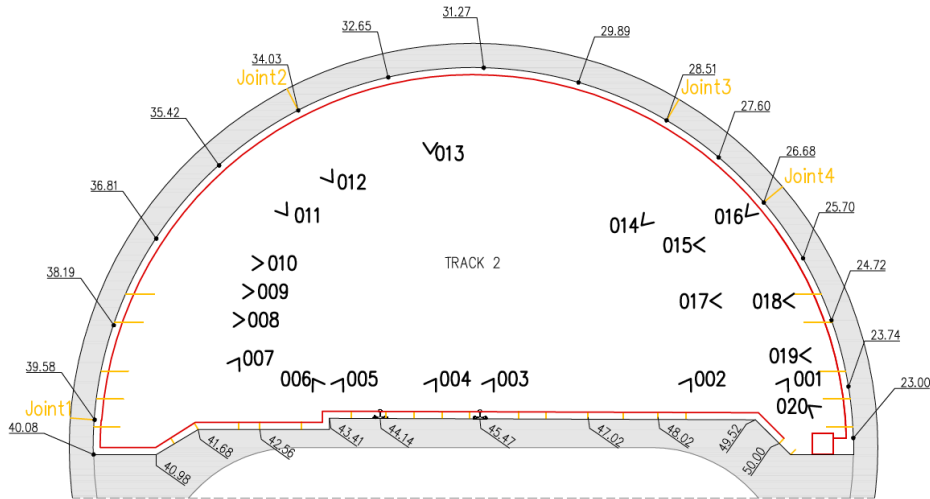


Figure 54. Catalogued discontinuities in tunnel cross section fiber layout (from Annex 1)

Table 3. Catalogued discontinuities list (elevation view)

Location [m]	Discontinuity ID	Location [m]	Discontinuity ID
23.00	15: Fiber turn	18.55	19: Concrete segment joint
22.05	16: Concrete segment joint	16.75	20: Concrete segment joint
21.25	17: Concrete segment joint	14.95	21: Concrete segment joint
20.35	18: Concrete segment joint	14.24	22: Fiber turn

* Additional care has to be taken between fiber lengths 14-23m regarding peaks since the bonding concrete surface presents superficial irregularities due to injected cement grout.

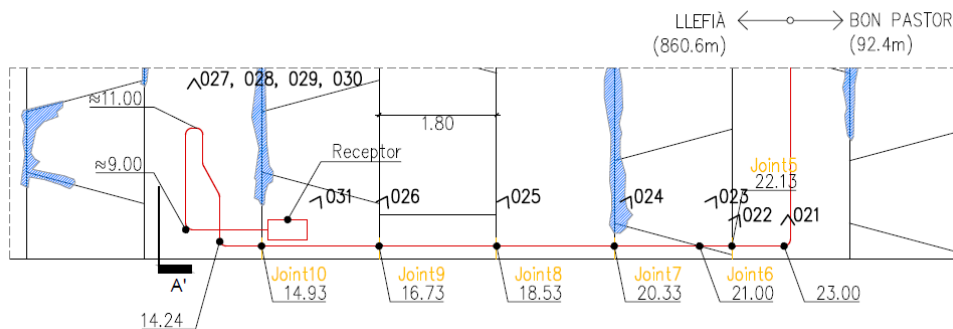


Figure 55. Discontinuities in longitudinal tunnel segment of fiber layout (from Annex 1)

The presented listing is later cross-related with the observed strain peaks locations. In order to identify the peaks of the collected data, an algorithm that localizes the strain peak both in terms of time and space has been developed. Figure 56 presents a typical outcome of the peaks identifying algorithm, which, in this view is locating one lonely peak at point 14.59m and a group of peaks in length interval 15.34-15.77m.

1	2
1 14.5999	[110.8888, -233.4520; 110.9079, -237.2730; 169.0546, -200.3970]
2 15.3399	7x2 double
3 15.3499	9x2 double
4 15.3599	8x2 double
5 15.3699	[110.9079, -201.0050]
6 15.3799	[110.9079, -205.4430]
7 15.3899	373x2 double
8 15.3999	3154x2 double
9 15.4099	3169x2 double
10 15.4199	3184x2 double
11 15.4299	2648x2 double
12 15.4399	3139x2 double

1	2	3
1 110.8888	-233.4520	
2 110.9079	-237.2730	
3 169.0546	-200.3970	
4		
5		
6		
7		
8		
9		
10		
11		
12		

1	2	3
1 168.9608	-202.9200	
2 168.9712	-202.3120	
3 168.9817	-204.2040	
4 168.9921	-205.4480	
5 169.0025	-204.8490	
6 169.0129	-207.3600	
7 169.0233	-207.9890	
8		
9		
10		
11		
12		

Figure 56. Peaks identifying algorithm

The advantage that this algorithm provides is that it creates an initial matrix of 2 columns (left matrix in Figure 56) where the location of the peak is presented in the first column and the second column includes a sub-matrix which stores the time when that peak occurred and the strain value it reached at that time (the two right matrices in Figure 56 show the sub-matrix of the two first peak locations). Sometimes, the peaks occur randomly with no actual physical explanation and usually presenting punctual high readings but not many. Other times, peaks occur during a long time interval. In this analysis, we are looking for those that present irregular behaviour at most of the monitoring times since those would identify a location where the fiber does not present restrictions regarding movement and, thus, a bonding discontinuity.

This algorithm will be used to identify bonding discontinuities in the collected data in order to have them in mind when interpreting the results.

It is worth noticing that Table 2 and Table 3 present only one measure for each discontinuity, however, it has to be considered that the fiber measuring resolution is 1cm and that most discontinuities will affect longer segments than that resolution. Therefore, the surroundings of the listed critical locations can be subject to strain peaks as well, as can be seen, for example, in the following arbitrary reading.

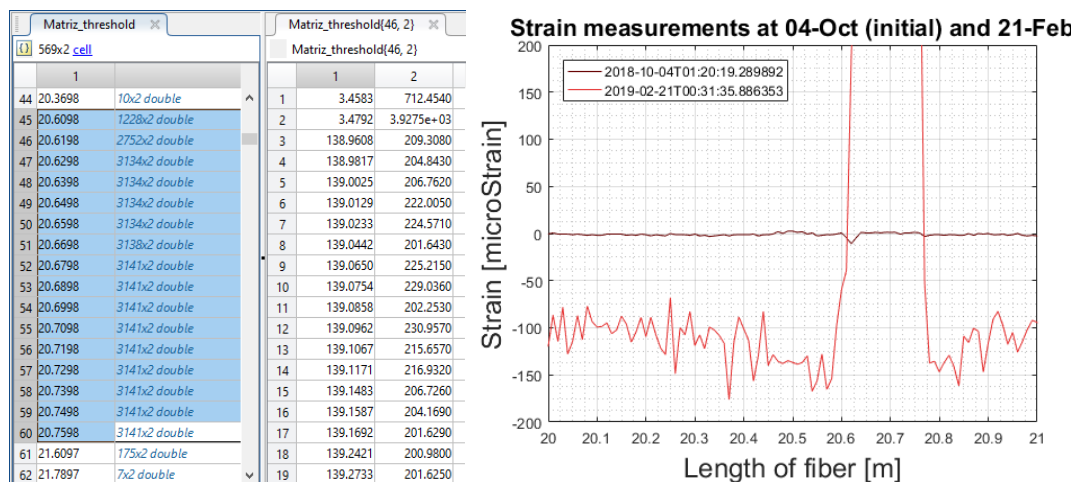


Figure 57. Particular peaks in a 20cm interval

Additionally, one must have in mind that the catalogued discontinuities might not have been exactly allocated given the given the installation conditions. Therefore, the layout might not exactly reproduce the locations of the discontinuities but it can be used as an orienting tool. For example, the presented particular peak found between 20.60m and 20.75, could actually belong to discontinuity number 18 located close to length 20.35m.

As long as it is possible, providing an accurate fiber layout is crucial to ease the data interpretation and post-process.

The following image correlate two strain readings and their characteristic peaks in red with the critical locations presented in Table 2 and Table 3 in blue. Some of the shown discontinuities are clearly located on or really close to particular measured peaks proving that they are related and, consequently, that these are unreliable readings due to bonding discontinuities.

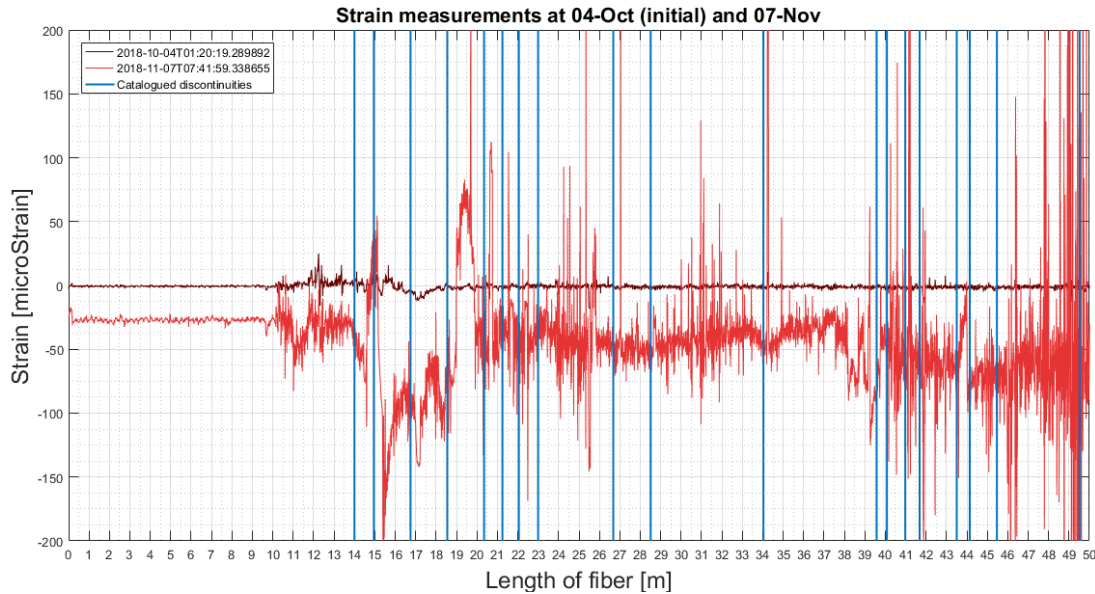


Figure 58. Strain reading along fiber in 4th October (initial measurements) and 7th November

Apart from peak identification and characterization, this analysis allows for an important procedure inside the treatment phase, which is calibration of the fiber layout. It is a fact that any real application of a particular technology implies higher room for error than the corresponding laboratory tests, which are executed in a controlled environment and comfortable conditions regarding lighting, temperature, timing, accessibility to the area to be monitored, among others. Therefore, the discontinuities cataloguing process might be affected and in need for calibration.

The calibration can be accomplished after conducting an in depth analysis on the correlation between measured strain peaks and catalogued discontinuities by observing the particular offset present between them.

4.2. Strain Reading Anomalies (SRAs)

In Bado et al. [48] and various publications preceding it (for example, Barrias et al. [69]), all based on experimental testing of DOFS as a monitoring tool, the appearance of Strain Reading Anomalies (SRAs) has been reported in the form of localized and excessively large strain readings which do not present a direct physical explanation.

The described strain peaks are usually considered as abnormal readings because of the large difference they present with previous readings, both in terms of time and space. Temporally speaking, two consecutive measures should present similar strain readings when the time interval, and thus the load difference, between them are almost negligible. On the other hand, considering that the resolution ranges in the cited experimental tests are around 5-10mm, opposite strain peaks being reported in two neighbouring readings are illogical given that short

distances between two consecutive and co-existing sections translate into a homogeneous behaviour (either tension or compression). Another reason that can trigger the consideration of a reading as abnormal could be the appearance of large tensile peaks in a theoretically compressed area of the structure and the other way around.

All these reasons suggest that these anomalies are reading errors from the DOFS, fact that is confirmed in Bado et al. [48] when complementing a DOFS-monitoring experimental test with other monitoring tools (strain gauges) and theoretical models, which did not explain nor present the peaks read by the DOFS.

There is little research regarding why these reading errors causing the anomalies occur considering the frequency of their appearance in OBR models. According to Ding et al. [70] DOFS reading anomalies are normally caused by a localized failure of the algorithm that tracks the light impulses through the range length under analysis and during a particular wavelength sweep. The SRAs may be caused as well by punctual alterations of reading factors such as the gauge length and the spacing set.

In addition, it has to be noted that in this case study DOFS are not bonded to a homogeneous material, on the contrary, concrete constitutes the tunnel's ring and slab and it has quite a heterogeneous composition which has to be added to the present discontinuities of the structure (cracks, joints, corners, among others). Even though the concrete lining segments are prefabricated some areas are superficially covered by cement grout from the executed injections which induce irregularities in the same way as poured concrete areas like the slab. This physical elements and mechanisms characterizing the case study might affect the fiber's readings as well regarding the anomalies.

4.2.1. Types of anomalies

In Bado et al. [48] two types of strain-reading anomalies are identified:

- **Harmful Anomalies (HF-SRAs)**
Strain peaks characterized by being followed by additional anomalies from their initial appearance and for the rest of the monitoring period. The strain measurement in this type of SRAs can sometimes be correlated to a high SSQ value given that the trend of this location, while including abnormally large values when compared to the rest of strain profiles, increases gradually with time and consistently with the load applied. Therefore, it could be interpreted as a coherent response if the surrounding points had similar tendencies. Note that this kind of anomalies might be contagious, meaning that the surroundings of an identified HF anomaly might become, in posterior times, an HF-SRA itself.
- **Harmless Anomalies (HL-SRAs)**
Oppositely to the harmful anomalies, these are strain peaks that, while preventing the correct reading of the strains at a specific time, still allow it later. Being the nature of this anomaly punctual in nature, it is easily identifiable in the strain profile of a section as an excessively large and punctual peak surrounded by coherent strain readings.

The theoretical definition of the characterized anomalies is graphically represented in Figure 59.

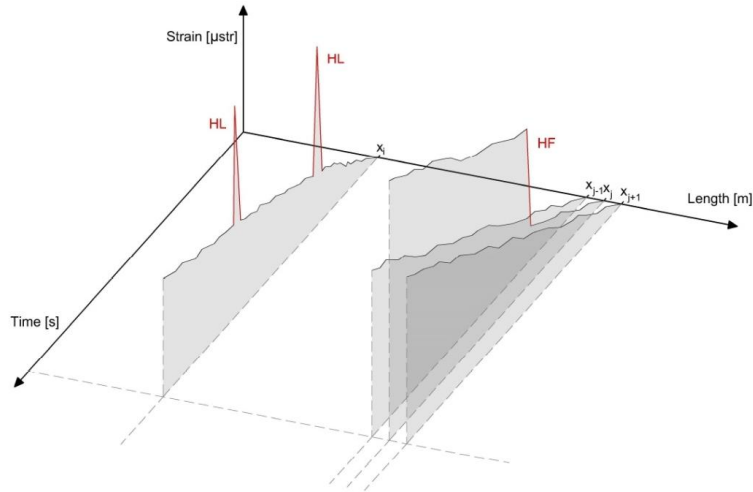


Figure 59. Graphical representation of SRAs' theoretical definition

Some visually identified anomalies in the tunnel's set of data are shown as an example in Figure 60, which represents the same graph seen from different angles. As can be seen, the strain peaks can either be positive or negative, therefore SRAs are observed in both sides of the graph. This graph represents the collected data from 4th October till 7th November, i.e. the beginning of the monitoring process. One can already appreciate the formation of HF anomalies which will theoretically remain for the rest of the monitoring period (as seen in Figure 61).

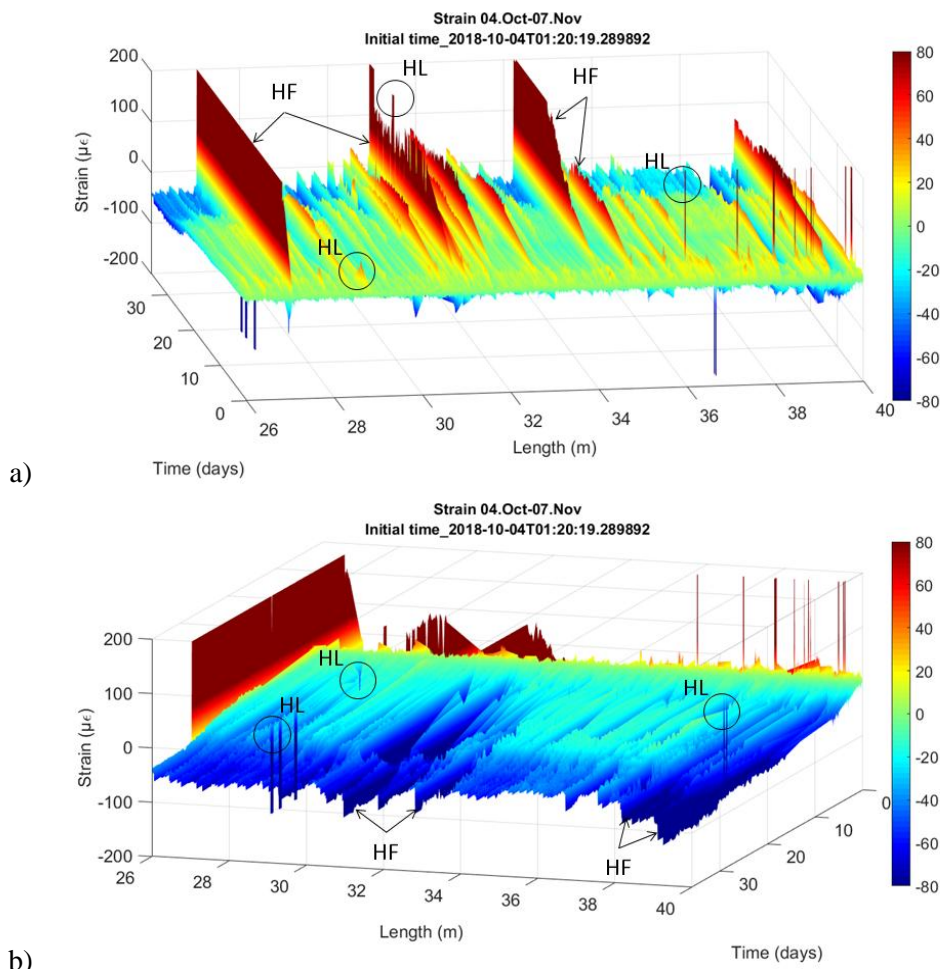


Figure 60. Example on HF and HL anomalies found in real case study's measurements a) positive strains (traction) b) negative strains (compression)

With regards to the evolution of HF SRAs, Figure 61 compares two graphs belonging to the same length interval of the fiber but different time intervals. Graph a) presents the raw strain measurements from the beginning of the project (initial measurements and excavation period), whereas graph b) presents the strain readings from the beginning to the 25th March (last day of the second to last monitoring period). As can be seen when comparing both graphs, HF SRAs can be detected early on given that most of the SRAs seen in graph a) represent most of the SRAs observed in graph b). Some appear in posterior times, however, they present some alterations in their early stages as well which could be considered as warnings.

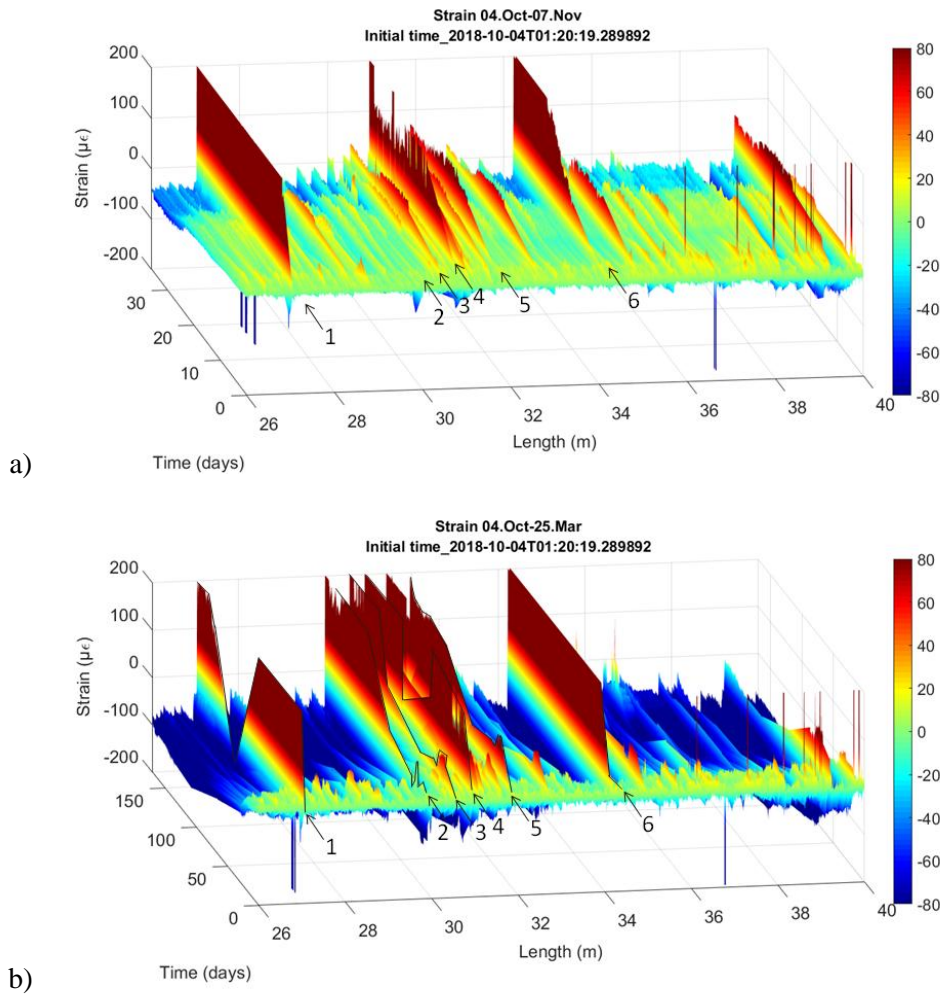


Figure 61. Evolution of SRAs a) 4thOctober - 7thNovember b) 4th October - 25th March

Note that Figure 60 and Figure 61 are representing the optical fiber length interval between 26 and 40 meters, which is considered as the least affected by strain peaks and catalogued discontinuities (as will be evaluated in depth in the results section). However, some SRAs can still be detected in this section which translates into SRAs being caused by local failures of the optical fiber measurement process.

Just for clear visualization of the amount of anomalies that the raw data set presents, Figure 62 is included in this section. In this graph, the 10 first meters of the fiber have not been included given that they are not bonded to the structure's surface and the anomalies that those present don't have to be structurally interpreted. As can be seen, there are several profiles that present anomalies specially in the 40-50m segment, which belongs to the fiber bonded to the slab and

under the rails and is by far the most affected by bonding discontinuities and, for it not being prefabricated, irregular concrete surface.

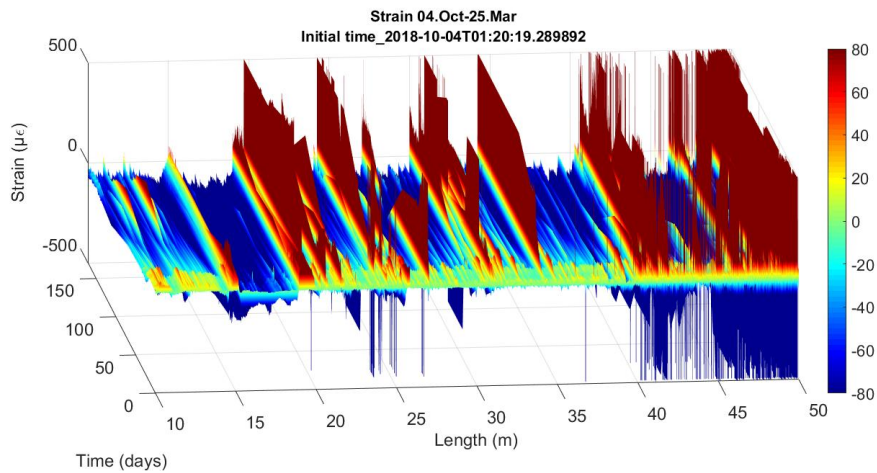


Figure 62. Graphical representation of strain raw readings between 4th October and 25th March

Obviously, in order to identify these anomalies in the collected data, the trend of every sensing section has to be studied. Since this tedious analysis is not actually viable in many projects given the dimensions of the data sets due to wide extensions of monitoring surfaces or long monitoring periods, an algorithm is developed with hopes of automatically detecting the characterized anomalies and allow for their removal. This algorithm will be tested with the case study's set of data with the aim of making this last presented graph SRAs-free and, consequently, ease its interpretation.

4.2.2. Anomalies post-processing

The idea behind the initially developed algorithm is based on the detection in the collected data of the SRAs defined above and the removal and substitution of such abnormal values by means of an interpolation procedure. The objective is to treat the raw strain measurements and obtain a new set of data that is more reliable than the first one and lacks the strain profiles distortion due to the presence of SRAs.

The reason behind exclusive detection and removal of SRAs is not enough is that new set of data would present empty data substituting the anomalous reading, whose respective times and locations are mostly random leading to discontinuous measurements in time and along the fiber. These missing values can however be approximated using the surrounding readings that are proved to be correct. Therefore, the steps that lead to a complete and improved, i.e. SRAs-free, set of data are:

1. *Detection of SRAs* → 2. *Removal of SRAs* → 3. *Substitution by interpolation*

4.2.2.1. Detection of anomalies

As mentioned in section 3.5 (Data collection) the SSQ values associated to the strain readings are used in the data post-processing as a tool to determine their quality and reliability [41]. By establishing a minimum SSQ value one can invalidate a percentage of SRAs and then, substitute the abnormal readings by linearly interpolated values between reliable readings achieving an undistorted strain profile (SRAs free).

The minimum/optimal SSQ value that deletes the highest percentage of SRAs while constituting a physically interpretable set of data depends on each monitoring campaign or optical fiber. Optimizing the SSQ value for interpolation is a trial and error process in which the only constraint on the SSQ value itself is that it has to be above 0.15 (recommended by the ODiSi software manufacturer [41]).

As can be seen in the following figure, different SSQ value restrictions have provided different outcomes. For the present section, the best fit (in red) can be achieved after the removal and consequent interpolation of the measurements with associated SSQ values lower than 0.30. A higher threshold would translate into to many measures being deleted (see cases SSQ lower than 0.35 or 0.45).

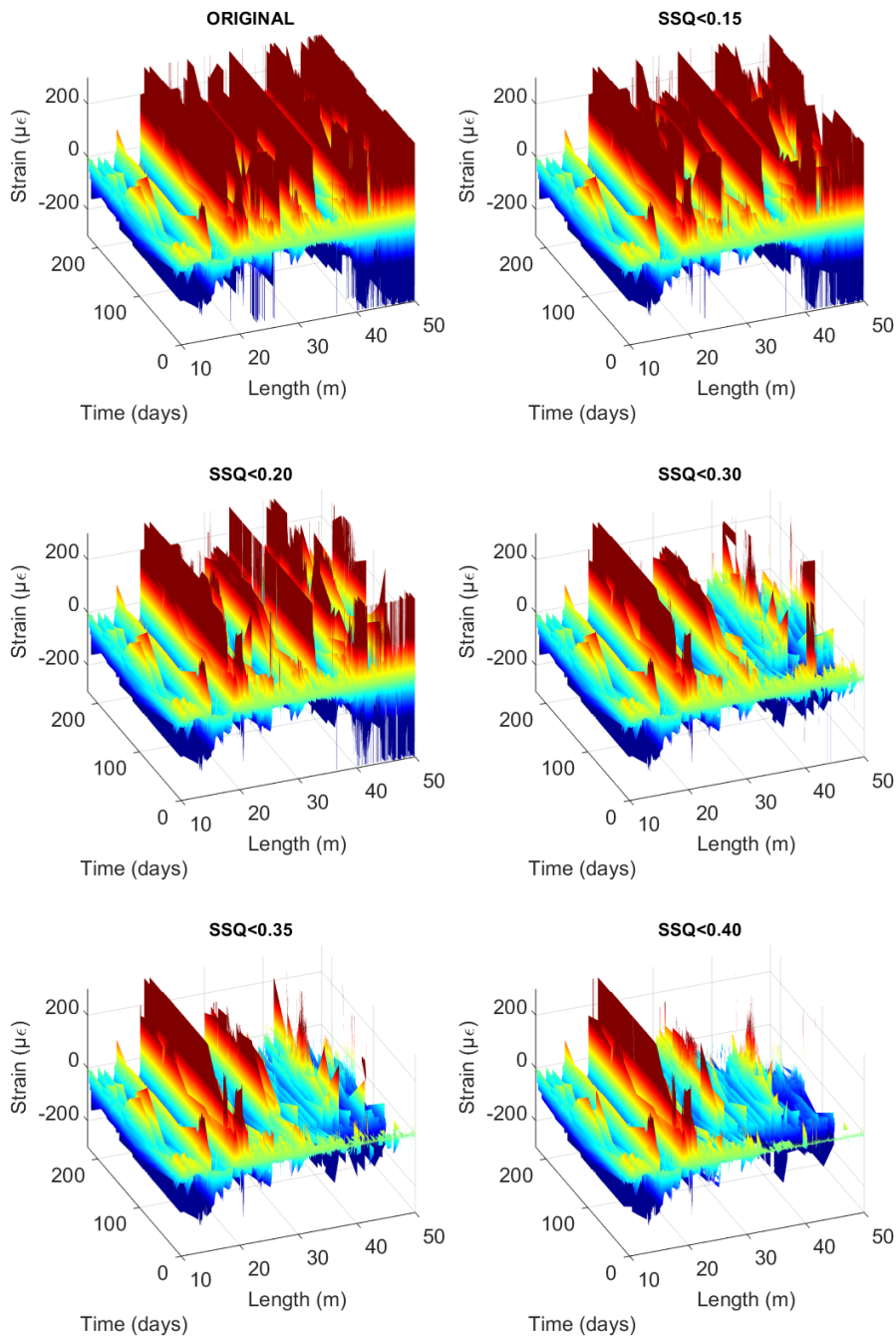


Figure 63. Strain measurements of segment 10-50m between 4th October and 17th May for different SSQ thresholds

A part from the SSQ consideration, one can directly apply the definition of SRA into the anomalies identification process. These are sudden and excessively large strain readings, i.e. there is an excessive variation between two consecutive readings.

In this case study, this SRA identification process based on strain ‘jumps’ can be applied either temporally or spatially. Temporally, because the loads are applied gradually on the construction site and the soil beneath it has to consolidate before the loads are transmitted to the tunnel structure and detected by the DOFS. Therefore, sudden strain variations in time are neither expected nor reasonable. Spatially, because the expected deformation levels in the monitored tunnel section due to the building construction at ground level (approximately $\pm 150 \mu\text{strains}$) are not prone to sizable cracks generation. Given that the only plausible physical explanation for large strain reading variations between two co-existing sections is cracking or a bonding discontinuity, it can be concluded that a spatial jump present in this case study’s collected data can be considered as an anomaly.

The concept of jumps in time and in space is shown in Figure 64 as readings that noticeably exceed the measurements surrounding them in terms of time and space respectively. Notice that the model jumps in time reproduce the concept of HL and HF SRAs shown in Figure 59. However, the model jump in space usually only appears as a single large peak, abrupt change in the spatial tendency (like the one a HF anomaly defines in time) could only happen if a single fiber was used to monitor an structural element (like a beam or a slab under a determinate loading scenario) being bonded to the element linearly covering both upper and lower surfaces. Then, the strain profile would represent the compressive and tensile strains associated to each surface one after the other along the fiber and, since the surfaces would be experiencing significantly different actions, an abrupt change would be expected between them. However, since the case study’s fiber is bonded along the inner fiber of the tunnel’s ring no concerns arise in the matter of spatial jumps being the subject structure continuous and subject to stable compressive loads.

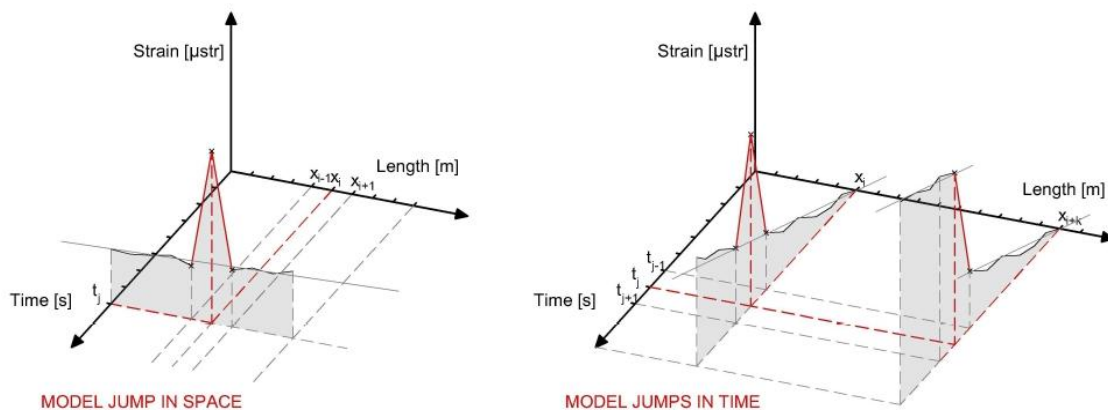


Figure 64. Jumps concept to detect anomalies

However, these considerations cannot be applied without a previous thoughtful review of the loading and structural conditions of the case study one is working on. As mentioned before, the objective is to delete unreliable readings, that is, measurements that do not reflect the real behaviour of the monitored structure. Establishing a maximum strain variation or minimum SSQ to identify an anomaly has to be done comparing the original and resulting sets of data (after the thresholds are applied and the interpolation is executed) and checking that the peaks elimination is coherent, neither excessive (which would imply a loss of reliable data) nor insufficient (which won’t allow for interpretation of readings).

For example, a laboratory experiment that involves the evaluation of a structure under impact loading or unloading processes would have to account for sudden and high strain variations between consecutive readings. The tendency of the raw data should be firstly identified and, next, the peaks elimination pattern defined. Maybe the consideration of large strain variations in consecutive readings removal wouldn't be accurate; however, the SSQ and/or the spatial strain jumps could be convenient instead. The same would happen if the response of a structural element was to be monitored up to crack formation under a gradually increasing load. Crack generation can cause significant strain variations between two co-existing sections; therefore, the spatial strain jumps removal would have a limited reliability.

The alternative for these particular cases would require, as always, being aware of the expected structural response of the monitored element to the loading case applied and studying the tendency of the raw set of data in order to identify the maximum reliable strain variation between consecutive readings and/or sections.

As a summary of this section, three different SRAs detecting procedures have been presented: SSQ, spatial and temporal JUMPS. Which one is more useful and how can they be combined or not to provide the desired result (SRAs-free strain profiles) depends on the structure, its loading and monitoring conditions and the study of the data.

4.2.2.2. Removal of SRAs

Once the SRAs have been detected it is easy to remove the abnormal values substituting them by *NaN*, which, in computing, stands for **Not a Number**. *NaN* is a numeric data type used by computing software (Matlab included) that represents an undefined or unrepresentable value. The equivalent parameter in Excel is *#N/A*, which stands for **Not Available**. It might be useful to take into account this notation variation when working with both programmes simultaneously.

In this case study, given that we are treating two 3290x5023 matrices (strain and SSQ) it is unviable to work with excel. Only preliminary data tests have been developed using excel and smaller sets of data like the monitoring periods separately.

This substitution of SRAs by *NaN* step is rather optional since the SRAs removal tool could be integrated in the interpolating algorithm. However, this phase is useful, on the one hand, to reduce the computational cost of the interpolation algorithm. Having the SRAs substituted by *NaNs* allows the algorithm to work only with one matrix. If it were to check the SSQ matrix or the jumps between consecutive measures for every strain measure (remember, 3290x5023) in order to determine if the strain measure is an SRA or not, it would be much harder to control and combine the different tools available for SRAs detection and interpolation.

On the other hand, *NaNs* helped in the preliminary evaluations of the data sets, thanks to the fact that both data treatment software, Matlab and Excel, allow for extraction of graphically interpolated strain profiles, meaning that the software does not need to be supplied with a strain value for every reading or location, in order to graphically represent the strain profile. Note that graphical interpolation is understood as providing a trend-line between two non-SRA strain readings covering the missing data but without computing their corresponding numerical value. Therefore, it allows for checking, before performing a computationally costly interpolation, if the SRAs removal procedure is efficient or not.

The problem regarding this graphical interpolation is that it develops incompatibilities, meaning that the missing reading will be substituted by a different value depending on the interpolation direction (if it is done through time or space). In the same way that one particular location cannot have two different strain measurements, a matrix cannot hold two values in one cell. That is why, in the next section, a part from developing an algorithm that approximates the strain values corresponding to SRAs, a priority and some conditions will have to be established between the two interpolation directions in order to produce the best set.

Therefore, the removal of SRAs algorithm follows the following simple Diagram 1.

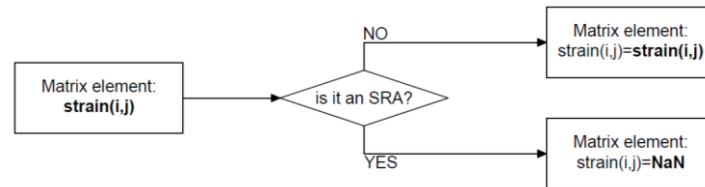


Diagram 1. Idea on substitution of SRAs

The complex part comes in identifying if the strain reading is an SRA or not. Two algorithms have been developed in order to cover the three SRAs detecting procedures defined in the previous section. Only two algorithms instead of three given that the spatial and temporal jumps can use the same algorithm with just a small variation, therefore, an algorithm for the SSQ tool and another for the JUMPS tool will be presented. An additional routine has been developed and named ERROR, it will be explained below as well.

SSQ routine

Substituting SRAs by *NaN* with the SSQ tool is achieved with the algorithm represented in Diagram 2a. It basically goes through the whole strain matrix column by column and, with an ‘*if*’ loop, checks, for each matrix element, if its associated SSQ value is lower than the *SSQ_{min}* (SSQ threshold established), if so, it substitutes the matrix element with ‘*NaN*’ and if not, it moves forward to the following matrix element.

JUMPS routine

Substituting SRAs by *NaN* with the JUMPS tool is achieved with the algorithm represented in Diagram 2b, which is a bit more elaborated. The idea is to go through the strain matrix column by column, if the temporal jumps are to be detected, or row by row, for the spatial jumps. The presented diagram works through the matrix to find temporal jumps, i.e. column by column, but it can easily be extrapolated to detect the spatial jumps by simply interchanging all *j* and *i*.

Since the JUMPS tool is usually applied after the SSQ, the routine already includes the possibility of finding *NaN* values, i.e. previously detected anomalies, in the strain matrix, which, if not considered would unable the algorithm. Note as well, that this algorithm starts at $j=2$, it does so that it can compare the strain matrix element to the previous one, since it is looking for the difference between the two values to be over a particular jump threshold Δ_{max} .

So, like with the previously presented algorithm, this one goes column by column. Before the start of each column an auxiliary counter *k* is set to 1, then, only if the strain matrix element in study is a *NaN* (from previous SSQ routine) the counter *k* increases 1 unit. Later an ‘*if*’ loop checks the strain variation between 2 readings: the current matrix element in study and the

closest previous element that is not a *NaN*. If the jump threshold Δ_{max} is surpassed, the current element is transformed to *NaN*, i.e. it is considered as an SRA, if not, there is one more ‘*if*’ check that will enable the check of the following element. Only if the current element in study is not *NaN* the counter increases to j , i.e. the current row number, if not the case, it remains the value it was.

Even though this second algorithm’s explanation is a bit tedious, it is interesting to notice that both HL and HF SRAs can be removed with it. When one measure in study exceeds the previous one by more than Δ_{max} it becomes a *NaN*, then, the next measure is compared to the first previous measure that is not a *NaN*. In the case that the measure in study is a HL anomaly, i.e. punctual failure, the next measure’s strain value will be similar to the one before the HL SRA, therefore, the Δ_{max} limit variation won’t be exceeded and the next measure will keep its strain value. On the other hand, if the measure in study is a HF SRA, the following measures will be deleted as well because, in HF SRAs, the strain profile is altered from their first appearance for the rest of the measurements which means that the following measurements will theoretically keep exceeding the correct strain value before the start of the HL anomaly by more than Δ_{max} μ strains and, therefore, keep becoming *NaN*.

The only drawback of the last routine was explained in the previous section, that is, it requires an in depth analysis of the data to determine a proper threshold Δ_{max} that 1. does not delete real peak measures as cracks or sudden loading events would be and 2. smoothens the strain profile deleting most SRAs.

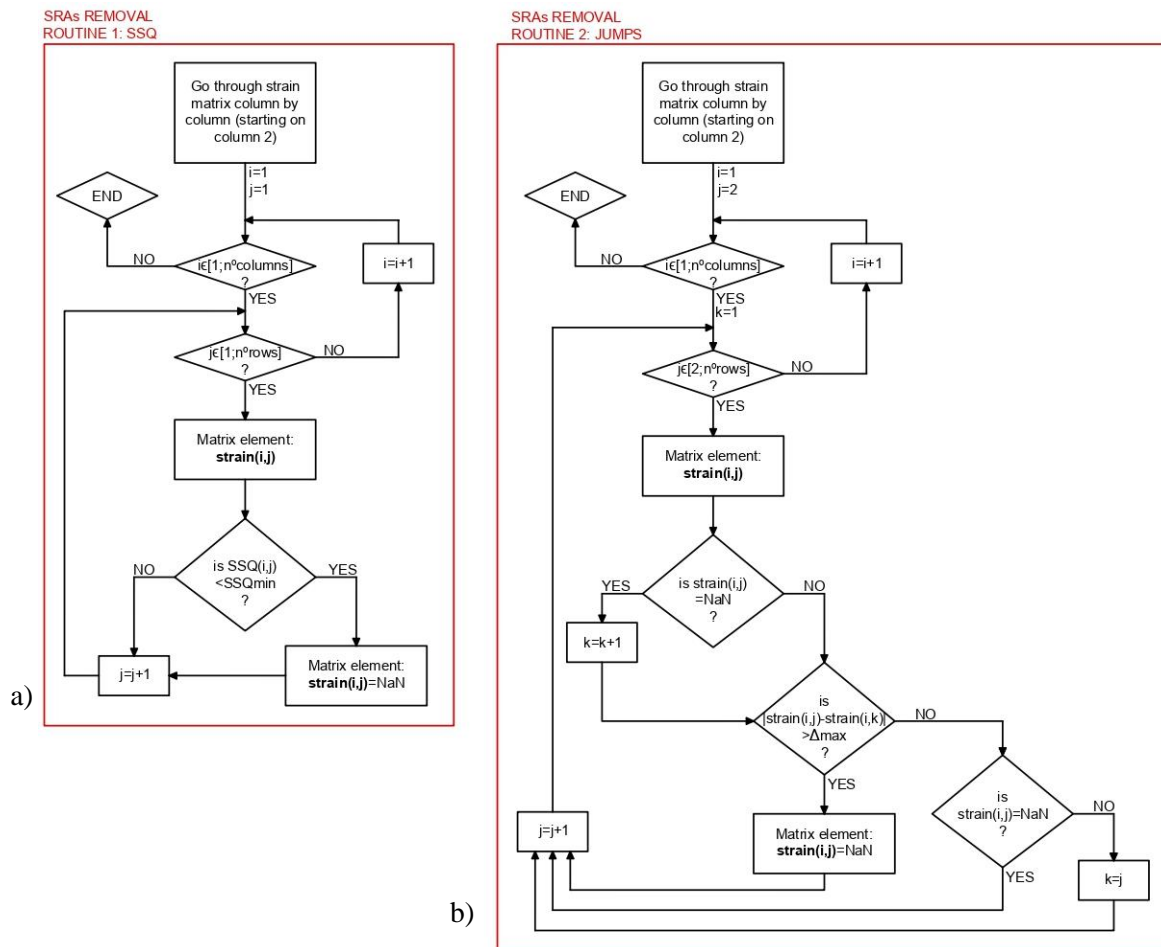


Diagram 2. SRAs removal with (a) SSQ detection tool and with (b) JUMPS tool

ERROR routine

The last developed routine regarding anomalies detection is based on the very simple concept that are errors. The first step is to develop a trend line of the readings of one location in time by means of a polynomial fitting curve, whose degree can be varied to provide more or less fitting. The degree of the polynomial fit cannot be too low, which would lead to non-representative tendencies, nor too high, because it would reproduce the punctual anomalies. After choosing the appropriate degree, a function that checks the difference between the reading and its corresponding expected value (belonging to the trend line) is developed. If the absolute value of this computed difference is higher than a determinate threshold, the reading is considered as an anomaly. The choice of the threshold value has to be, as always, a result of an in-depth study of the measured tendencies and peaks.

Figure 65 provides an example of the described procedure, in this case the only observed anomalies are found at the beginning of time (around 7th October) conforming what was described as a HL-SRA.

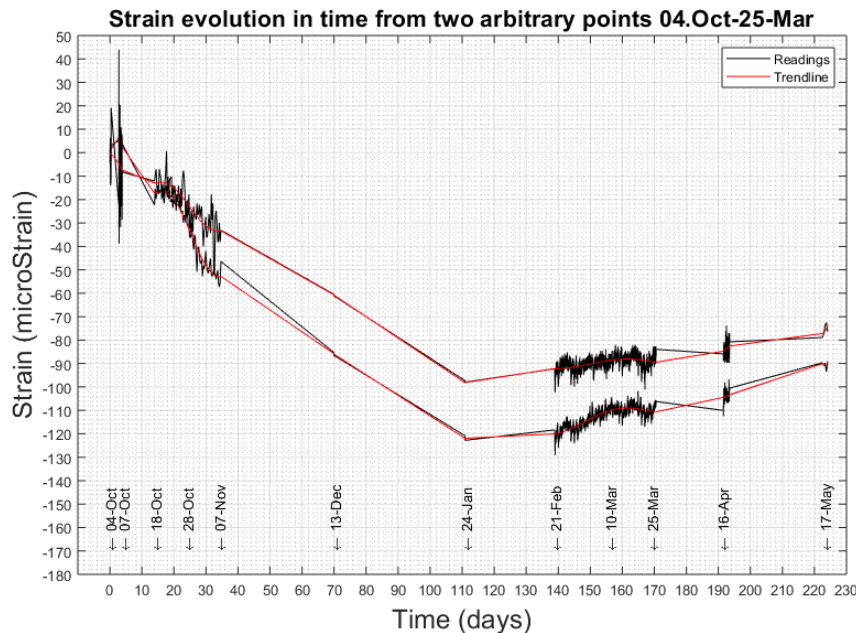


Figure 65. Example of trend lines

It is worth noticing as well that not having continuous monitoring precludes the trend lines from being smooth since the polynomial fit is ill-conditioned, i.e. it has too many data in some areas and few in others.

Additionally, it is worth mentioning that only harmless anomalies will be deleted if the fitting curve is done for one location at all times and since harmful anomalies usually present an excessively large but continuous profile, therefore, the fitting will reproduce the anomaly and, consequently, the routine will not delete it. This can be solved, as will be seen in the following section, through horizontal interpolation. However, it could be solved through this routine if the loading profile was known. In the case of knowing the exact loading scenario that the element is subject to at every time, an approximation of the expected strains could substitute the previously defined trend line, consequently, allowing to identify both harmless and harmful anomalies given that they would both differ significantly from the expected readings.

In the case study presented in this thesis, the construction time line is known but, unlike with typical laboratory tests, the exact loading scenario that the element is subject to at every time is not known. Therefore, the strain profiles cannot be compared to a base loading trend-line that they should theoretically follow and, consequently, HF-SRAs cannot be deleted with timely interpolation exclusively, they require spatial interpolation as well (see following section).

4.2.2.3. Substitution by interpolation

Regarding the interpolation of the removed data there are two options available.

- **Time interpolation**

When the missing values are interpolated between the previous and following readings of the same location consequently providing a smooth strain evolution of one location in time.

- **Space interpolation**

When the missing values are interpolated between the surrounding correct readings of the same measurement time. Therefore, a smooth strain profile is provided along the 0-50m of fiber.

These interpolations can be used to replace the detected anomalous readings. The possible generation of cracks during monitoring periods makes time interpolation preferable since they are usually detected by observing strain peaks between very close locations. However, space interpolation is the only way to delete HF-SRAs which do not present peaks in the same location but a rather magnified strain profile.

In the strain matrix organization rows represent the strains along the fiber at particular times, and columns, the strain evolution in time of each monitored point. For that, the interpolation algorithm will go through each row (if its space interpolation) or each column (if its time interpolation) looking for the missing readings and interpolating the missing values between the correct surrounding readings. Firstly, the interpolation algorithm is presented and, then, the possible combinations discussed.

The following algorithm looks for NaN values (corresponding to anomalies) and substitutes them by linearly interpolated strains from the correct readings surrounding them. The complex part involved the identification of the surrounding correct strains given that anomalies can involve in the direction of interpolation one reading alone or many, i.e. the distribution of anomalies in the matrix is random. Therefore, when evaluating the matrix row by row or column by column and coming across one NaN a auxiliary variable k (see following algorithm) has to start counting how many anomalies follow it. When the following non-anomalous reading appears, counter k is used to find the initial correct reading (before the NaNs), which together with the last, enables de computation of the interpolated values between them.

%VERTICAL INTERPOLATION: Substitutes NaN by interpolated values and fixes harmless anomalies

```
strain_nan=strain';
for i=1:length(position)
    for j=2:length(time_h)
        k=1;
        if (isnan(strain_nan(i,j))) && (j+k<=length(time_h))
            while (j+k<length(time_h)) && (isnan(strain_nan(i,j+k)))
                k=k+1;
            end
```

```

for h=1:k
m=(strain_nan(i,j+k)-strain_nan(i,j-1))/(time_h(j+k)-time_h(j-1));
strain_interp(i,j-1+h)=strain_nan(i,j-1)+m*(time_h(j-1+h)-time_h(j-1));
end
end
end
end
end

```

The above algorithm corresponds to a time interpolation (evaluates the time evolution of one location), however, it can also be applied in space as well through small changes regarding the indexing i and j (see Annex 4 for complete set of algorithms).

The only issue that this algorithm can come through is when one of the extremes of the interpolation is missing, i.e. if anomalies are located in the first or last components of the evaluated row or column. These values are the only ones that will be left as NaN, and consequently lost, since they cannot be interpolated.

Given that three SRAs detection tools and two interpolation possibilities have been defined, there are several combinations available and, as the interpolations can be computed consecutively, even more. After several trial rounds it is concluded that the algorithm combinations that work better are the following:

Combination 1

The first proposal which exploits SRAs detection using SSQ followed by the application of time jumps routine whose outcome is treated with an initial vertical interpolation to recover the missing values and a posterior horizontal interpolation to recover the particular values missed by the time interpolation. An example of the outcome of this combination is shown in the following figures.

The thresholds used to identify anomalies in Figure 66 and Figure 67 and were SSQs lower than 0.30 and strain jumps in time higher than $50 \mu\epsilon$. The initial figure provides both original and interpolated matrices to allow for comparison and the next one, the interpolated matrix only for better assessment of the peaks reduction and visual interpretation of the structural changes.

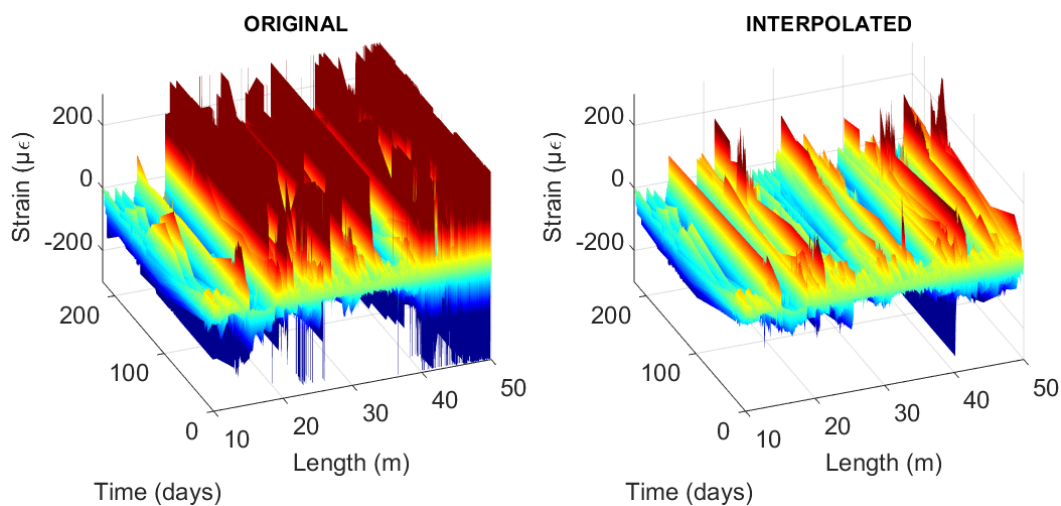


Figure 66. Original vs Interpolated matrix for combination 1 with $SSQ < 0.30$ and jumps in time $> 50 \mu\epsilon$ deleted

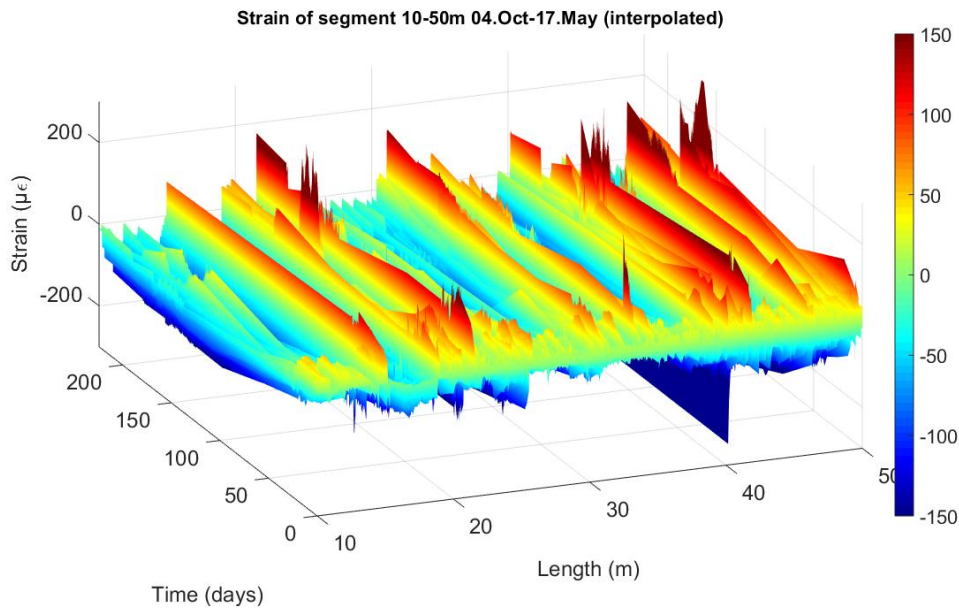


Figure 67. Combination 1 with $SSQ < 0.30$ and jumps in time $> 50\mu\epsilon$ deleted

This figure provides a good idea of the deformation processes that the monitored areas are experiencing. There are still some peaks which were not possibly deleted since they had an admissible SSQ value and, additionally, the time evolution corresponding to their location did not present jumps. However, the data is now visually interpretable, not at all like in the original matrix, which means a significant improvement.

Combination 2

This second option proposed to compute the anomalies detection through SSQ as well being followed by firstly by a direct time interpolation and then a horizontal interpolation of the outcome of a spatial jumps routine, in an attempt to smooth the surface in space. However, as can be seen in the following figures, this option doesn't present such a favourable outcome.

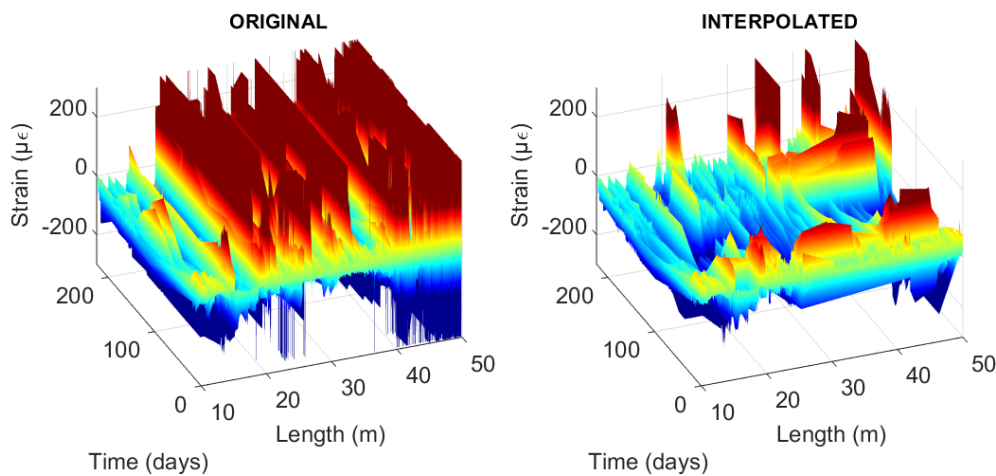


Figure 68. Original vs Interpolated matrix for combination 2 with $SSQ < 30$ and jumps in space $> 50\mu\epsilon$ deleted

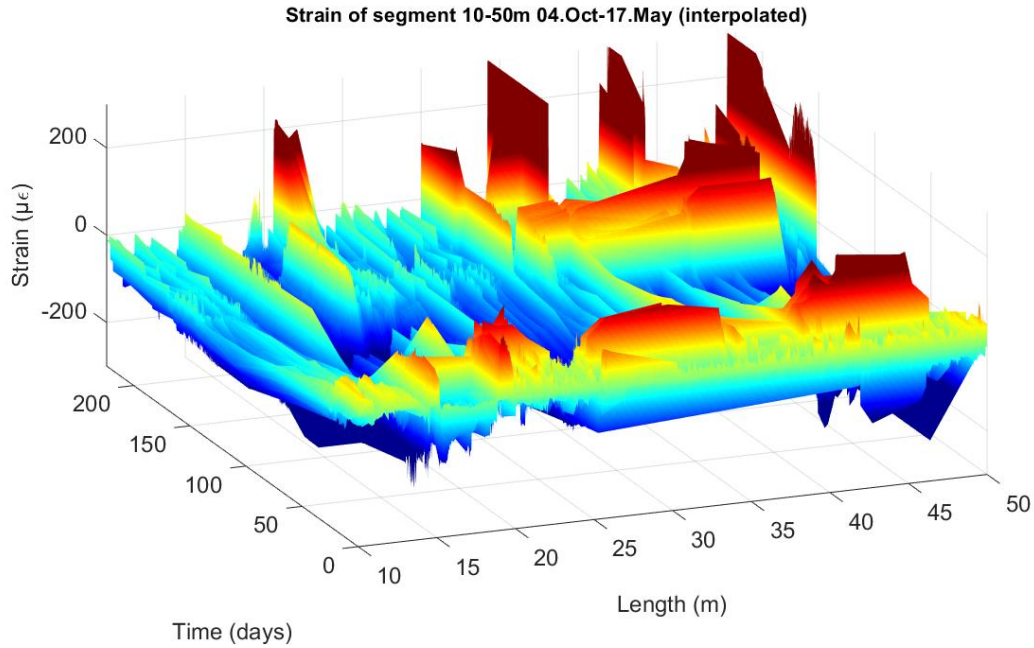


Figure 69. Combination 2 with $SSQ < 30$ and jumps in space $> 50 \mu\epsilon$ deleted

Even though some improvement has been achieved through this method, i.e. some anomalies have been deleted. Alterations can be clearly observed in the above figure that do not provide reliable data. Indeed some of the good readings have been deleted and substituted by a horizontal drag of strain peaks. This leads to the thought that the special interpolation will not provide a good outcome if the peaks have not been properly detected first.

Combination 3

Finally, the last combination addresses the error routine. The performed analysis seems to reveal that this routine doesn't work as desired in the studied case. The attempt to delete the harmless anomalies is in bane since the trend line has reached to them and considers them as good strain values (an example of that is circled below). However, the idea behind this algorithm that is comparison of the reading with the expected value has potential and could be perhaps improved by setting the polynomial fit with different conditions or assigning different weights to different readings depending on their reliability.

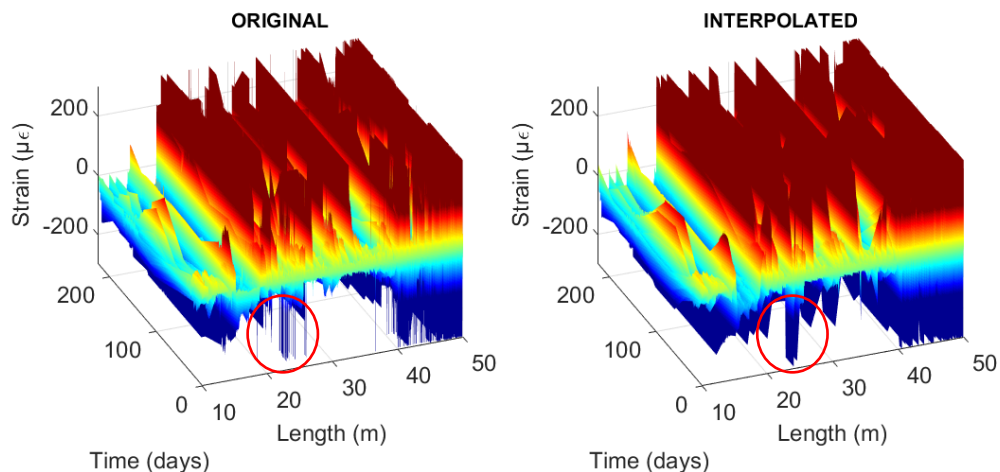


Figure 70. Combination 3 with polynomial fit of degree 5 and error $> 10 \mu\epsilon$

4.3. Final post-processing algorithm

The final proposal regarding data post processing for the particular case study is combination 1 given that it deletes the majority of anomalies while providing tendencies that make sense according to the structural conditions of the case. Additionally, it provides some visual interpretation of the behaviour of the structure as a whole. It can be seen in Figure 71a) that the inner surface of the concrete lining is experiencing generalized compression (in some places more than others). In Figure 71b) it can be interpreted that there are some differentiable fiber segments regarding the monitored response, the observed points that represent a change of tendency are marked with an arrow. The segments in between the arrows could perfectly coincide with the structurally differentiable elements that are covered with the same fiber. Indeed, the fiber covers the tunnel transversally (in the slab (4), the principal vault (3) and a small section at the beginning (1)) and longitudinally (2), monitoring segments might experience the unloading and loading processes at ground level differently.

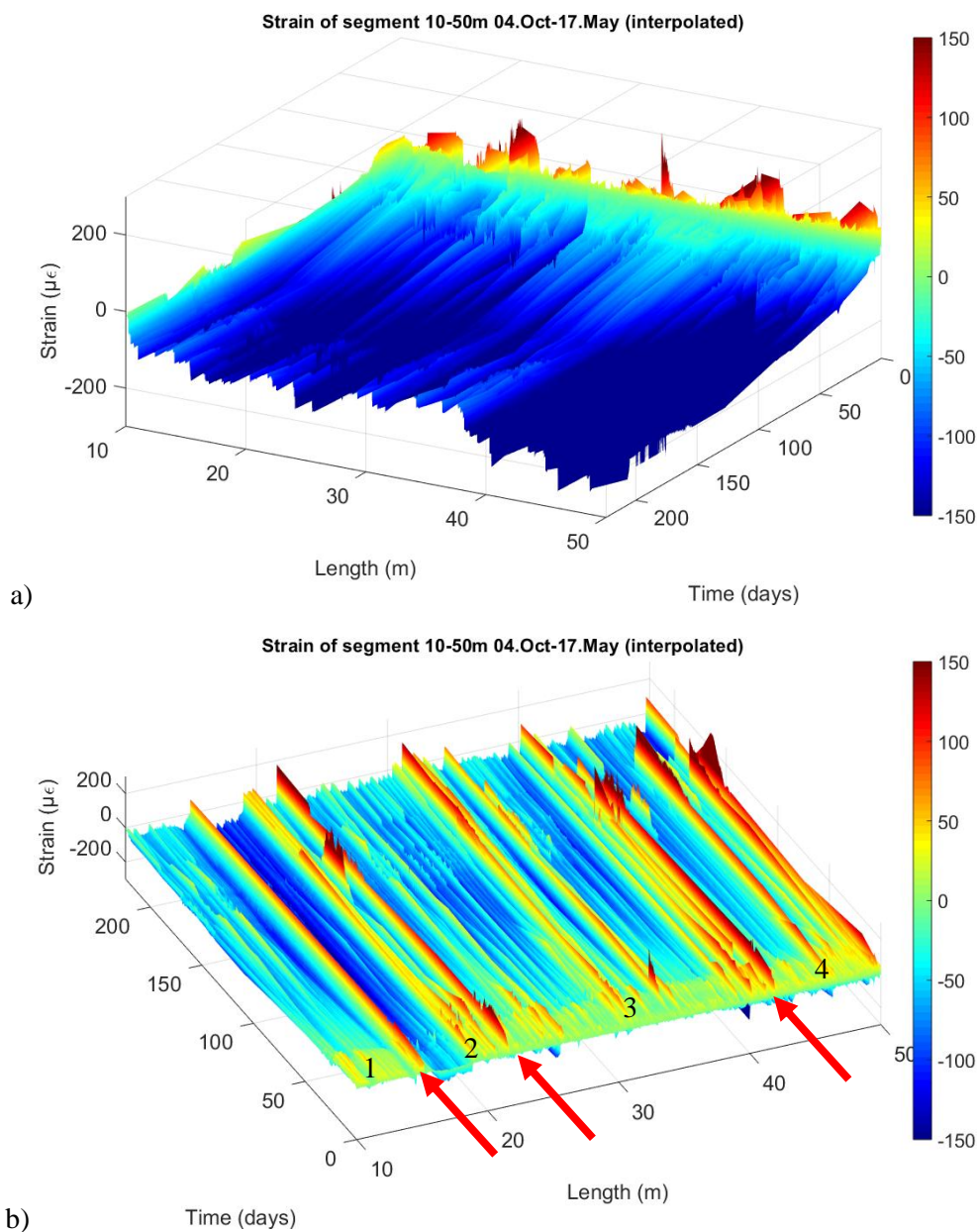


Figure 71. Final treated data set a) from below and b) from above

The final data set that has to be evaluated when trying to detect damage generation is the one presented above, because is the one found to work better regarding the treatment of anomalies among the proposed treatment strategies.

However, with the aim of properly observing the global behaviour of the structure an additional data treatment process is proposed. The idea came from the not very useful errors routine which used trend lines. A part from the already presented damage detection post-process, a global interpretation post-process can be developed through the use of polynomial fitting. Firstly, the readings of every location can be reproduced by a single curve erasing noise and anomalies and then, the graph can be smoothed in space by means of another fit. Of course, since the variability of readings at a particular time and along the whole fiber is much higher than the one of a particular location along the whole monitoring time, the degree of the polynomial fit will be higher in the first place, so can it can reproduce the differentiable behaviours of all fiber segments.

Applying this trend lines concept and after an assessment of the best polynomial fit regarding the trend lines the following figure is developed.

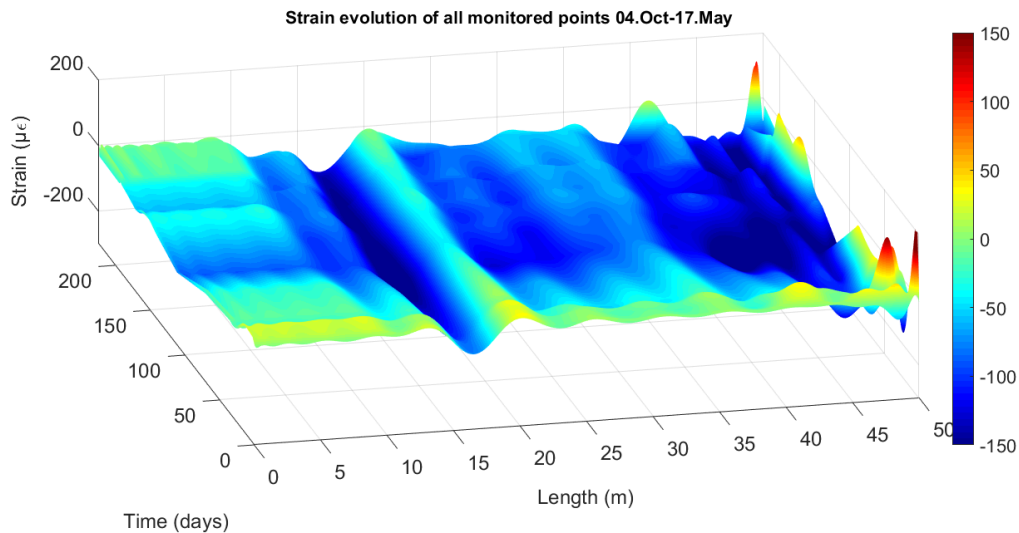


Figure 72. Treated strain data by means of trend lines

It is worth noticing that, up to now, segment 0-10m had not been shown given that it is not attached to the structural surface and, consequently, its readings don't provide structural strains. However, they have to be assessed as well because they could be reproducing temperature variations or other processes that might affect the rest of the readings as well. This will be assessed in the results section.

The later figures will be the ones assessed in the results section since the aim of the thesis is to see if the DOFS provide reliable data and reproduce what is really happening. Because of that, the data won't be tested regarding the highest accuracy but rather the orders of magnitude and if the measured strains are coherent with the structural and loading conditions of the case study.

However, it is important to stress that BOTH post-processed diagrams need to be evaluated after every monitoring period. The first one will provide an idea of local damage and the second one regarding global structural behaviour, and together they provide the required information to perform SHM for the case study.

5. Displacements computation from DOFS strain readings

Researchers such as Piccolo et al. [15] have developed methodologies for convergence computation from DOFS strain readings. As mentioned in the introduction, the study case of the mentioned paper proposes an alternative convergence measurement method to the commonly used invar wires or laser theodolites, whose performance is not considered to be optimal in cases with limited accessibility and operative area or aggressive environment (for example, road tunnels and waste repository cells). The main issues exposed in the article regarding the usual convergence monitoring sensors are their installation requirements, which take space, limiting the object structure operability, and preclude the application protective measures that could limit the sensor's exposure and avoid the performance reduction. The DOFS becomes a good alternative candidate when facing these kind of issues as seen in the introductory sections of this thesis. For that, [15] proposes and demonstrates the feasibility of the interpretation of the orthoradial strain measurements obtained by a DOFS to obtain the structural convergence using an inverse analysis associated with the finite element model.

The proposed methodology of [15] is applied to a laboratory test providing convergence measurements with a millimetre precision and, consequently, making way for new promising application of DOFS in tunnel monitoring.

An alternative approach for convergence computation is proposed in this section. The fundamental idea backing the new proposal is the definition of a body subject to stress. Applying loads to an arbitrary mass implies that it will undergo deformation, from which the point rotations and displacements of each point forming the body can be computed by means of the Navier-Bresse system of equations.

Regarding the case study of this thesis, the following sections present the theoretical basis of the crucial concepts strain, curvature, rotation and displacement and their application to the tunnel monitoring project is performed. The aim is to compute the displacements experienced by the fiber and, consequently, by the tunnel concrete lining. The results of the explained computations will be presented in the following section 6.

5.1. Theoretical background

5.1.2. Strain

Strain is a measure of deformation representing the displacement between particles in the body relative to a reference length and it can be expressed as the ratio between the total deformation and the original dimension of the body as represented in Equation 3.

$$\varepsilon = \frac{\Delta L}{L} = \frac{l - L}{L} \quad (3)$$

where ε is the engineering normal strain, L is the original length of the fiber and l is the final length of the fiber

The optical DOFS measures the lengthening and shortening episodes applied to it for being bonded to the concrete structure and, therefore, recreating its behaviour. As explained in the above sections, the readings obtained for each measuring point identify whether the fiber is

being expanded or compressed by comparing the measure taken at the time of the reading with the baseline measurement. Being the baseline supposedly free from perturbations, i.e. not undergoing loading processes, it represents the structure's initial state, to which all posterior measures are compared to with the aim of identifying length variations due to the loading / unloading processes that the structure undergoes.

Therefore, it is important to note that, in this case study, each value collected by the DOFS is not a strain value itself but the strain variation with respect to the initial state.

5.1.2. Curvature

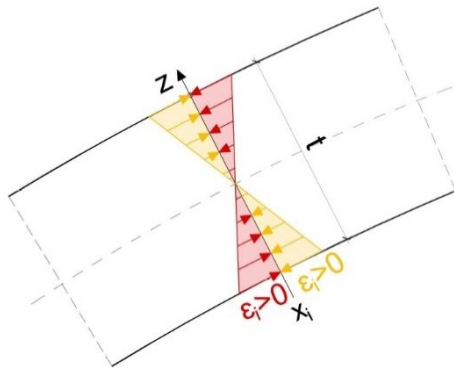
Considering a beam under Euler-Bernoulli's hypothesis, i.e. assuming that the sections that are orthogonal to the neutral surface remain flat and orthogonal after the deformation, that deflections in the all points of one section are small and equal to the ones in the beam axis and that lateral displacement is null, the strain in a segment of the beam varies linearly through thickness. This relationship is represented Equation 4.

$$\varepsilon_x = -\chi \cdot z \quad (4)$$

where χ is the curvature, ε the strain in the segment of the beam at a distance z from the neutral surface and x the axial coordinate.

On the basis of the corrected strain measurements, after an adequate post-processing, the curvature of the structure along its whole length with a resolution of 1cm can be obtained.

By simplifying the geometry of the concrete lining segments assuming that the loading processes of the structure induce a linear strain variation and that the neutral surface remains in the middle fiber with $z = -t/2$ (being t the thickness of the concrete lining) and maximum strains at upper and lower fiber. Then, the curvature can be computed for each measuring point by applying a particularization of Equation 4 that is Equation 5.



$$\chi_i = \frac{0 + \varepsilon_i}{t/2} = \frac{2 \cdot \varepsilon_i}{t} \quad (5)$$

where t is the concrete segment ring depth, ε_i the corresponding strain measure of location i and χ_i the associated curvature of location i .

Figure 73. Representation of location i deformation

As can be seen in Figure 73, if the measured strain value ε_i is negative, the lower fiber of section i is experiencing compression and, if positive, the lower fiber of section i is experiencing tension or, more accurately, decompression, since the concrete lining segments will still be compressed after the variation.

It is worth noticing that assuming that the neutral fiber remains in the section's gravity center is not very exact. Indeed, a monitoring scheme that would have provided an accurate measure of

curvature would have been the one covering two separated fibers of the same section. However, since the tunnel is already built it is not possible to access inner fibers or the upper one to deploy an additional line of sensors. This approximation, regarding both the magnitude of the neutral fiber height and the fact that it remains constant along the monitored tunnel section, might have a significant impact on the reliability of the computed displacements.

Curvature is a relevant value regarding structural analysis; however, it is not a value that offers much visual information. For that, the following sections present the theoretical definition of rotations and displacements.

5.1.3. Rotations and displacements

The Navier-Bresse cinematic equation system is used in the solid mechanics field with the aim of defining the behaviour of the particles forming a deformable solid. The system consists of two equations, one describing the movement of the particles and, the other, the rotation.

To compute the relative movement between two points G_0 and G_1 of a deformable solid the Navier-Bresse system can be used and is presented in Equations 6 and 7.

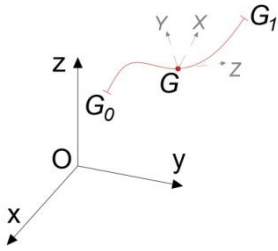


Figure 74. Relative movement between points A and B

$$\vec{\theta}_1 = \vec{\theta}_0 + \int_{G_0}^{G_1} d\vec{\theta} \quad (6)$$

$$\vec{u}_1 = \vec{u}_0 + \vec{\theta}_0 \wedge \vec{r}_{0-1} + \int_{G_0}^{G_1} d\vec{r} + \int_{G_0}^{G_1} d\vec{\theta} \wedge \vec{r} \quad (7)$$

where $\vec{\theta}$ denotes the rotation, \vec{u} is the displacement and r_{0-1} is the vector linking sections 0 and 1.

Expression 6 establishes that the rotation of an arbitrary point $\vec{\theta}_1$ depends firstly on the rotation of the entry point $\vec{\theta}_0$ representing the solid rigid rotation and the sum of the infinitesimal rotations happening between point 0 and point 1 that is $\int d\vec{\theta}$.

Expression 7 is a bit more complex. It establishes that the total displacement experienced by an arbitrary point \vec{u}_1 depends firstly on the solid rigid displacement characterized by the displacement of the entry point \vec{u}_0 and its corresponding rotation $\vec{\theta}_0$ that induces displacements in point 1 depending on the relative location between the two \vec{r}_{0-1} . The next component is the sum of the infinitesimal displacements occurring between points 0 and 1 that is $\int d\vec{u}$. Finally, the effect of the infinitesimal rotations happening between the two points is added to the final displacement computation with the component $\int d\vec{\theta} \wedge \vec{r}$.

Equations 6 and 7 can be particularized to the case study considering a 2-D slender curved beam of variable curvature made of an elastic material such that the relationship of stress and strain is linear holding even to a finite deformation [71].

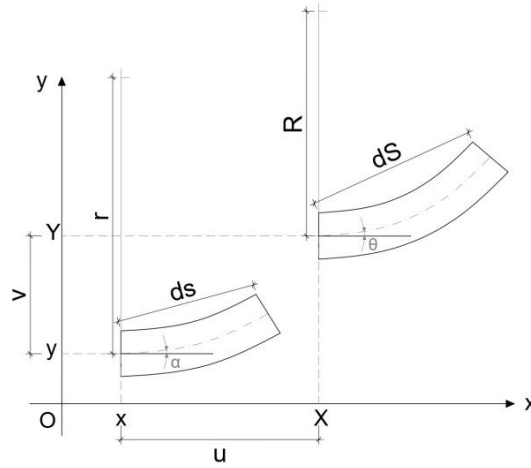


Figure 75. Deformations of infinitesimal element (adapted from [71])

The coordinates of point (x,y) in the un-deformed state deform to (X,Y) as seen in Figure 75 where v and u correspond to the vertical and horizontal displacements respectively. The tangent slope angle at (X,Y) is denoted by α and, at (x,y) , by θ with

$$\theta = \alpha + \varphi \quad (8)$$

where φ corresponds to the rotation angle.

For an arbitrary infinitesimal arc element in Figure 75 and denoting its corresponding radius of curvature as R , its deformed length dS satisfies

$$dS = R d\theta = \frac{1}{\chi} d\theta \Rightarrow d\theta = \chi dS \quad (9)$$

where χ corresponds to the curvature, i.e. inverse of the radius of curvature r , and $d\theta$ the infinitesimal variation of the tangent slope angle.

Additionally, considering that the applied loads remain in the xy -plane (see Figure 76) the following simplifications can be applied to equations 6 and 7.

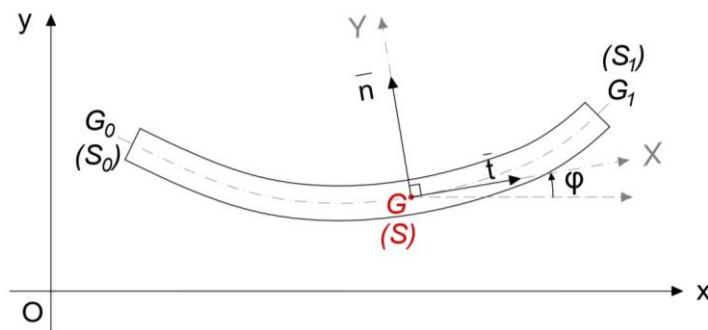


Figure 76. XY-plane element (adapted from [72])

$$\begin{aligned} Q_z = M_x = M_y = 0 \\ u_z = \theta_y = \theta_x = 0 \\ N_x = N; M_z = M; Q_y = Q; \theta_z = \theta \end{aligned} \quad (10)$$

where N , M and Q , represent the axial force, bending moment and shear force respectively.

Therefore, equation 6 is composed only by vectors perpendicular to the xy -plane and can be re-written in projection to Oz -axis as

$$\theta_1 = \theta_0 + \int_{G_0}^{G_1} \frac{M}{EI} ds \quad (11)$$

Regarding equation 7, it is equivalent to the two scalar equations bellow:

$$u_1 = u_0 + \theta_0(y_1 - y_0) + \int_{G_0}^{G_1} \left(\frac{N}{EA} dx - \frac{Q}{GA_C} dy \right) + \int_{G_0}^{G_1} \frac{M}{EI_z} (y_1 - y) ds \quad (12)$$

$$v_1 = v_0 + \theta_0(x_1 - x_0) + \int_{G_0}^{G_1} \left(\frac{N}{EA} dy + \frac{Q}{GA_C} dx \right) - \int_{G_0}^{G_1} \frac{M}{EI_z} (x_1 - x) ds \quad (13)$$

where, (x, y) are the coordinates of the arbitrary point G , (u, v) are the components of its displacement vector in the $\{O, x y z\}$ space, E is the Young modulus, A is the area of the section, G is the shear modulus and A_C the shear area.

The graphical representation of each component of the previous formulas is clearly represented by C. Navarro in [73].

According to [74], for an arbitrary beam, the contribution of the axial and shear forces (first integral) to the total displacement is negligible when compared to the bending moment contribution (second integral). In particular, the contribution of the shear force is only significant for short elements (small relationship length/depth). For this, the first integral is neglected in the following computations.

Since the moment laws are unknown, in the formulas 11 to 13, the concept of curvature will be used instead since, according to the Euler-Bernoulli theory,

$$M = EI_z \chi \Rightarrow \chi = \frac{M}{EI_z} \quad (14)$$

Finally, the Navier-Bresse system of equations particularized for the case study is presented in equations 15-17, allowing for the computation of rotations and translations suffered by an arbitrary plane section (S_1) due to variations of curvature, i.e. bending moment.

$$\theta_1 = \theta_0 + \int_{G_0}^{G_1} \chi ds \quad (15)$$

$$u_1 = u_0 - \theta_0(y_1 - y_0) - \int_{G_0}^{G_1} \chi (y_1 - y) ds \quad (16)$$

$$v_1 = v_0 + \theta_0(x_1 - x_0) + \int_{G_0}^{G_1} \chi (x_1 - x) ds \quad (17)$$

being (x, y) the coordinates of the arbitrary point G and (u, v) the components of its displacement vector in the $\{O, x y z\}$ space.

5.1.4. Cylindrical coordinates

The displacement computation is aimed at the ring structure, i.e. between fiber lengths 23m and 40m as marked by the continuous red line in Figure 77. Since the real segment of fiber almost defines half a circle with a 5.45m radius, its geometry will be approximated to that with the aim of easing the displacements computation.

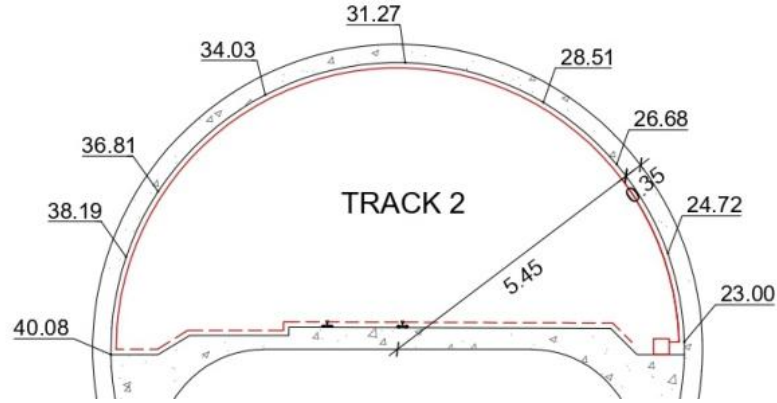


Figure 77. Segment of fiber employed to compute displacements

In addition, on the basis of the case study's geometry and the computed displacements interpretation, it is preferable to obtain the radial and tangential displacements that each measuring point is subject to rather than the Cartesian u and v displacements. For that, a change of the coordinate system is applied considering a plane structure with a middle line defined by a circular arc with centre in O and radius R (see Figure 78).

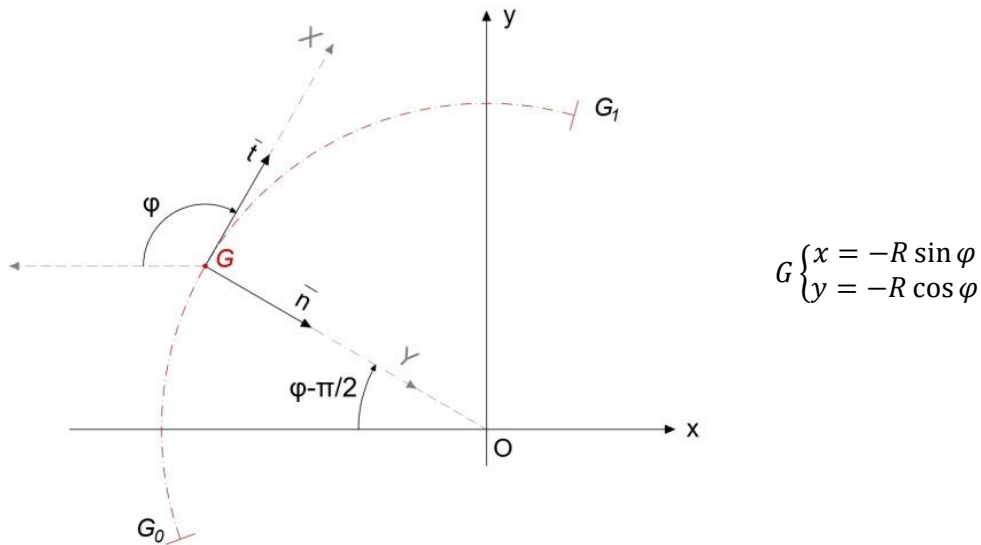


Figure 78. Change from Cartesian to cylindrical coordinates (adapted from [72])

Being u and v the components of the displacement vector $\overline{\delta G}$ in the xyz fixed reference axis and U and V the tangential and radial components of the displacement vector in the XYZ mobile axis, the change of basis matrix is

$$\begin{pmatrix} U \\ V \end{pmatrix} = \begin{pmatrix} -\cos\varphi & \sin\varphi \\ \sin\varphi & \cos\varphi \end{pmatrix} \begin{pmatrix} u \\ v \end{pmatrix} \quad (18)$$

The displacements at location i can be therefore computed in two ways, going back to location 0 for each computation or using the displacements and curvatures computed for the previous location $i - 1$. The computation presentation will be done for the first option from which the later can be easily extrapolated. Then, considering that the aim is to obtain the displacements at each location i , it follows

$$U_i = -u_0 \cos \varphi_i + v_0 \sin \varphi_i + R\theta_0[\cos(\varphi_i - \varphi_0) - 1] + R^2 \int_{\varphi_0}^{\varphi_i} \chi[\cos(\varphi_i - \varphi) - 1]d\varphi \quad (19)$$

$$V_i = u_0 \sin \varphi_i + v_0 \cos \varphi_i + R\theta_0[\sin(\varphi_i - \varphi_0)] + R^2 \int_{\varphi_0}^{\varphi_i} \chi[\sin(\varphi_i - \varphi)]d\varphi \quad (20)$$

The angles φ_i and φ_0 are detailed in Figure 79.

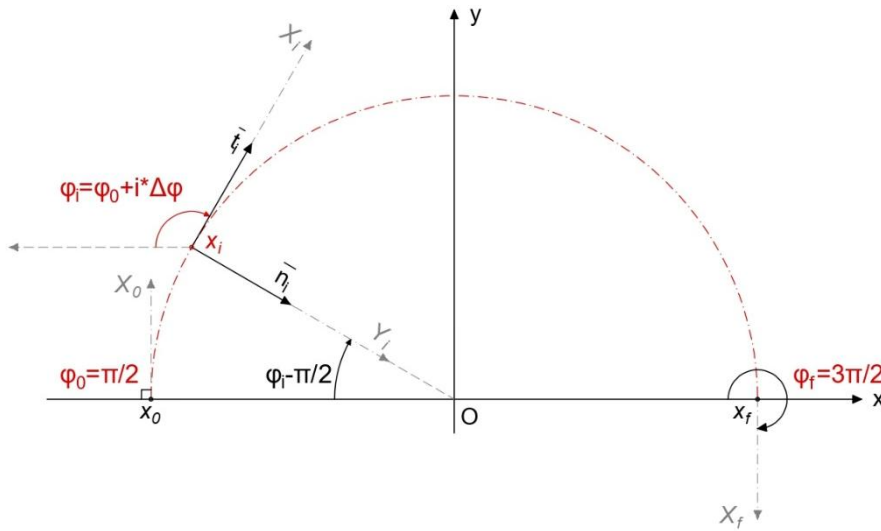


Figure 79. Definition of arbitrary angle φ_i and initial φ_0

In order to be able to compute the displacements U_i and V_i at each strain measuring location i , the fiber point located further from the loading area (at fiber length 40m) is chosen as the starting point for each of the displacements computations. The final point of the segment to evaluate is found at fiber length 23m, covering the whole length of the tunnel vault. The initial point could be assumed to have null induced displacements for being the least affected by the loading processes. This condition regarding the initial point could be applied directly to the system of equations defined by formulas 19 and 20. However, applying only this condition would lead to increasing displacements (in magnitude) along the fiber reaching a maximum for the last evaluated point $x=23\text{m}$, which wouldn't make sense, since the location that experiences larger displacements should be the closest one to the load application point, i.e. somewhere between locations 31m and 28m.

Other conditions that could be applied to the system to solve the mentioned problem would be assuming that the last point (supposedly symmetric to the initial one) has null radial displacement, due to the presence of the tunnel slab acting as a diaphragm, or that the last point has an equal tangential displacement in magnitude as the first one but with the opposite sign.

However, these boundary conditions are rather unclear considering that the last point is not exactly at the same height as the first one (it is actually 30cm above the slab) and that the load redistribution pattern and magnitudes are not exactly known. For this reason, different computing cases will be developed in order to assess the better conditioning application. After a study regarding the behaviour of the displacement function depending on the initial and final variables, the proposed options for conditioning are:

$$U_0 = 0; V_0 = 0 \text{ and } \theta_0 \text{ s. t. } V_f \approx 0 \quad (21.A)$$

$$U_0 \text{ and } \theta_0 \text{ s. t. } U_f \approx -U_0 \text{ and } V_f = V_0 = 0 \quad (21.B)$$

$$\text{Inverse problem: } U_f, V_f \text{ s. t. } U_0 = V_0 = 0 \text{ or } U_f, V_f \text{ s. t. } U_0 = 0 \quad (21.C)$$

where x would be an arbitrary value up to testing.

This initial rotation θ_0 , conditioned by the displacement at the final point, can be obtained through an optimization function applied to the radial displacement at the final point for each temporal reading. It works for both cases A and B, the only difference is that the optimized function will be V_f in case A and $U_f + U_0$ in case B.

The inverse problem proposition is originated after several erroneous tests regarding the attempt to impose low radial displacements at the extremes. It consists in computing the displacements from fiber length 23m towards 40m and performing an optimization that minimizes the displacements at $x=40m$ depending on the considered values for rotation and displacements at $x=23m$. Note that, for this, a change of coordinates has to be done in the developed formulas since the tangential displacement has opposite direction, for which the developed theory in [72] was used.

It is worth noticing, regarding the conditions, that the radial displacement at the final point (23m), could eventually be computed given that the deformations along the upper fiber of the tunnel slab are known. Therefore, a procedure similar to the one used for the tunnel vault but extrapolated to the concrete slab could be applied for the fiber segment 40-50m obtaining the displacement of the last point of the fiber, 50m, and posteriorly applying it substituting the established condition of $v_f = 0$. Even though, this would provide a more reliable convergence measure, it is not executed for the case study due to various reasons:

- Point 50m does not coincide with point 23m as can be seen in the fiber layout and pictures (Annex 1 and Annex 2). Point 50m is found on the slab at approximately 1m from the concrete lining and point 23m is located on the concrete lining's inner surface 30cm above the corner formed by the slab and tunnel vault.
- As was seen in the data treatment section, the raw strain readings between fiber lengths 40-50m present a high rate of anomalies, which, even after the data treatment, cannot be removed completely. Therefore, the convergence computation of the slab would be affected by too much error.

- Given the structural and loading conditions of the case study, the expected radial displacement at location 23m is very small, therefore, easily approximated to 0.

5.1.5. Approximation by Riemann

Given that the curvature is available as a discrete function, an approximation of the integrals to be solved in the described series of computations will be presented in this section.

The approximation method used is the Riemann sum which states that, for a function f defined on $[a, b]$, a partition P of $[a, b]$ into a collection of subintervals $[x_0, x_1], [x_1, x_2], \dots, [x_{n-1}, x_n]$, and for each $i = 1, 2, \dots, n$, a point x_i^* in $[x_{i-1}, x_i]$, the sum

$$S = \sum_{i=0}^n f(x_i^*)(x_i - x_{i-1}) = \sum_{i=0}^n f(x_i^*)\Delta x_i \quad (22)$$

can approximate a definite integral of f from a to b as

$$\int_a^b f(x)dx = \lim_{n \rightarrow \infty} \sum_{i=0}^n f(x_i^*)\Delta x_i \quad (23)$$

Therefore, equation 15 can be approximated as:

$$\theta_i = \theta_0 + R \int_{\varphi_0}^{\varphi_i} \chi d\varphi = \theta_0 + R \sum_{k=0}^i \chi_k \Delta\varphi \quad (24)$$

And the integrals in equations 19 and 20 as:

$$\int_{\varphi_0}^{\varphi_i} \chi [\cos(\varphi_i - \varphi) - 1] d\varphi = \sum_{k=0}^{i-1} \chi_k [\cos(\varphi_i - \varphi_k) - 1] \Delta\varphi \quad (25)$$

$$\int_{\varphi_0}^{\varphi_i} \chi [\sin(\varphi_i - \varphi)] d\varphi = \sum_{k=0}^{i-1} \chi_k [\sin(\varphi_i - \varphi_k)] \Delta\varphi \quad (26)$$

where $\Delta\varphi$ is the angle variation between each performed reading and, since the distance between readings Δl is constant with 1cm, it is safe to say, being such a small angle variation that:

$$\Delta\varphi = \frac{\Delta l}{R} = \frac{0.01}{5.45} \approx 1.83 \cdot 10^{-3} \quad (27)$$

5.1.6. Final system of equations

As mentioned before, there are two possibilities regarding the computation of displacements from $x=40\text{m}$ towards $x=23\text{m}$. The displacements at location i can be computed going back to location 0 for each computation (option I) or using the displacements and curvatures computed for the previous location $i - 1$ (option II).

I: The final system of equations to compute and add to the algorithm is, after the change of coordinates and the integral approximation,

$$U_i = -u_0 \cos \varphi_i + v_0 \sin \varphi_i + R\theta_0[\cos(\varphi_i - \varphi_0) - 1] + R^2\Delta\varphi \sum_{k=0}^{i-1} \chi_k[\cos(\varphi_i - \varphi_k) - 1] \quad (\text{I.28})$$

$$V_i = u_0 \sin \varphi_i + v_0 \cos \varphi_i + R\theta_0[\sin(\varphi_i - \varphi_0)] + R^2\Delta\varphi \sum_{k=0}^{i-1} \chi_k[\sin(\varphi_i - \varphi_k)] \quad (\text{I.29})$$

with R , the inner radius of the tunnel and $\Delta\varphi$, the variation of the φ angle between two readings.

II: If the computation of displacements in each location i is wished to be done from the previous location $i - 1$, the system of equations becomes, after the explained approximations,

$$U_i = -u_{i-1} \cos \varphi_i + v_{i-1} \sin \varphi_i + R\theta_{i-1}[\cos(\Delta\varphi) - 1] + R^2 \frac{\Delta\varphi}{2} [\chi_{i-1}[\cos(\Delta\varphi) - 1]] \quad (\text{II.30})$$

$$V_i = u_{i-1} \sin \varphi_i + v_{i-1} \cos \varphi_i + R\theta_{i-1}[\sin(\Delta\varphi)] + R^2 \frac{\Delta\varphi}{2} [\chi_{i-1} \sin(\Delta\varphi)] \quad (\text{II.31})$$

with the change of coordinates of the displacements at each step as,

$$\begin{pmatrix} u_i \\ v_i \end{pmatrix} = \begin{pmatrix} -\cos\varphi_i & \sin\varphi_i \\ \sin\varphi_i & \cos\varphi_i \end{pmatrix} \begin{pmatrix} U_i \\ V_i \end{pmatrix} \quad (\text{II.32})$$

and the computation of the rotation at each step as,

$$\theta_i = \theta_{i-1} + R[\chi_i + \chi_{i-1}] \frac{\Delta\varphi}{2} \quad (\text{II.33})$$

with R , the inner radius of the tunnel and $\Delta\varphi$, the variation of the φ angle between two readings.

In principle, both methods lead to the same results.

Finally, the inverse problem system of equations is also presented, since it will be used for conditioning case C. After some development, it is obtained for the displacements computation referenced at the initial point (I) as,

$$U_i = u_0 \cos \varphi_i + v_0 \sin \varphi_i + R\theta_0[1 - \cos(\varphi_i - \varphi_0)] \\ + R^2 \Delta\varphi \sum_{k=0}^{i-1} \chi_k [1 - \cos(\varphi_i - \varphi_k)] \quad (\text{I.34})$$

$$V_i = -u_0 \sin \varphi_i + v_0 \cos \varphi_i + R\theta_0[\sin(\varphi_i - \varphi_0)] \\ + R^2 \Delta\varphi \sum_{k=0}^{i-1} \chi_k [\sin(\varphi_i - \varphi_k)] \quad (\text{I.35})$$

with R , the inner radius of the tunnel and $\Delta\varphi$, the variation of the φ angle between two readings.

And for the displacements computation referenced at the previous point (II) as,

$$U_i = u_{i-1} \cos \varphi_i + v_{i-1} \sin \varphi_i + R\theta_{i-1}[1 - \cos(\Delta\varphi)] \\ + R^2 \frac{\Delta\varphi}{2} [\chi_{i-1} [1 - \cos(\Delta\varphi)]] \quad (\text{II.36})$$

$$V_i = -u_{i-1} \sin \varphi_i + v_{i-1} \cos \varphi_i + R\theta_{i-1}[\sin(\Delta\varphi)] \\ + R^2 \frac{\Delta\varphi}{2} [\chi_{i-1} \sin(\Delta\varphi)] \quad (\text{II.37})$$

with the change of coordinates of the displacements at each step as,

$$\begin{pmatrix} u_i \\ v_i \end{pmatrix} = \begin{pmatrix} \cos \varphi_i & -\sin \varphi_i \\ \sin \varphi_i & \cos \varphi_i \end{pmatrix} \begin{pmatrix} U_i \\ V_i \end{pmatrix} \quad (\text{II.38})$$

and the computation of the rotation at each step as,

$$\theta_i = \theta_{i-1} + R[\chi_i + \chi_{i-1}] \frac{\Delta\varphi}{2} \quad (\text{II.39})$$

with R , the inner radius of the tunnel and $\Delta\varphi$, the variation of the φ angle between two readings.

5.2. Algorithm for displacement computation

The developed algorithm can be found in Annex 4; however, a small introduction to it is presented here. With the aim of obtaining the displacements, the theoretical concepts presented in the previous section are introduced to the algorithm. Firstly, the concrete lining thickness ‘t’ is added to enable the curvature computation and the tunnel radius ‘R’ to compute the displacements.

```
% Parameters
t=0.35/2;           %half of the concrete lining segment's thickness in [m]
R=5.45;            %approximate tunnel radius in [m]
```

As mentioned before, the computation of displacements starts from fiber length 40m, the furthest section point from the loading area and assumed as not affected, up to fiber length 23m, i.e. the other corner. Therefore, an integration interval is defined regarding the fiber segment along which the displacements wish to be computed. Since the strain matrix is organized by columns with locations from 0m to 50m (see Figure 52) it is flipped to satisfy the integration direction (from left to right) and reduced to cover only the wished interval given that the rest of data (0-23m and 40-50m intervals) is not needed. The position vector is also reduced and flipped in the same manner to ease posterior computations.

```
% Integration interval
i1=23;
i2=40;
pos1=find(position <= i1,1,'last');
pos2=find(position >= i2,1,'first');
position=flip(position(pos1:pos2),1);
strain=flip(strain(:,pos1:pos2),2);
```

The curvatures are easy to compute directly applying Equation 5, i.e. dividing all components of the strain matrix by half of the thickness of the concrete lining segments ‘t’. This computation multiplies all strains by 10^{-6} given that the strain is measured in $\mu\epsilon$.

```
% Curvatures [1/m]
curv=strain*(1E-06)/t;
```

The integration step $\Delta\varphi$ is introduced directly applying Equation 27 and the corresponding φ_i angles for each position i are computed and stored in a vector named ‘fi’.

```
% Fi step [rad]
Afi=0.01/R;
% Fi [rad]
fi=[];
for n=0:length(pos_disp)
    fi=[fi pi()/2+n*Afi];
end
```

Finally, the displacements are computed drawing upon the equations presented in section 5.1.6, which involve the use of the Riemann approximation, noted in the algorithm as ‘SRU’ for the tangential displacements and ‘SRV’ for the radial ones. This part of the code is not included here because of its length but it is presented in Annex 4, where both options shown in section 5.1.6 regarding the final system of equations are presented and were tested to provide equal results.

The boundary condition / hypothesis established for each reading in option A is that the first point of the integration interval has null displacements and a rotation such that the radial displacement in the final point is minimized (from Equation 21.A). For option B, we have that the radial displacement of the first point is null but the tangential one has an arbitrary trial value

x and a rotation such that the final tangential displacement is equal to x , thus to the initial tangential displacement (from Equation 21.B). These two possible conditions are easily applied to code I, by simply isolating the initial rotation variable since the displacements depend directly on it for every location, and to code II, by computing an optimization of the desired displacement (radial or tangential) varying the initial rotation value. The inverse problem proposed for conditioning 21.C works equally when optimizing a function, the only difference is that it follows a different system of equations.

The results and an assessment of the proposed technique are shown in the following section right after the presentation and interpretation of the treated strain measurements.

6. Results and discussion

This section is aimed at interpreting the treated data displaying the collected strain measures and comparing them to the tunnel's expected structural response. Firstly, a basic structural analysis on the effects of the building construction on the tunnel structure will be presented being followed later by the DOFS data display and its corresponding verification and assessment.

6.1. Expected structural effects

In order to provide an overview on the structural response of the tunnel's concrete lining a basic structural analysis is executed. It is assumed, as explained in Section 5.1.2., that the concrete lining segments are in complete axial compressive state given the nature of the infrastructure. Considering that as the initial state, all the observed compressive or tensile effects in the model represent the variations applied to the initial state, meaning that when the model presents tensile stresses it does not imply that the concrete lining segment is working in tension but rather that it is being slightly decompressed.

Given that the lower fiber of the tunnel concrete lining is being monitored, it can be expected that, as in a simply supported beam under a uniformly distributed load (Figure 80), when it is unloaded the lower fiber will experience compression and, when it is loaded, traction. For that, it can be deduced that the strain evolution in time will have a negative slope for as long as the soil surrounding the underground structure is transmitting the excavation effects to it. After that, the strain-readings should reach a maximum compressive state and start reproducing the effect of the construction works by adopting a positive slope representing decompression.

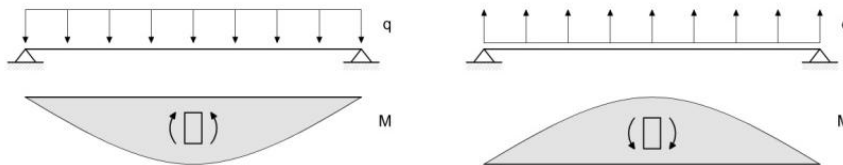


Figure 80. Simply supported beam under uniformly distributed load

For appropriate visualization of the different effects of the building construction along the tunnel's vault two simple theoretical 2-D models are developed with GiD Software [75] based on Finite Element Analysis (FEM). These models aim to recreate the effects of the unloading event, which takes place during the excavation period (from 8th October to 9th November), and the loading process, which corresponds to the construction works (from 13th December until, supposedly, the beginning of year 2020) on the tunnel structure.

In both theoretical models, the loads have been exaggerated in order to produce tensile differences in the concrete lining that are visually appreciable and interpretable and will later allow for interpretation of the behaviour of different points in the section.

6.1.1. Unloading model

The model overview of the excavation period is presented in Figure 81. A positive vertical load of approximately 85kN/m^2 (from assuming an excavation depth of 4.7m and a soil specific weight of 18kN/m^3) is applied on the right half of the simulated ground surface replicating the soil removal process.

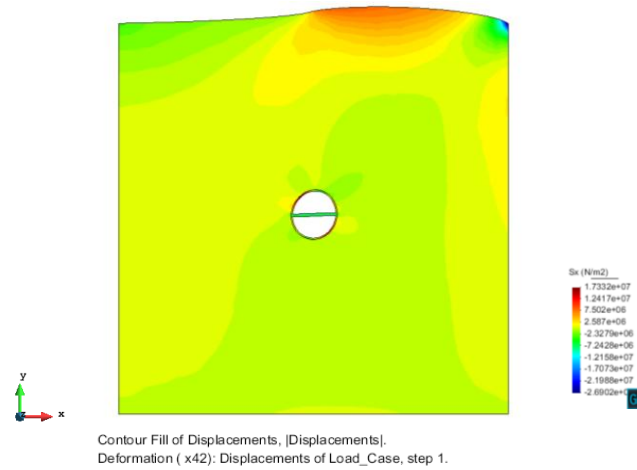


Figure 81. Unloading / excavation model

As can be seen in the more detailed, the tunnel cross section is stretched towards the right side (where the building is located). The red/yellow areas represent tensile stresses while the blue/green ones represent compressive stresses.

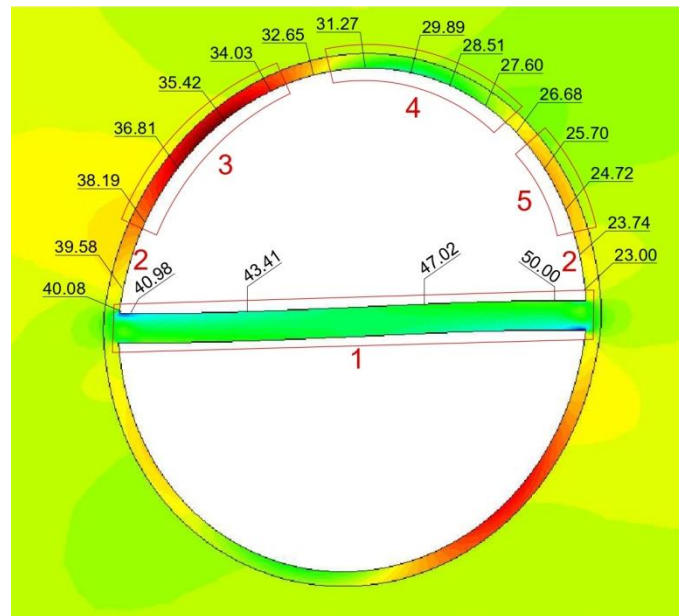


Figure 82. Unloading / excavation model detail with coordinates of fiber

Analysing Figure 82 it is concluded that the unloading process differently affects the marked areas as explained below.

1. **Segment 50-40m** (slab): The slab works as a diaphragm experiencing compression which is logical given the upwards deformation of the section.
2. **Segments 40-39m and 24-23m** (concrete lining close to the slab): The yellow colouring denotes a range of stresses from null to low traction; however, these segments belong to transitional areas between the tunnel concrete lining and the slab, for that the corresponding strain-readings might behave in particular ways.
3. **Segment 33-38m**: This area is clearly experiencing more traction stresses than any other, which implies that its measurements should be the least compressed ones.
4. **Segment 32-27m**: Together with the slab, this area should present measurements that are more compressed than the other areas.

5. **Segment 26-24m:** This section is clearly in traction but less than segment 3. For that, strains between the ones observed in segment 3 and those in segment 4 should be observed along this segment.

6.1.2. Loading model

Figure 83 presents the theoretical model of the structure behaviour being subject to loading processes at ground level. As can be observed, the applied load is opposite to the one in the previous model as well as the effects on the soil, which is clearly under compression stresses (blue colouring). Assuming the foundation slab of 0.8m depth, a concrete slab of 0.3m on each floor, approximated dead loads and live loads regarding residential use, final load of 93kN/m^3 is obtained and applied.

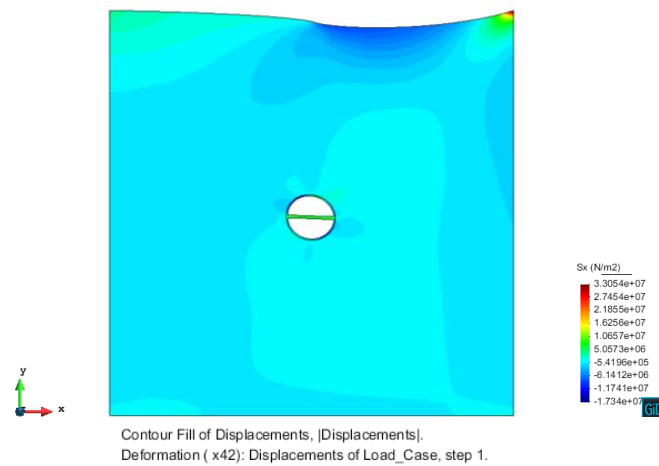


Figure 83. Loading model

The theoretical effects of the construction works on the tunnel lining are detailed in Figure 84. The tunnel cross section is obliquely flattened, generating the opposite stresses from those observed in the previous model.

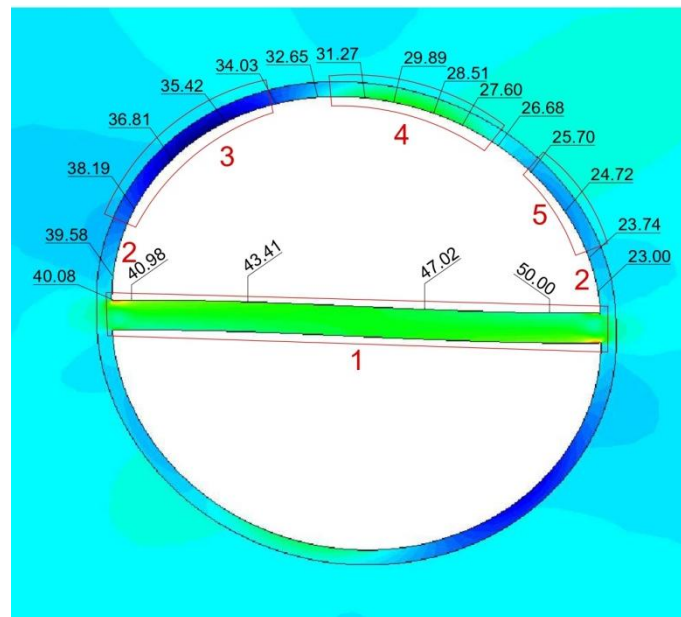


Figure 84. Loading model detail with fiber coordinates

The marked areas in Figure 84 represent the segments of concrete lining that are affected differently by the construction works. They coincide with the differentiable areas of Figure 82 but are now responding to the opposite stresses.

1. **Segment 50-40m** (slab): The slab experiences traction given that the tunnel cross section is deforming downwards and, therefore, pulling the extremes of the slab outwards.
2. **Segments 40-39m and 24-23m** (concrete lining close to the slab): As mentioned before, this is the transitional area between the tunnel concrete lining and the slab, for that, the corresponding strain-readings might behave particularly. However and in principle, light blue colouring denotes a stress range from null to low compression.
3. **Segment 33-38m**: This area is clearly the most compressed one.
4. **Segment 32-27m**: Together with the slab, this area should present the least compressed stresses in all the tunnel cross section.
5. **Segment 26-24m**: This section is clearly in compression but with stresses found between those in segments 3 (high compression) and 4 (low traction).

6.1.3. Conclusive ideas

In conclusion, the models reproduce the opposite effects that the structure is subject to given the two opposite loading cases. Having this basic structural analysis in mind, the interpretation of the strain-readings provided by the DOFS will be easier and more understandable. Additionally and rather more importantly, this previous study will allow for a reliability assessment of the SHM tool that are the DOFS and the monitoring project design itself.

6.2. Observed behaviour of the section and reference points

In this section an analysis of the treated strain measurements, i.e. after anomalies elimination and interpolation procedures described in section 4, will take place firstly presenting and interpreting a 3D figure with all the measurements and later focusing on each structurally differentiable segment of fiber and their representative locations. After that, the computed displacements (defined in section 5) will be presented and assessed.

6.2.1. Strains

6.2.1.1. 3Ds. Global analysis

The global overview of the treated strain measurements provided by the DOFS and its post-processing is presented in Figure 85. As can be observed in the figure, the initial measurements are green corresponding to null or very small strain variations, which is logical given that those correspond to the monitoring period right before the start of the excavation works. Therefore, no loading processes were happening and, consequently, the structure did not present affections.

Later, the tendency is towards negative strain values, which means compression and seems to be coherent given the nature of the construction period that is excavation, i.e. unloading of the structure that translates into compression on the lower fiber of the concrete lining.

After reaching a minimum of approximately $-260\mu\text{strains}$ in the most critical location and around February, the strain profile slope is inverted reproducing a decompressive process as the negative strains are being reduced in absolute value getting closer to zero.

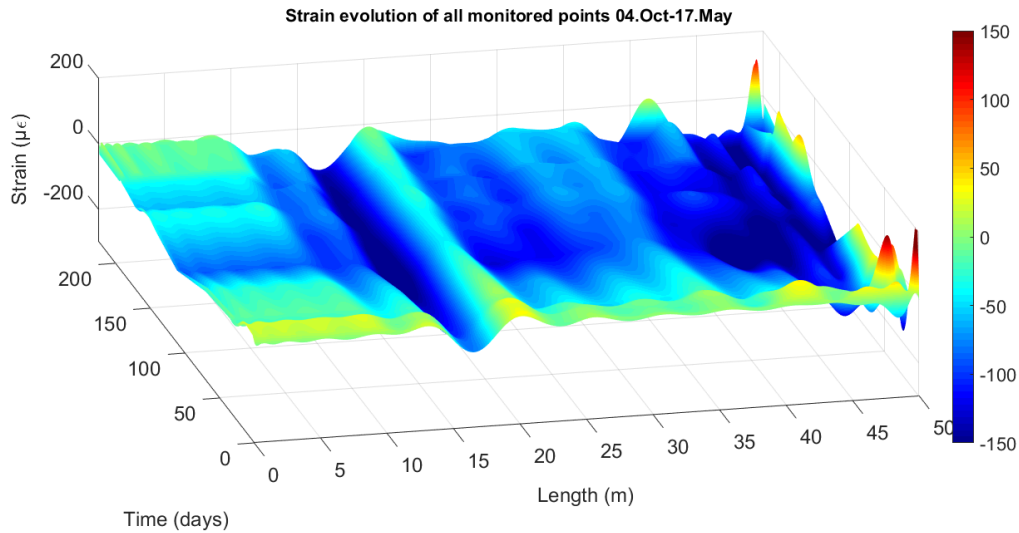


Figure 85. Strain evolution at all times and locations (same as Figure 72)

It can be then said that, at first glance, the measured strain profiles coincide with the structural analysis and, therefore, that the DOFS readings are reproducing the behaviour of the underground structure. In order to guarantee the reliability of such monitoring method for the developed case study, an in depth analysis of the results for each particular segment of the fiber is presented below.

Now the structurally differentiable segments of the optical fiber will be analysed separately. The 3D figure presented in section 3 when describing the DOFS monitoring setup is introduced here as well to have in mind the different fiber segments that will be analyzed.

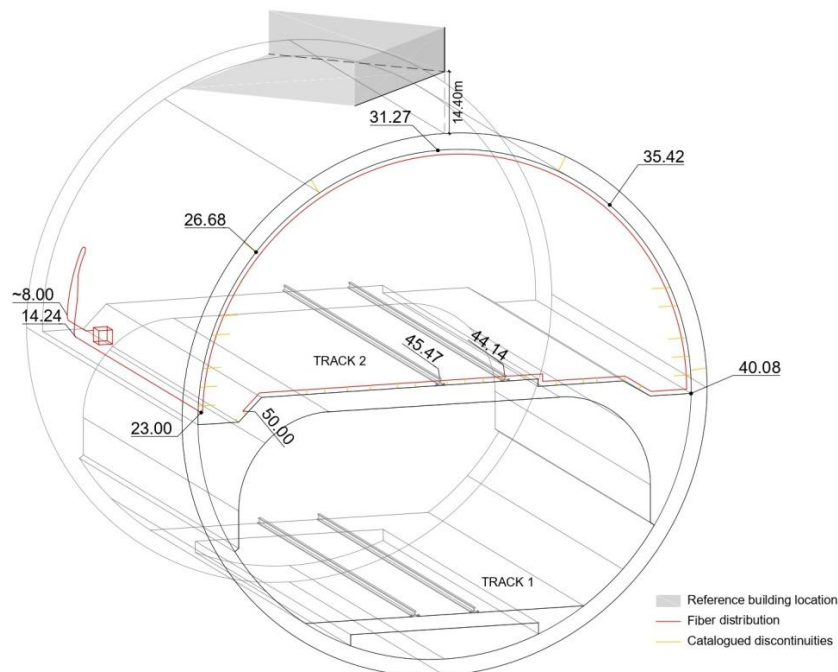


Figure 86. 3-Dimensional representation of the DOFS monitoring scheme

Additionally, a plan view of the 3D figure is used to provide a global visual appreciation of the segments that present different structural effects along the 50m fiber for being bonded to sub-structures that behave differently when loaded.

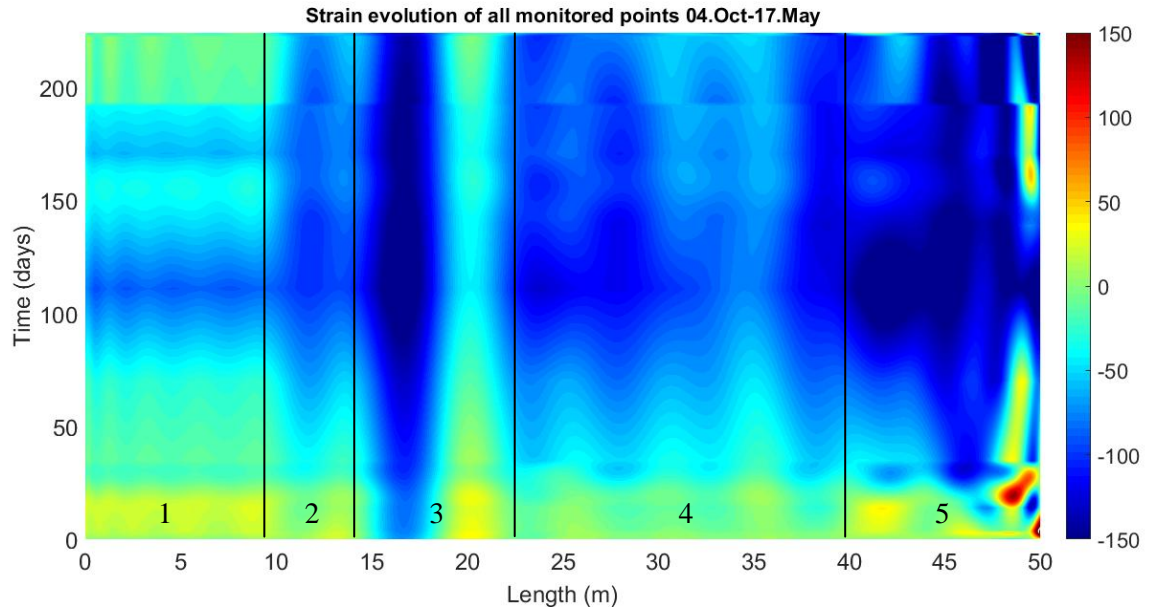


Figure 87. Plan view of strain evolution at all times and locations

As can be observed comparing Figure 87 and Figure 86, the five differentiable behaviours correspond to the fiber lengths covering the five different substructures: 0-9m (unbonded fiber segment), 9-14m (partial sectional monitoring segment), 14-23m (longitudinal tunnel segment), 23-40m (complete tunnel transversal section segment) and 40-50m (upper fiber of the tunnel slab). The mentioned structurally differentiable segments are analyzed separately bellow.

1. 0-9m (unbonded segment)

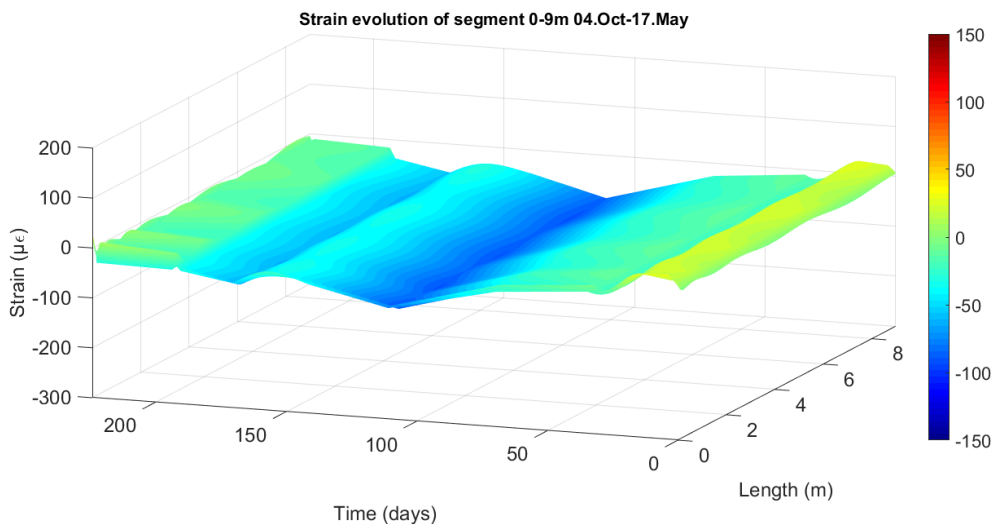


Figure 88. Strain evolution in 0-8m segment

As mentioned in the introductory sections, the unbonded fiber segments do not provide strain measurements per se but reproduce instead the effects of temperature variations on the measurements. The data collected from these segments can be useful in the case of long-term monitoring campaigns because it allows for correction or compensation of the strain readings along the bonded segments affected by temperature variations.

This idea has been developed in previous research campaigns; for example, [46] where it has been named thermal compensation and has been proved to be successful when attempting to obtain a resulting data set that presented pure mechanical strains along all the fiber length. The removal of thermal strains is achieved by subtracting the thermal effects outputs from the unbonded segment of the fibre to the total strain measures in all the points of the bonded segment.

In this case, considering that the location of the fiber setup is a metro tunnel at 14m underground with no affections from the outside weather conditions, it can be concluded that the temperature variations are negligible given that temperature remains rather constant in that location during the whole year and, consequently, during the monitoring period.

However, some oscillations are observed in the unbonded segment (Figure 88) remaining constant along the 9m length, which induces the thought of actual displacements occurring between locations 0m and 9m. This segment is not bonded to the structure with epoxy resin but it is attached to it with duct tape (see Figure 89) for protective reasons since damage at any location of the fiber could unable its monitoring ability. Therefore, the readings can end up presenting variations due to minor displacements between the measuring points of this segment that can be roughly computed as shown below. Being the approximate minimum of the strains readings in this segment $-50\mu\epsilon$, the displacement between the extreme points of the study interval can be computed as

$$50\mu\epsilon \cdot 9m = 450 \cdot 10^{-6}m = 0.45mm$$

Therefore, any displacement of 0.45mm could explain the seen oscillations being this option more plausible than the temperature variation for it being non-existent and given the particularly high sensitivity of the DOFS when measuring strains.



Figure 89. Not bonded segment

2. 9-14m (partial sectional monitoring segment)

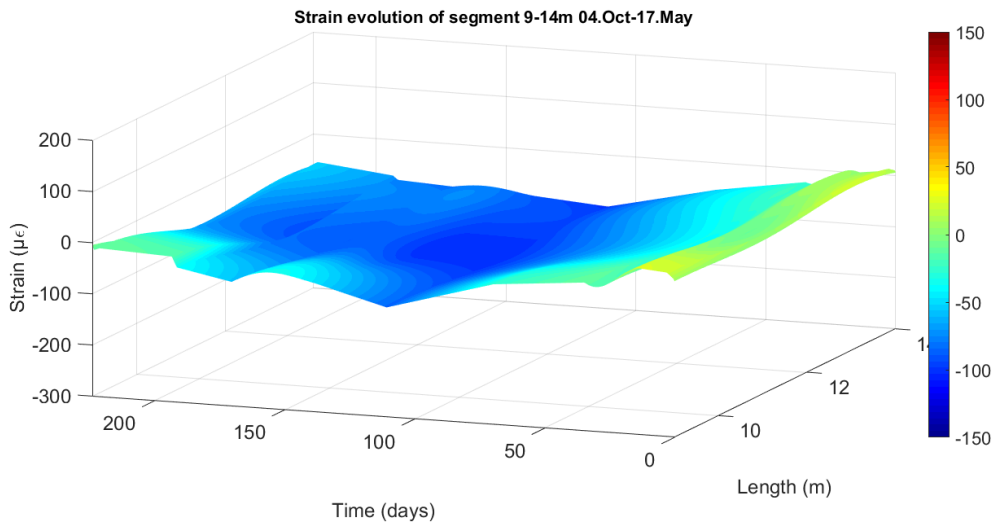


Figure 90. Strain evolution in 8-14m segment

This segment corresponds to the fiber length covering a small portion of a tunnel transversal section. Only the first 3m of the tunnel vault are covered and then, the fiber goes down towards the monitoring device location (see Figure 91). It is interesting to see that the covered length is subject to similar deformation processes as the ones observed in the completely covered section (23-40m) given that it belongs to the same structural scheme (a cross section). This can be easily observed by comparing segments 2 and 4 in Figure 87:

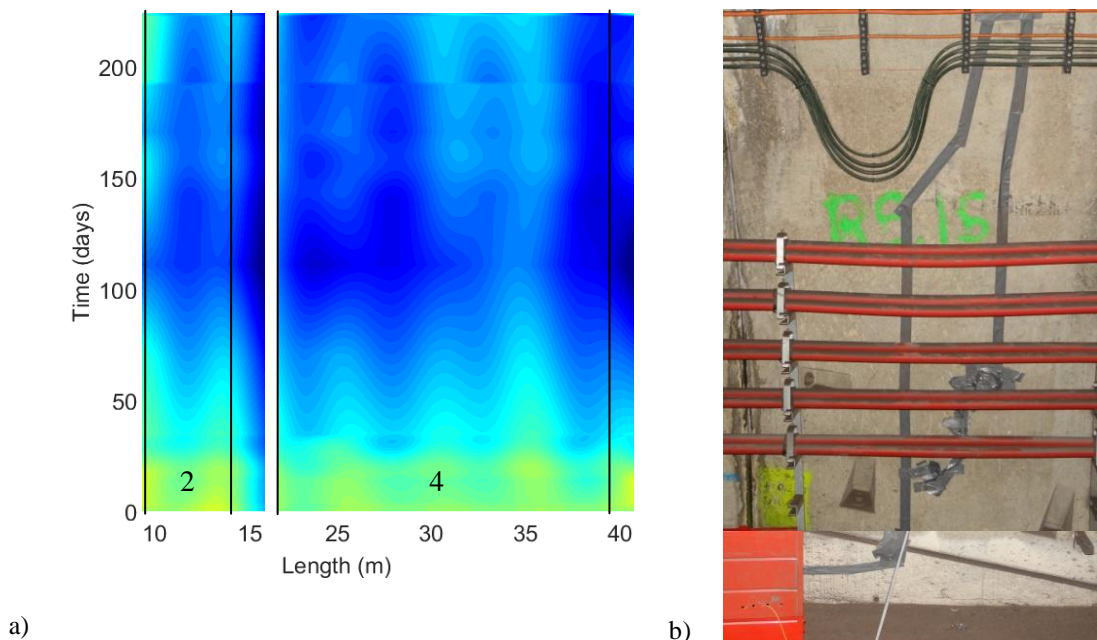


Figure 91. 8-14m fiber segment a) comparison of segments 2 and 4 (particularization of Figure 87) and b) site picture

Also, the maximum compressive strains (around $-100\mu\text{strains}$) are much inferior to the ones measured in the complete section (23-40m segment) as this one is 10m away from the critically loaded section.

3. 14-23m (longitudinal tunnel segment)

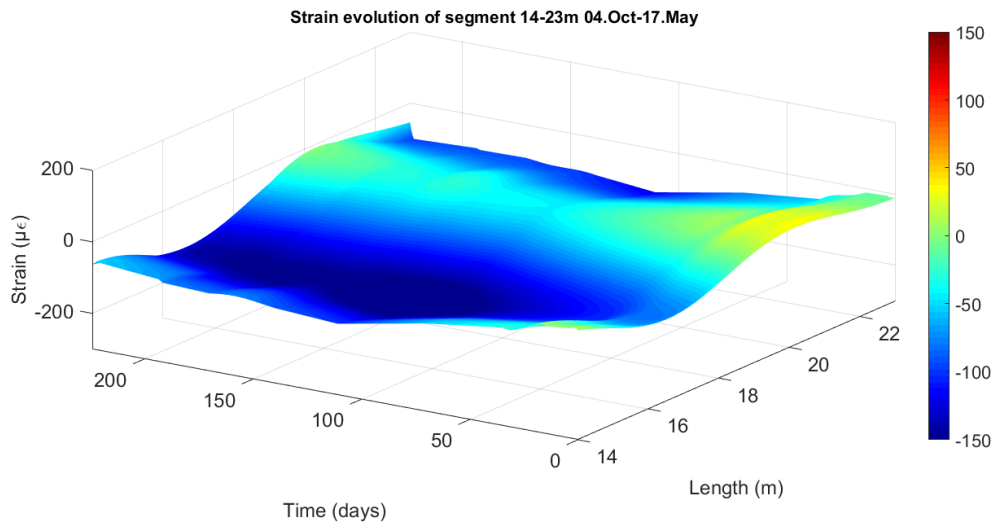


Figure 92. Strain evolution in 14-23m segment

Firstly, considering the plane strain state this structure is subject to, it can be said that the concrete segments cannot deform in the axial direction of the tunnel. Therefore, the compressive tendency of this fiber segment makes sense given that, when the structure is unloaded, the segments that become axially tractioned attempt to deform but, since this deformation is restricted by definition of the structural state, the segments experience an even higher compression.

In this 9m long fiber segment, two clearly differentiable processes are happening. Up to fiber length 18.5m a significant compressive process is taking place, whereas in the surroundings of fiber length 20m the compression is not so considerable. As can be seen in the tunnel plan view (Annex 2 or Figure 93), this might be because of the presence of several cracks in the first half of this segment which weakens that segment making it more liable to deformation.

It is important to have in mind that this segment was particularly affected by anomalous behaviour due to the amount of discontinuities the fiber setup was subject to (mainly joints between the concrete lining segments). Therefore, this graph, being an approximation of the collected data itself, might be more affected by anomalies than the other segments.

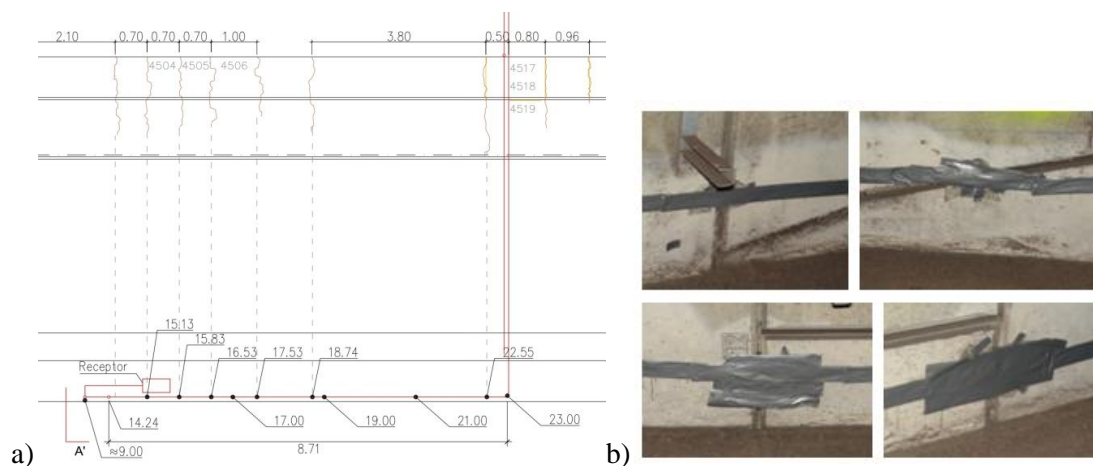


Figure 93. 14-26m segment setup with a) detail of tunnel plan view and b) site pictures of discontinuities

4. 23-40m (complete tunnel transversal section segment)

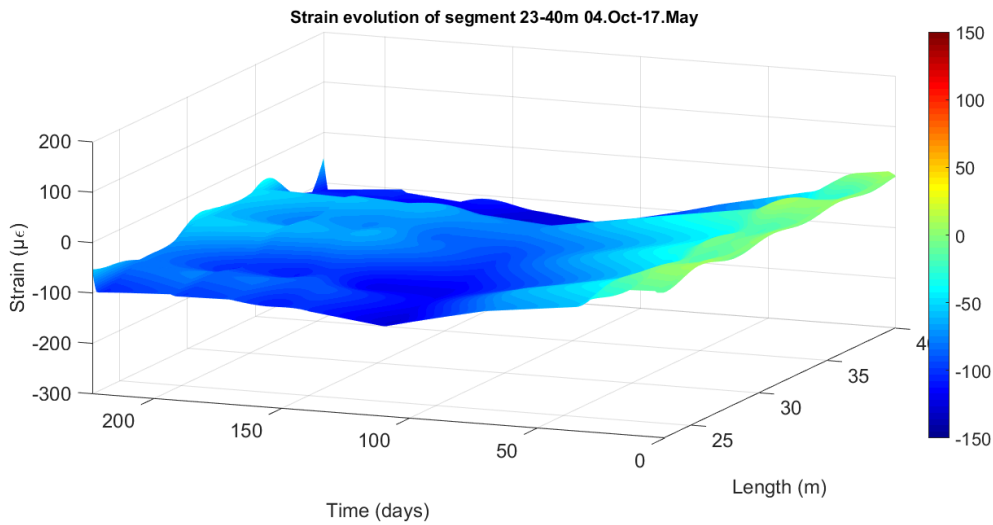


Figure 94. Strain evolution in 23-40m segment

The readings of this segment should reproduce the observed theoretical behaviour on the tunnel's vault. Since the last reading was executed on the 17th May, the measurements profile does not get to fully reproduce the deformations caused by the ground level loading. It can be intuit, however, how the compression starts diminishing and strains start getting lower (in absolute value) in the middle of the graph (end of January) which means that there's traction in the lower concrete lining fiber and that the effects of the loading works (construction) start compensating the unloading operations (excavation).

Remembering that the building construction site covers half of the tunnel layout, it must be said that, in the later graph, it is difficult to appreciate the particular behaviours of the two differently loaded halves of the tunnel. For that, this segment will be analysed in detail by means of the representative points in order to check if the readings reproduce the theoretical behaviour of the tunnel's vault presented in Figure 82 and Figure 84.

5. 40-50m (slab segment)

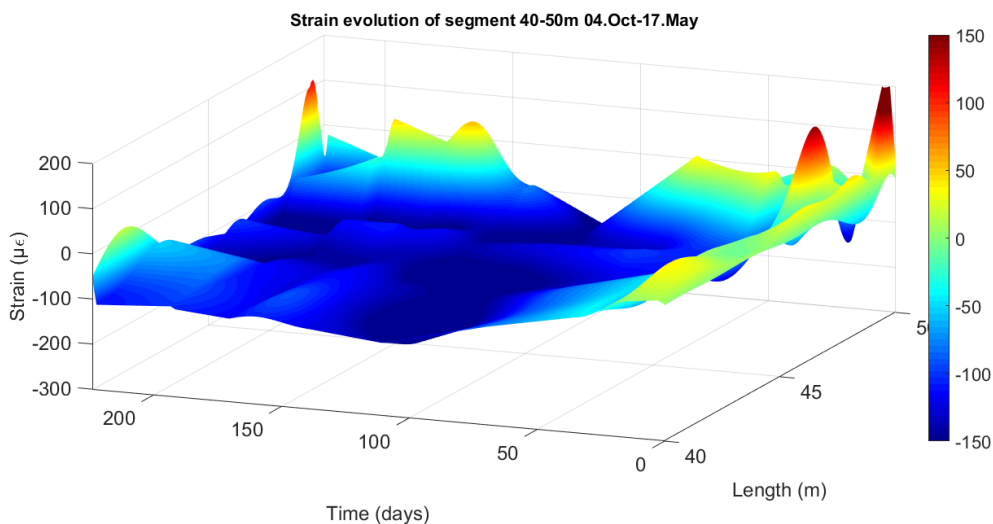


Figure 95. Strain evolution in 40-50m segment

This is clearly the area with the highest compressive strains (darker blue). This behaviour is logical given the upwards stretching of the tunnel cross section in the unloading scenario (see Figure 81) that pushes the extremes of the slab together compressing it. We can expect from these locations to end up inverting their structural state in future measurements in relation to the rest of the fiber, i.e. enduring the lowest compressive stresses of the whole monitoring length when the loading processes fully substitute the excavation effects.

As can be seen, the strain profiles in the last 2.5m of the fiber are significantly affected by peaks, which were not possible to remove during the data post-process. However, being the nature of the high values so punctual and considering that the location of the last segment is a passable area with not a very smooth surface, the appearance of peaks and distorted profiles can be explained without implying structural damage.



Figure 96. Last meters of the fiber

6.2.1.2. 2Ds. Representative points

The effect of the different construction works on the tunnel concrete lining is better observed by means of the so called representative points. These are determinate measures located in the structurally differentiable segments of the tunnel cross section (defined in the theoretical models presented in Figure 82 and Figure 84) and not affected by reading anomalies. Conclusions regarding the structural behaviour of the structure can be easily extracted and understood from these particular points presented in Figure 97.

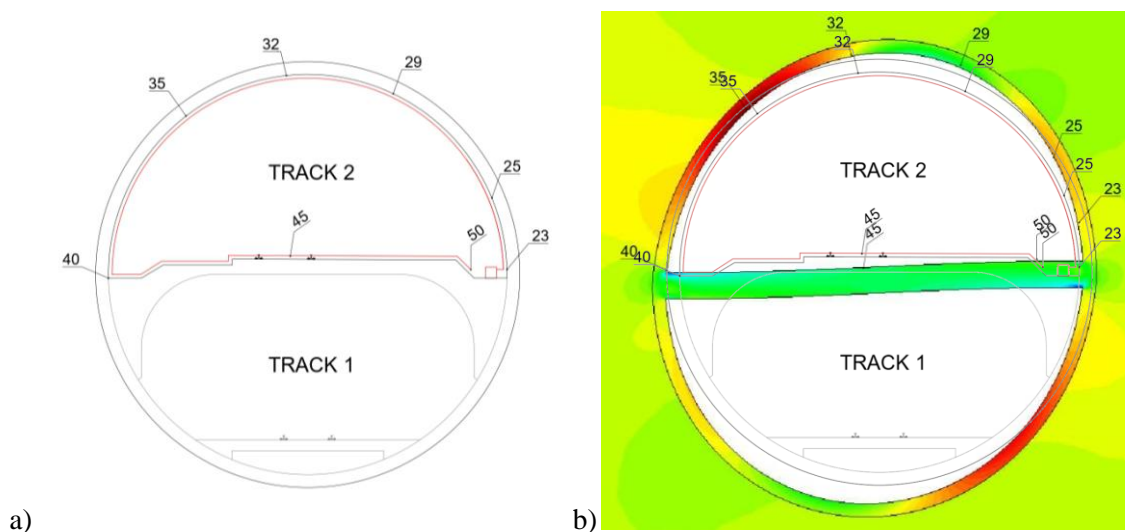


Figure 97. Representative points in a) tunnel cross section and b) structural loading model

In order to check the accuracy of the strain readings, Figure 98 and Figure 99 have been developed showing the strain evolution of the representative locations during the whole construction period (from 4th October 2018 to 17th May 2019).

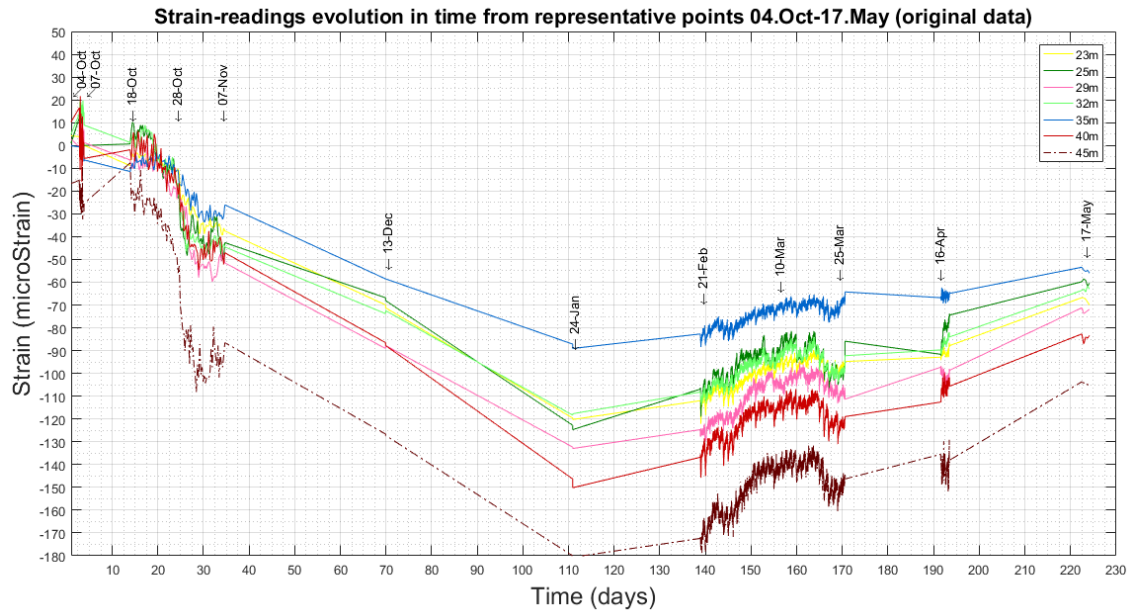


Figure 98. Strain evolution of representative points from 4th October 2018 to 17th May 2019 (original data)

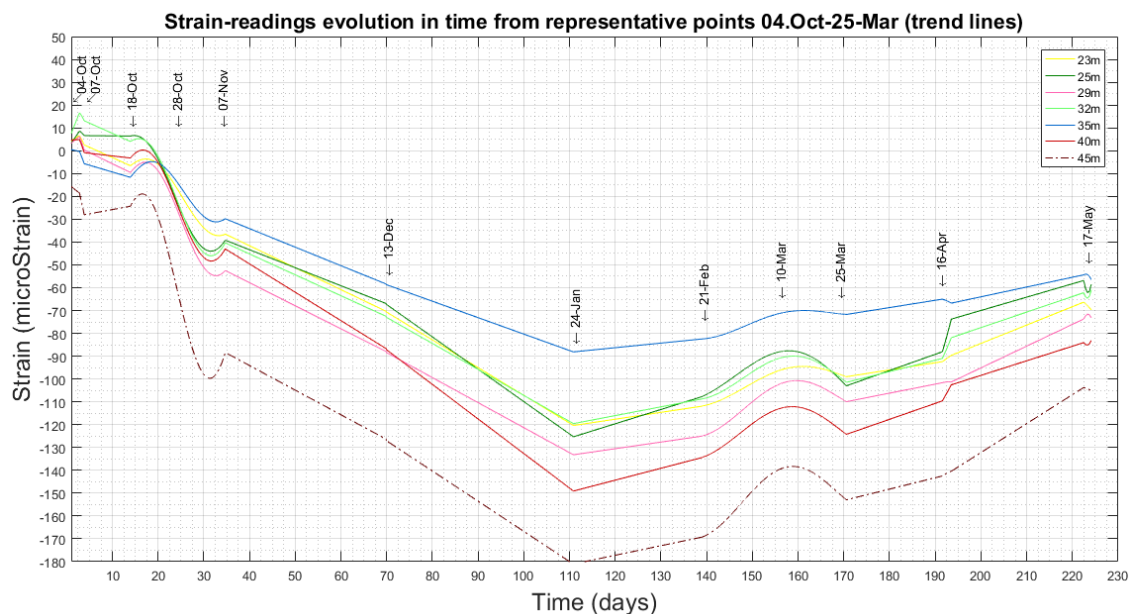


Figure 99. Strain evolution of representative points from 4th October 2018 to 17th May 2019 (trendlines)

Figure 98 presents the original strain measurements obtained right after the ODiSI-A post process and Figure 99 presents the strain evolution provided by the treated data. Since these points do not present anomalous behaviour (they were specifically chosen for that) their treated strain profile, which was obtained by means of trend lines, is really close to the original data. It is interesting to present both diagrams to show the difference between the original and post-

processed data and to prove that looking back to the original readings is both helpful and necessary.

In this case, the monitoring periods are clearly marked in Figure 98 by the characteristic noise and changes of slope, whilst the treated profiles in Figure 99 show much smoother tendencies. The later presents some changes in slope as well, which might seem unexpected due to the definition of trend lines (explained in section 4); however, these are not out of the normal considering the ill conditioning of the polynomial approximation. That is the variability of available measures along the monitoring period as there are long periods with very few data and others with much denser collections.

To enter the representative point's structural interpretation subject some comments regarding the monitoring periods must be firstly noted. The initial measures (between 4th and 7th October, before the excavation works started) were conducted with small time intervals between them (30 minutes maximum) and, considering the metro traffic frequency of 10 minutes, it is logical that the point profiles present irregularities in those times, even being representative points specially selected. Later on, the monitoring period that covers the excavation works that took place from the 7th October till approximately the 9th November, presents a strong increase of the compressive strains (downwards) clearly reproducing the unloading effects of the excavation works. These effects are appreciated during the two following monitoring episodes in the 13th December and 24th January. It is worth noticing that these periods were critical given that the reading processes failed and the only available data measurements were collected manually during the programmed data and device collection visits.

The next measures, taken between the 21st February and 25th March, already present the compensating effects of construction works (decompression); therefore, the real compression maximum is found close to the 24th January marking approximately two and a half months between the end of excavation works and their final effects on the structure. This aspect claims again the previously commented soil consolidation effect. It is clear that the transmission of loads applied at ground level to the structure located 14m below is not instantaneous, indeed it can take between two weeks and two months, according to the analysed data, for the response to a particular applied load to be monitored by the DOFS.

The construction works that are causing the change of tendency started around the end of December with the joint 1 foundation slab completed on the 20th December followed by the on in joint 2 finished by the 10th January. By the beginning of March, the ground floor slabs of joints 1 and 2 were already executed as well as the walls and pillars of the first floor in joint 1 and the foundation slab in joint 3 (see Figure 100). Therefore, significant works had been executed preceding the March monitoring period, clearly enough to compensate for the excavation unloading and start decompressing the lower fiber of the tunnel lining.

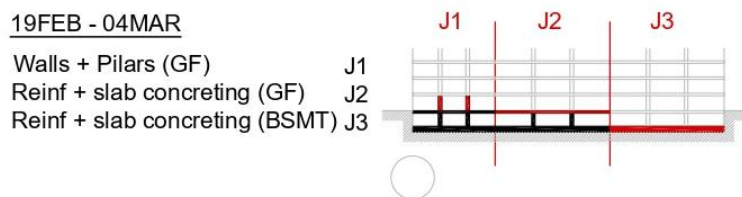


Figure 100. Construction works completed by the beginning of March.

At the end of March a reduction in the strain decompression slope can be appreciated, which, after some thought process regarding the timeline of works, was possible to explain as follows.

As mentioned in the construction timeline, the works present at all times greater development in joint 1 (the one above the tunnel) than the other two, with an advantage of 1 floor with respect to joint 2 and two with respect to joint 3 (see Figure 101).

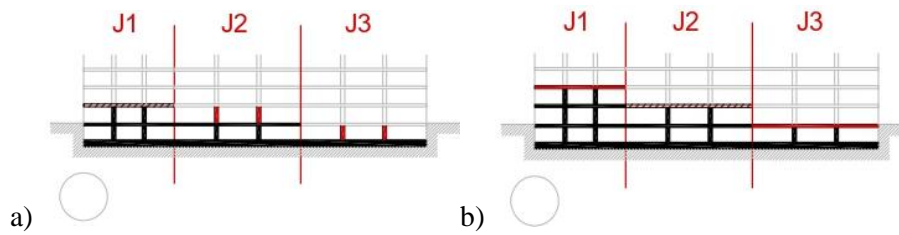


Figure 101. Relation between the three joints regarding construction time-line in a) 18th March and b) 18th April

The works in joint 3 started around the end of February, from which it is deduced that the loading of the further area from the tunnel layout slightly unloaded the soil corresponding to joint 1 by inducing a balance sort of behaviour between joint 1 and 3, explaining the decompressing profile slope reduction.

After that, the tendency observed after the 16th April and 17th May monitoring episodes (being the first one short due to a monitoring failure and the later executed in the data collection programmed visit) is still of decompression but with a minor slope.

Now, the evaluation of each representative point shown in the diagram of Figure 98 and Figure 99 will take place.

- **Point 45** (brown dash dot line) is located in the slab segment and presents the highest compressive state as was expected since the slab is supposed to work in compression during the unloading phase as explained in the 3D Figure 95.
- **Point 40** (red line) comes next as it is the second most compressed point, which makes sense given its location in the left hand side corner really close to the slab but located on the concrete lining surface, which, according to the model, is supposed to experience high compression as well but slightly less than the slab.
- **Point 29** (pink line) is located close to the keystone of the tunnel slightly to the right. It could be defined as the closest point to the application of loads and, since the tunnel section deforms towards loads application area, point 29 presents the second highest compressive state (right after the already presented point 40).

As can be seen, points 40 and 39 have similar strain evolutions, in fact, up to the 13th December, point 29 is more compressed than point 40, which might be explained by the sequential loading of the tunnel substructures, meaning that the loading processes get first to the upper concrete lining and later to the structures found below.

It is also noticeable that points 23, 32 and 25 present similar tendencies even while being located in different areas.

- **Point 23** (yellow line) is found in the right hand side corner, roughly 50cm above the floor slab, which relieves it from the characteristic high compressions of the slab experimenting medium ones typical from the transitional areas between the high deformation concentration zones.

- **Point 25** (dark green) is located above point 23 and corresponds to a section with slightly higher traction (barely noticeable at determinate times) than 23. Even though it is found in the centre of what could be identified as the first quadrant of the tunnel cross section, the experimented traction is not the highest for it belonging to the unloading / loading side of the tunnel which induced an oblique deformation of the tunnel towards the construction site.
- **Point 32** (light green) can be found in the second quadrant of the tunnel cross section really close to the keystone. It represents the beginning of the fiber segment that experiences higher traction deformations.

Finally the, red area of the modelled structure is characterized by point 35.

- **Point 35** (dark blue) belongs to the least compressed segment between lengths 33 and 38m of the fiber setup. Except for the initial measurements, which was described before as not really representative, the strain readings are the lowest in absolute value during all times.

Regarding the strain readings it can be concluded that they reproduce quite accurately the expected behaviour stated in the theoretical model. It can be consequently expected that, after the future monitoring campaigns take place, the readings will probably end up reproducing the loading model (see Figure 84) just as they reliably reproduced the initial unloading model.

6.2.2. Displacements

The section convergence was computed by means of the theoretically developed formulas presented in section 5.

Firstly, since the displacements computation was executed for the monitored tunnel transversal section, i.e. 40-23m fiber segment, the post-processed strain readings corresponding to this segment and for particular monitoring times are presented in the following figure.

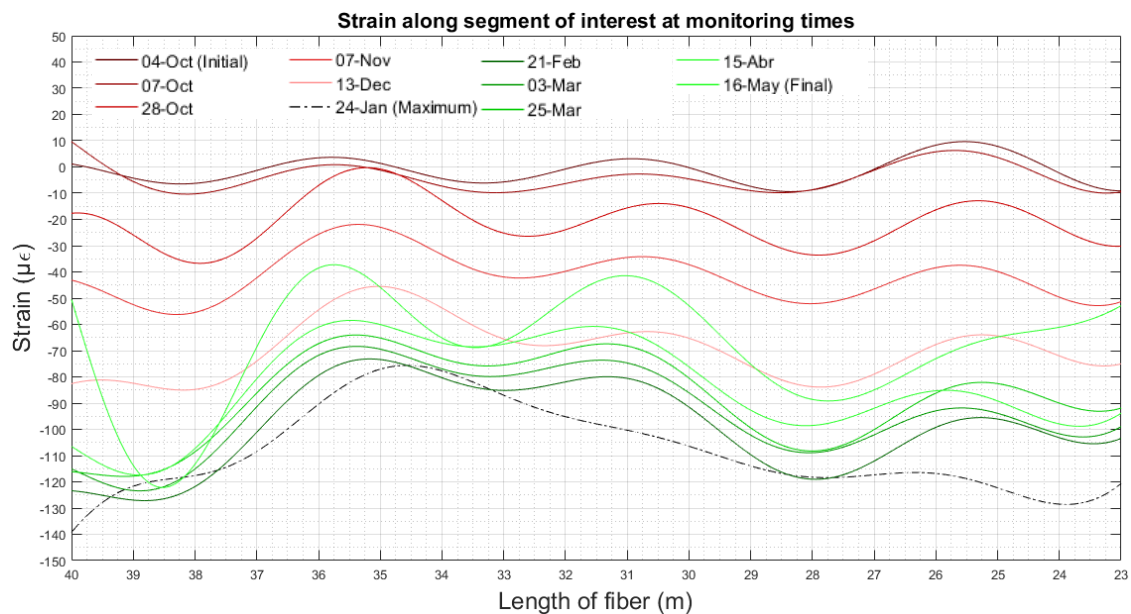


Figure 102. Strain readings along transversally monitored tunnel section at different times

The results presented in the following page, represent the computed displacements considering null displacements and rotation at the initial point ($x=40m$), i.e. the conditions case 0.

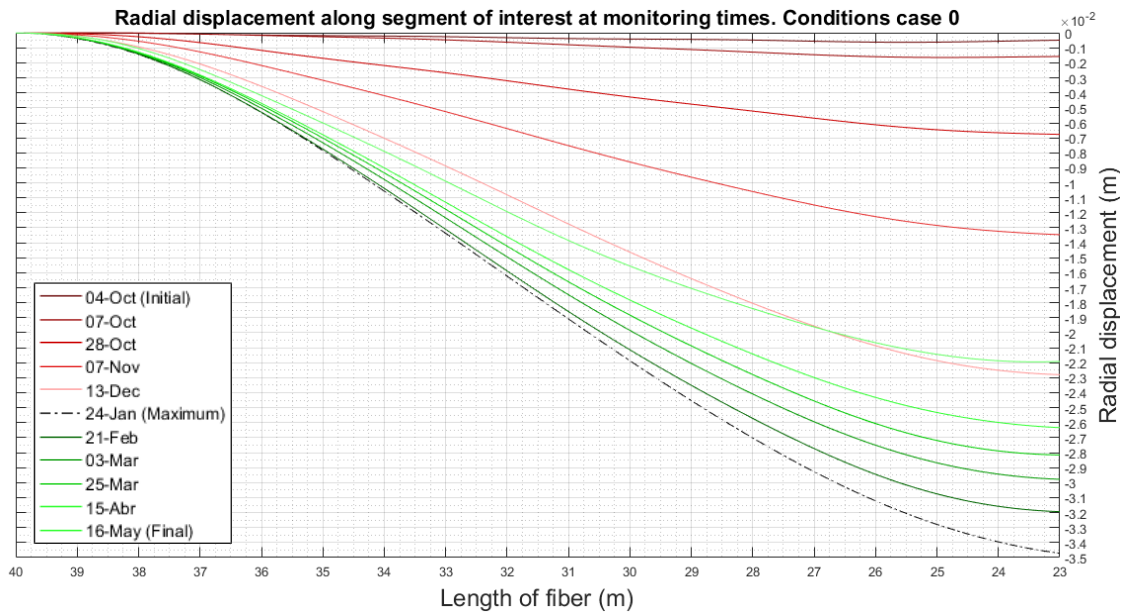


Figure 103. Radial displacements along transversally monitored tunnel section at different times for case 0

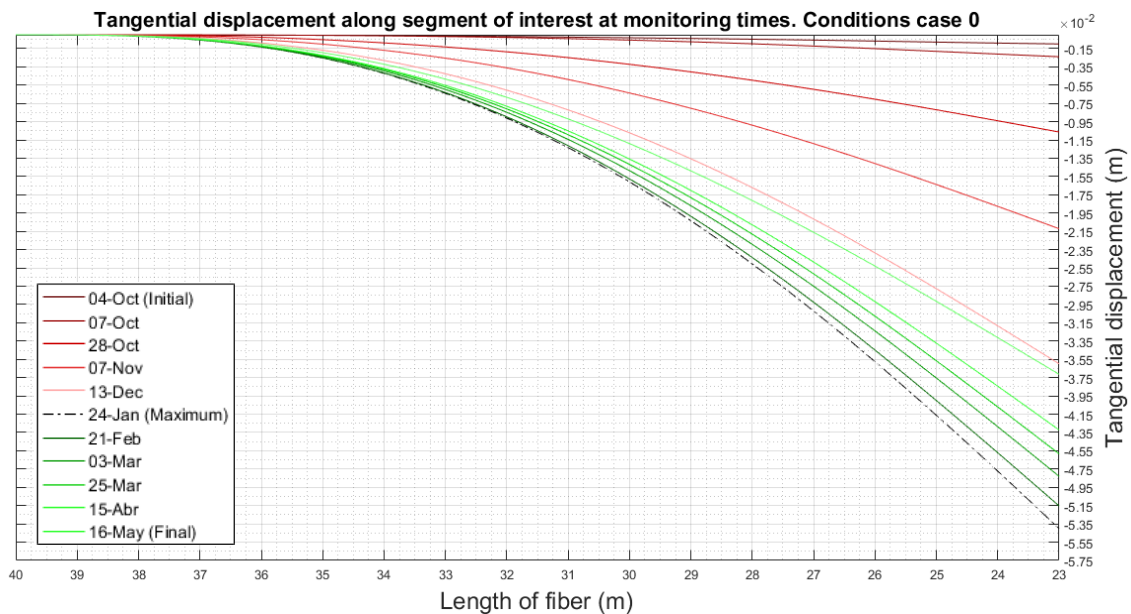


Figure 104. Tangential displacements along transversally monitored tunnel section at different times for case 0

These results could be considered correct magnitude wise, since the order is of centimetres, and regarding their signs, when considering the axis direction (shown in Figure 79), it would mean the section deforms upwards. Additionally, it can be observed that the displacements increase in time up to the 24th January and from that date, they start decreasing again, which is coherent with the strain reading results presented in the previous section.

However, the tendency marks that the maximum displacement is achieved for all readings in the last point of the segment $x=23\text{m}$ (as shown in Figure 105). As can be observed in the developed geometry, the computed convergence is not consistent with the theoretically developed model, which clearly shows that the maximum displacement should be found in the monitored location that is closest to the application of loads, i.e. a point between 31-28m (see Figure 82 or Figure 97).

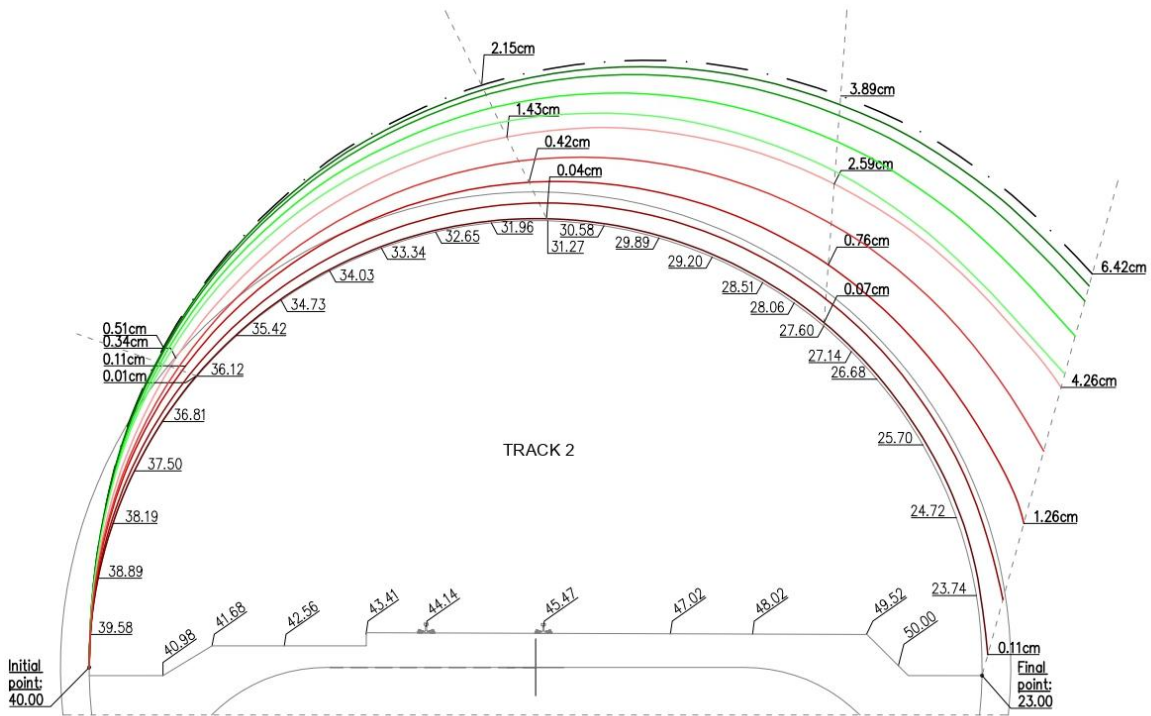


Figure 105. Computed total displacements along transversally monitored tunnel section at different times for case 0

In order to solve the aforementioned tendency issue further considerations regarding boundary's conditioning are applied. In section 5, two possible cases regarding boundary conditions were presented, which were defined by equations 21.A and 21.B respectively. The following diagrams represent the first case. The hypothesis established for each reading in option A is that the first point of the integration interval has null displacements and a rotation such that the radial displacement in the final point is restricted / minimized.

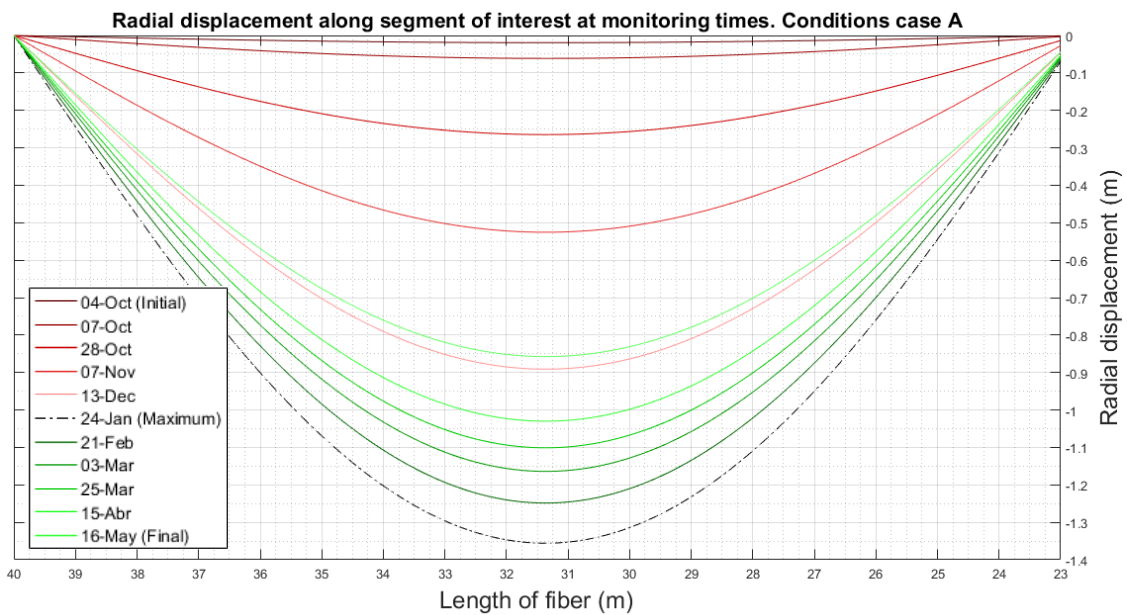


Figure 106. Radial displacements along transversally monitored tunnel section at different times for case A

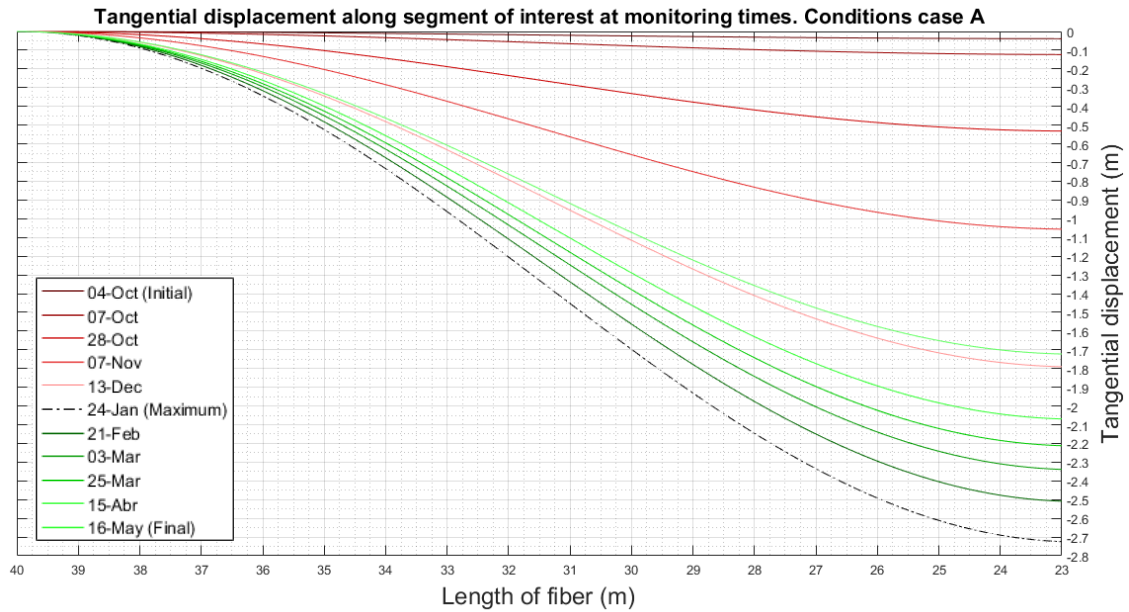


Figure 107. Tangential displacements along transversally monitored tunnel section at different times for case A

Establishing boundary condition A led to the above diagrams, which, first of all, do not provide reliable data regarding the magnitudes. Additionally, the issue here is that the maximum displacement is found in the keystone of the tunnel (approximately $x=31.2\text{m}$) while, as mentioned before, it should be located somewhere in the right side of the section.

Nevertheless, in Figure 106 and Figure 107, the tendencies make sense since they reproduce the upwards displacement of the section and limit the radial displacement on both extremes, a computation that could be reproducing the effect of a considerable redistribution of loads in the soil separating the structures that allows the loads to reach the structure homogeneously, i.e. without the structure perceiving the asymmetrical loading scheme.

All in all, the excessive magnitude of the presented displacements leads to believe that an additional condition regarding the tangential displacement is required. When considering the proposed boundary conditions of case B, the following diagrams are obtained.

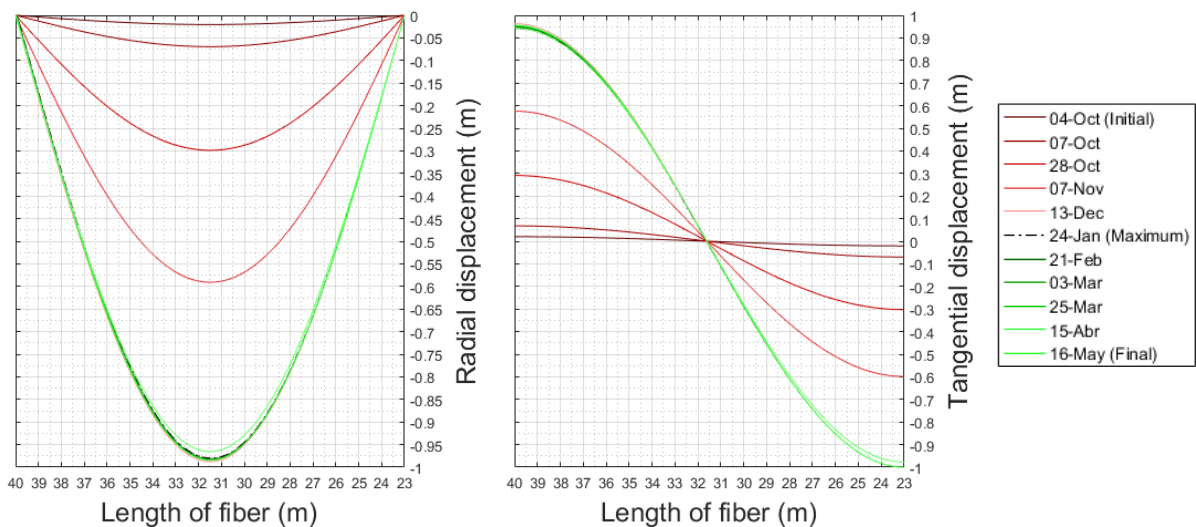


Figure 108. Displacements along transversally monitored tunnel section at different times for case B

It is clear that, magnitude wise, the displacements in Figure 108 don't agree with the theoretical convergence (reaching 1m in the extremes regarding tangential displacements and in the centre regarding the radial ones). However, they present a coherent tendency reaching the maximum displacement exactly where the tangential one is null.

When trying to find a solution regarding the shown inconsistencies, a possible misconception of the theory developed in section 5 was considered on which no apparent theoretical errors were found. Several trial runs regarding the components of each formula were made in order to see whether some variations in each component led to more consistent displacement values and tendencies along the fiber.

The findings of these final trials revealed an interesting option which involved the computation of the inverse method explained in section 5 and simply consisting on an evaluation of the transversal section from the other side, meaning from $x=23\text{m}$ to $x=40\text{m}$. This allows to impose the final displacements (at $x=40\text{m}$) to be null and to look for the initial displacements (at $x=23\text{m}$) that achieve that. The solution to this is found below:

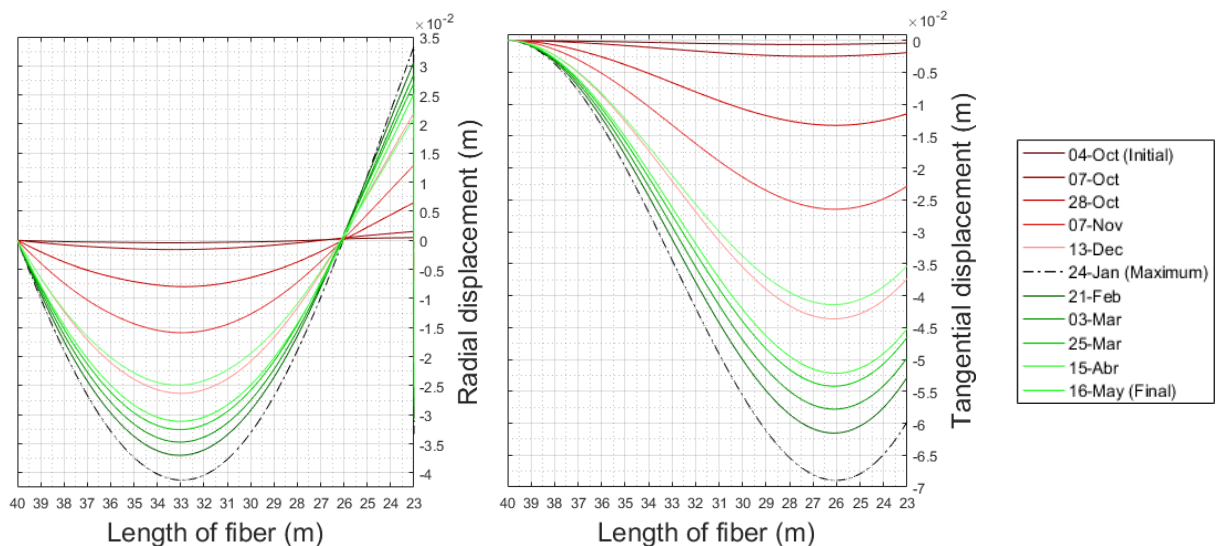


Figure 109. Displacements along transversally monitored tunnel section at different times for case C

The last diagram provides reasonable convergence values. However, the tendency is still not optimal yet given that the tangential displacement is always negative, which translates into the tunnel section rotating anticlockwise, and that it reaches its maximum magnitude around fiber length 26m coinciding with the null radial displacement. Additionally, the maximum radial displacement is found in coordinate 33m (in the left half of the tunnel section), which is the opposite regarding the theoretical model.

Finally, it was deduced that, perhaps, the radial displacement at fiber length 40m did not have to be restricted given that the load is applied on the right side and it might pull the section upwards and a little bit to the right. When the radial displacement at 40m was set free, the diagrams obtained after the minimization of the tangential displacement at 40m where the ones shown in Figure 110.

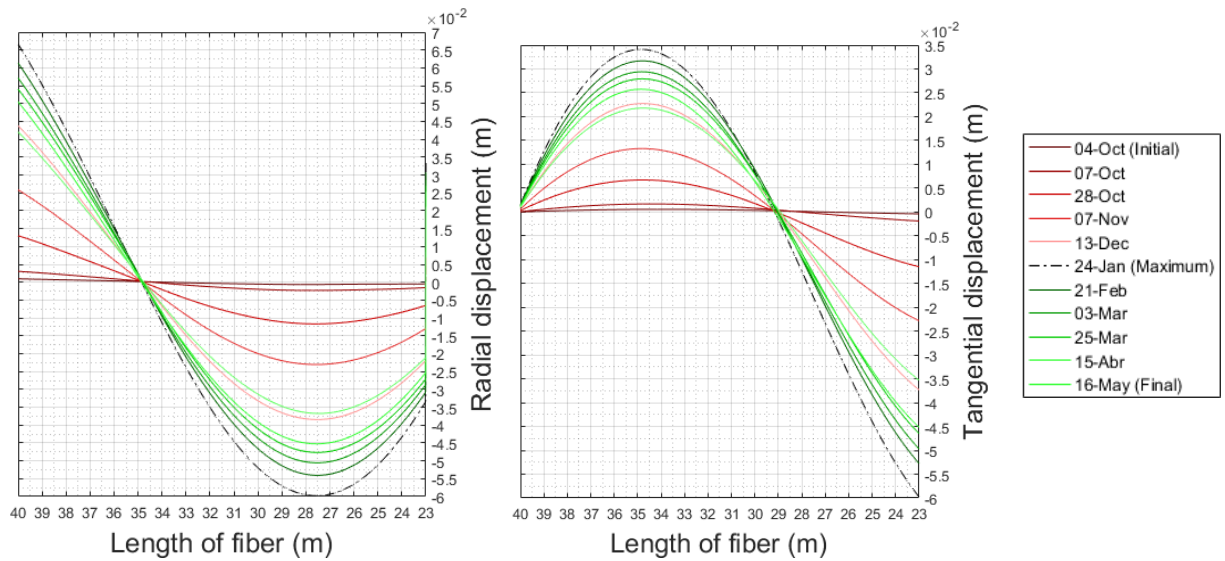


Figure 110. Displacements along transversally monitored tunnel section at different times for case C with radial displacement at 40m free

Among all the set show, these diagrams do provide the best results even though being a bit high. The radial displacements from 40m to 35m are positive, which translates into this segment moving slightly towards the centre of the tunnel. In this segment the tangential displacements increase responding to the traction that was explained with the theoretical model reaching a maximum at 35m (the most tractioned point, see Figure 98 or the theoretical model). Then, the both start diminishing up to fiber length 27.5m, where the radials reach the maximum negative value and the tangential are null, clearly reproducing the deformation of the section towards the building position.

7. Conclusions

7.1. Case study

7.1.1. DOFS performance

Overall, a few conclusions can be extracted from the performed strain readings analysis.

Firstly and more importantly, it seems that the DOFS readings quite accurately reproduce the tunnel deformation process. The tendencies observed were expected and can be explained simply through a proper interpretation of the case study and its structural and loading conditions. The theoretical model developed with GiD provided some insight as well regarding the structural behaviour of the tunnel concrete lining.

All readings can be considered accurate with the exception of the anomalous behaviour of some particular points, which was dealt with in section 3 and required an indispensable treatment for the data set to be visually interpretable. The outcome of the data post-processing involved two strain readings data sets; the first one can be used to detect local damage observing the strain peaks evolution (given that the majority of strain reading anomalies have been eliminated) and the second one to interpret the global behaviour of the structure (since it provides a very smooth surface of strain tendencies). It is important to stress that BOTH post-processed diagrams need to be evaluated after every monitoring period because together they provide the required information to perform adequate SHM for the case study and extract the pertinent conclusions regarding safety.

Additionally, regarding data post-processing, it is crucial to treat the raw strain measurements if one wants to use them to compute derived mechanical properties, such as displacements or stresses, given that the anomalies carry many errors and will definitely induce over-dimensioned results.

It is worth noticing that, given the lack of a continuous monitoring tool, i.e. nonstop readings during the whole construction process, the particular effects on the strain profile slopes of each constructive step, meaning, for example, the conclusion of each floor, are very hard to appreciate in the strain profiles. Even the concreting works, understood as superficially distributed load applied in a significantly reduced time interval and considered as the largest loading events, are difficult to observe in the strain profiles of each monitoring point.

As commented during the analysis, the structural response of the tunnel due to a determinate action at ground level can be monitored logically only after the soil consolidation period, i.e. when the underground structure is undergoing the loading effects itself and therefore transmitting them to the fiber. This time interval can involve several months. In the case study, even if the excavation works were concluded around the 10th December 2018, the unloading effects were still being detected in the readings (reproducing structural compression) at the beginning of February 2019.

Therefore, if the monitoring conditions stay unaltered, future monitoring campaigns will probably reproduce the loading model due to the building construction (see Figure 84) just as they reproduced the initial unloading model due to the excavation works.

However, as a personal opinion with regards to the time interval between action and response, the nature of the case study is quite unfavourable regarding safety assurance. The effects of one action can only be detected some months after its application. During this time interval more loading processes will take place responding to the construction project, and, if that mentioned action is critical, i.e. results in an unacceptable strains increase or even cracking, by the time it comes to knowledge even worse structural effects than the ones observed will have to be accounted for. Therefore, the decision making process will have to consider not only stopping the construction works but also reversing the latest applied actions.

For that, an in depth previous theoretical study on the situation has to be performed before the works commence which can be later complemented with the real-time monitoring of the structure.

7.1.2. Displacement computation

All in all, the theory developed in section 5 seems to provide reasonable results regarding the computed convergences. Indeed, in a 2017 thesis [76], the same theory was applied to compute the convergence that a laboratory beam developed under certain loads while being monitored by DOFS. The results of that experiment already provided proof that the theory works and produces accurate results when the right assumptions are made.

The application of the theory and the Navier-Bresse equations to the case study required complex particularizations that were presented in Section 5. In order to adapt the available data to the theory, some assumptions had to be made regarding the structural conditions of the tunnel, for instance, the neutral fiber of the concrete segments used to compute the curvature of each section.

Additionally, the boundary conditions that had to be considered to obtain the real tendencies were not very clear. Therefore, if this method is to be a generalized convergence computation tool, the definition of conditions has to be improved, either through additional onsite measurements that provide proof of them or detailed theoretical models that reproduce all the structural elements involving the case. These additional controls could also provide the required exactitude regarding structural variations to test the performed convergence computations.

Since the monitoring scheme was not aimed at convergence computation when it was designed it is more than understandable that the considerations regarding boundary conditions attainment were not taken. Perhaps, a better performance of the developed displacements computation would be achieved if the transversal section was monitored entirely, i.e. with the initial and final points coinciding in the same locations. Currently, they are separated by 1.2m, but if the later were the case, it could be truly considered that the coinciding initial and final points had the same displacements and rotation.

However, the assumptions made are not much of a problem since the exact verification regarding the computed values was not the objective of the thesis but rather testing the particularization of the theory to a generalized tunnel structure and consequently widening the applicability of DOFS.

7.1.3. Tunnel monitoring project

Regarding the monitoring project, two main problems were observed that significantly affected data collection, treatment and interpretation.

As mentioned before, a major drawback of the monitoring project was lack of flexible accessibility for being a metro tunnel holding an operative line. Remote access wasn't possible either due to since no network connection could be provided at the time (that particular metro line segment does not yet include optical fiber network). This led to reading failures happening due to voltage dips, rebooting of the monitoring device or direct electricity disconnection not being detected and to the consequential data loss.

The second problem observed was the lack of cooperation between the implicated parties, i.e. no other company involved in the tunnel or the ground level construction felt responsible for the required monitoring other than Cotca. This led to additional difficulties regarding sensor installation and data acquisition from the executed works at ground level or the maintenance tasks in the tunnel.

However, many positive outcomes were extracted that compensate these two problems. Firstly, the monitoring scheme was very well thought location wise and in terms of monitoring tools choice. Indeed, DOFSs offered a major advantage due to their spatial resolution of 1cm and their almost nonexistent disruption of the tunnel service.

The present case showed that covering structurally differentiable elements doesn't restrict the DOFS performance of the data interpretation. The complex installation process due to surface roughness, presence of joints and magnitude of the structure (the keystone is 5.4m above the slab) did not present unfavourable outcomes regarding data collection other than those dealt with in the data pos-processing section. Additionally, the installation executed in the 4th October hasn't required for any maintenance procedures yet, limiting the personnel intervention to data collection. Perhaps in the future, the sensor protection in the reachable areas and discontinuities has to be reinstalled for its degradation in time, but the fiber will hardly be affected being so thin and covered by epoxy.

Opting for such an innovative technique is not common because traditional sensing is always easier to reach and less mistrusted. Thanks to previously executed DOFSs deployments (for example, [49] and [46]), the company has gained experience in this field and technology through the last decade securing the successful outcome of the present and very much probable future projects involving this type of sensors.

7.2. *DOFS technology applied on real structures*

An introductory review on the fundamentals and application of DOFSs in civil engineering has been presented in this thesis and, together with the exposed case study, all the referenced publications and many others, it has shown the technical feasibility of applying DOFS to perform structural monitoring cannot be doubted.

The possibility of obtaining readings that are continuous in the space is the main advantage that DOFSs offers over other sensing technologies. Additionally, the existence of differentiable types of distributed sensors regarding spatial resolution and range allows their diversifiable applicability depending on the requirements of each SHM project. Ranging from large civil engineering infrastructure such as bridges, dams and tunnels to historical buildings and concrete

cooling towers, their versatility is rather impressive. Sensors like BOTDA can be used to cover long span structures and assess their global behaviour and others with higher spatial resolution, such as the ones based in OFDR technique, can be used to quantify more particular structural damage. However, as mentioned in [11] the fact that these sensors can be deployed in such different applications stresses the importance of adapting the system to each solution. The choice of the best and most cost-effective sensing technique for a project has to be done after serious consideration of some parameters such as size of the structure, acquisition speed, desired spatial resolution, among others.

Even though considering their advantageous performance, DOFSs still constitute a recent technology and their reliability and accuracy when applied to real world structures is still under probation. However, optical fiber sensing has and is experiencing an exponential increase of interest and, consequently, several studies and applications have been presented in the last decade covering this topic. Additionally, structures in the projecting phase are starting to consider the early implementation of such sensors ([14], [61], [77]) leading to a further recognition and improvement of the technology.

7.3. SHM

SHM practice has become, during the past decades, of higher importance regarding many fields of engineering. Understood as a damage detection strategy, SHM can be implemented in many different ways and for diverse motives. When deployed correctly, it can only lead to cost-effective outcomes.

After presenting this concept in the introduction and developing this thesis around it the following conclusions were extracted from it:

- The need to perform such monitoring is based on the enormous economic and life-safety benefits that this concept has the potential to offer.
- SHM strategies need to be incorporated at the design stage so that all involved structures whose behaviour is uncertain can be controlled during construction and in-service.
- The design has to allow for access to sensors preferably non-restrictively, so that the correct operation of those can be checked at all times.
- Measures of structural performance (in the form of limit strains or displacements for example) should be stated previous to the monitoring phase to help with decision making during all stages: choice of sensors, definition of monitoring scheme and its resolution, choice of maintenance and repairing procedures, etc.

7.4. Further research proposal

On the one hand and regarding the case study, further research could be developed regarding the magnitude of the strain readings. This could be done through a comparison of the measurements with more exact theoretical models regarding:

- Geometry: for example, through a 3-Dimensional Finite Element model,

- Material characteristics: with better knowledge of the soil characteristics, the tunnel structure, the interface between soil and concrete lining and
- Loads applied during construction process: with an accurate and real-time description of the works performed at ground level.

Additional monitoring tools installed in the tunnel could also be useful regarding the verification of the DOFS measurements.

The mentioned additional controls would provide also a better knowledge of the structural conditions that would allow for the improvement of the developed convergence computation theory. Distributed Optical Fiber Sensing would clearly benefit from such application considering the current tendency of tunnelling activity and the increasing demands on modern transport networks and that it can be extrapolated to almost every kind of structure.

The proposed data post processing methodology has room for improvement if detection tools for SRAs are developed. This is, in general, a significantly undeveloped topic in the DOFS field and, while the sensor technology is not perfected to avoid such unexplainable peaks, there should be tools that allow for real data interpretation.

In general, standardized guidelines need to be developed to ensure success in every DOFSs deployment regarding, fiber bonding to the structure, temperature affections on readings, SRAs, among other factors. This technology can still be considered as a newly developed / under research field since there is still room for improvement and for widening their applicability. However, Distributed Optical Fiber Sensors are anticipated to have a very important role in Structural Health Management in the near future if correctly understood and developed.

8. References

- [1] J. M. W. Brownjohn, "Structural health monitoring of civil infrastructure," *J. Philosophical Trans. A Math. Phys. Eng. Sci.*, vol. 365, no. 1851, pp. 589–622, 2006.
- [2] VII Framework Programme, "MAINLINE project," 2016.
- [3] "Mianus River Bridge Collapses - Today in History: June 28." [Online]. Available: http://www.klasslooch.com/injaka_bridge_collapse.htm. [Accessed: 04-Jun-2019].
- [4] Klass Koch Associates, "Injaka bridge." [Online]. Available: http://www.klasslooch.com/injaka_bridge_collapse.htm. [Accessed: 04-Jun-2019].
- [5] W. R. De Sitter, "Costs of service life optimization 'The Law of Fives,'" (CEB Bulletin d'information; Vol. 152). Comité Euro-International du Béton, Copenhagen, Denmark, May 18-20, 1983, 1984.
- [6] Ministry of Ontario, "Building together - Guide for municipal asset management plans," 2014. [Online]. Available: <https://www.ontario.ca/page/building-together-guide-municipal-asset-management-plans#section-2>. [Accessed: 07-Jun-2019].
- [7] J. T. P. Housner, G. W., Bergman, L. A., Caughey, T. K., Chassiakos, A. G., Claus, R. O., Masri, S. F., Skelton, R. E., Soong, T. T., Spencer, B. F., Yao, "Structural control: Past, present and future," *J. Eng. Mech.*, vol. 123, no. 9, pp. 897–971, 1997.
- [8] R. M. Matthews, S. L., Moss, "In-service structural monitoring a state-of-the-art review," *Struct. Eng.*, vol. 73, pp. 23–31, 1995.
- [9] A. Mita, "Emerging needs in Japan for health monitoring technologies in civil and building structures," in *2nd International Workshop on Structural Health Monitoring*, 1999.
- [10] M. Baker, "Sensors power next-generation SHM," *Sherbone Sensors*, 2014. [Online]. Available: <http://www.sensorland.com/HowPage131.html>. [Accessed: 04-Jun-2019].
- [11] A. Barrias, J. R. Casas, and S. Villalba, "A review of distributed optical fiber sensors for civil engineering applications," *Sensors (Switzerland)*, vol. 16, no. 5, 2016.
- [12] K. Loupos *et al.*, "Fiber Sensors Based System For Tunnel Linings' Structural Health Monitoring," *2nd Conf. Smart Monit. Assess. Rehabil. Civ. Struct.*, pp. 9–11, 2013.
- [13] J. Dunnycliff, "Geotechnical instrumentation for monitoring field performance," 1982.
- [14] C. B. Barbosa *et al.*, "Fiber Bragg grating system for continuous large-scale monitoring of convergence in Rossio Tunnel," *20th Int. Conf. Opt. Fibre Sensors*, vol. 7503, no. August 2014, p. 75035S, 2009.
- [15] A. Piccolo, Y. Lecieux, D. Leduc, F. Bumbieler, P. Teixeira, and J. Zghondi, "Tunnel convergence analysis by distributed optical fiber strain sensing with means of finite element – inverse analysis method," no. December, pp. 1–12, 2018.
- [16] J. Yu, J. R. Standind, R. Vollum, and D. Potts, "Tunneling induced strains and deformations at Central Line," in *Crossrail Project: Infrastructure design and construction*, ICE Publishing, 2015, p. 271,499.
- [17] W. Wang, W. Zhao, L. Huang, V. Vimarlund, and Z. Wang, "Applications of terrestrial laser scanning for tunnels: a review," *J. Traffic Transp. Eng. (English Ed.)*, vol. 1, no. 5, pp. 325–337, 2014.

- [18] G. Bossi, L. Schenato, and G. Marcato, "Structural Health Monitoring of a Road Tunnel Intersecting a Large and Active Landslide," *Appl. Sci.*, vol. 7, no. 12, p. 1271, 2017.
- [19] Geotechnisches Ingenieurbüro and P. F. und P. GmbH, "Displacement measurements," 2004. [Online]. Available: <https://gif-ettlingen.eu/en/geotechnical-instruments/displacement-measurements/>. [Accessed: 04-Jun-2019].
- [20] G. Rodríguez Guitiérrez, "Monitorización de estructuras de hormigón mediante sensores de fibra óptica distribuida.," Ph.D. Thesis, Universitat Politècnica de Catalunya, 2017.
- [21] M. Kaloop, E. Elbeltagi, J. Hu, and A. Elrefai, "Recent Advances of Structures Monitoring and Evaluation Using GPS-Time Series Monitoring Systems: A Review," *ISPRS Int. J. Geo-Information*, vol. 6, no. 12, p. 382, 2017.
- [22] M. R. Jahanshahi, S. F. Masri, and G. S. Sukhatme, "Multi-image stitching and scene reconstruction for evaluating defect evolution in structures," *Struct. Heal. Monit.*, vol. 10, no. 6, pp. 643–657, 2011.
- [23] S. Maddison, "Structural Monitoring in Tunnels using a novel Wireless System," *Imp. Eng.*, no. 20, 2014.
- [24] F. Ariznavarreta-Fernández, C. González-Palacio, A. Menéndez-Díaz, and C. Ordoñez, "Measurement system with angular encoders for continuous monitoring of tunnel convergence," *Tunn. Undergr. Sp. Technol.*, vol. 56, pp. 176–185, 2016.
- [25] D. Balageas, C. P. Fritzen, and A. Güemes, "Introduction to Structural Health Monitoring," in *Structural Health Monitoring*, ISTE, 2006.
- [26] E. Udd and W. B. Spillman Jr., *Fiber Optic Sensors: An Introduction for Engineers and Scientists*, 2nd ed. John Wiley & Sons: Hoboken, NJ, USA, 2011.
- [27] J. M. López-Higuera, L. R. Cobo, A. Q. Incera, and A. Cobo, "Fiber optic sensors in structural health monitoring," *J. Light. Technol.*, vol. 29, no. 4, pp. 587–608, 2011.
- [28] J. R. Casas and P. J. S. Cruz, "Fiber Optic Sensors for Bridge Monitoring," *J. Bridg. Eng.*, vol. 8, no. 6, pp. 362–373, 2003.
- [29] X. W. Ye, Y. H. Su, and J. P. Han, "Structural health monitoring of civil infrastructure using optical fiber sensing technology: A comprehensive review," *Sci. World J.*, vol. 2014, 2014.
- [30] G. Rodriguez, J. R. Casas, and S. Villalba, "SHM by DOFS in civil engineering: a review," *Struct. Monit. Maint.*, vol. 2, no. 4, pp. 357–382, 2015.
- [31] FOSCO. Fiber Optics For Sale CO., "Optical fiber tutorial: How optical fiber works," 2019. [Online]. Available: <https://www.fiberoptics4sale.com/blogs/archive-posts/95146054-optical-fiber-tutorial-optic-fiber-communication-fiber>. [Accessed: 05-Jun-2019].
- [32] S. Villalba and J. R. Casas, "Application of optical fiber distributed sensing to health monitoring of concrete structures," *Mech. Syst. Signal Process.*, vol. 39, no. 1–2, pp. 441–451, 2013.
- [33] H. Guo, G. Xiao, N. Mrad, and J. Yao, "Fiber optic sensors for structural health monitoring of air platforms," *Sensors*, vol. 11, no. 4, pp. 3687–3705, 2011.
- [34] B. H. Lee *et al.*, "Interferometric Fiber Optic Sensors," *Opt. Fiber Sensors Adv. Tech. Appl.*, pp. 37–78, 2017.

- [35] M. Abolbashari, A. S. Gerges, and F. Farahi, "A combined fiber Bragg grating and interferometric based sensor," *20th Int. Conf. Opt. Fibre Sensors*, vol. 7503, no. October, 2009.
- [36] S. Michelsen, "Optical fiber grating based sensors," Ph.D. Thesis, DTU Orbit, 2003.
- [37] C. E. Campanella, A. Cuccovillo, C. Campanella, A. Yurt, and V. M. N. Passaro, "Fibre Bragg Grating based strain sensors: Review of technology and applications," *Sensors (Switzerland)*, vol. 18, no. 9, 2018.
- [38] M. D. Todd, G. A. Johnson, and S. T. Vohra, "Deployment of a fiber bragg grating-based measurement system in a structural health monitoring application," *Smart Mater. Struct.*, vol. 10, no. 3, pp. 534–539, 2001.
- [39] A. Barrias, J. R. Casas, and S. Villalba, "Embedded distributed optical fiber sensors in reinforced concrete structures - A case study," *Sensors (Switzerland)*, vol. 18, no. 4, pp. 1–22, 2018.
- [40] R. C. Tennyson, A. A. Mufti, S. Rizkalla, G. Tadros, and B. Benmokrane, "Structural health monitoring of innovative bridges in Canada with fiber optic sensors," *Smart Mater. Struct.*, vol. 10, no. 3, pp. 560–573, 2001.
- [41] LUNA Technologies, "ODiSI-A Optical Distributed Sensor Interrogator (Users Guide)," 2013. [Online]. Available: <http://lunainc.com/wp-content/uploads/2014/05/ODiSI-A-Users-Guidev1.2.pdf>. [Accessed: 04-May-2019].
- [42] A. Güemes, A. Fernández-López, and B. Soller, "Optical fiber distributed sensing - physical principles and applications," *Struct. Heal. Monit.*, vol. 9, no. 3, pp. 233–245, 2010.
- [43] N. de Battista, R. Harvey, and N. Cheal, "Distributed fibre optic sensor system to measure the progressive axial shortening of a high-rise building during construction," in *39th IABSE Symposium - Engineering the Future*, 2017.
- [44] A. Brault, S. Nurmi, and N. A. Hoult, "Distributed Deflection Measurement of Reinforced Concrete Elements Using Fibre Optic Sensors," in *39th IABSE Symposium - Engineering the Future*, 2017.
- [45] M. Weisbrich and K. Holschemacher, "Comparison between different fiber coatings and adhesives on steel surfaces for distributed optical strain measurements based on Rayleigh backscattering," *J. Sensors Sens. Syst.*, vol. 7, no. 2, pp. 601–608, 2018.
- [46] A. Barrias, G. Rodriguez, J. R. Casas, and S. Villalba, "Application of distributed optical fiber sensors for the health monitoring of two real structures in Barcelona," *Struct. Infrastruct. Eng.*, vol. 14, no. 7, pp. 967–985, 2018.
- [47] M. F. Bado, G. Kaklauskas, and J. R. Casas, "Performance of Distributed Optical Fiber Sensors and Digital Image Correlation in the monitoring of RC structures."
- [48] M. F. Bado, J. R. Casas, and A. Barrias, "Performance of rayleigh-based distributed optical fiber sensors bonded to reinforcing bars in bending," *Sensors (Switzerland)*, vol. 18, no. 9, 2018.
- [49] J. Casas, S. Villalba, and V. Villalba, "Management and Safety of Existing Concrete Structures via Optical Fiber Distributed Sensing," in *Maintenance and Safety of Aging Infrastructure. Structures and Infrastructures Book Series, Vol. 10*, CRC Press Taylor & Francis Group, Ed. 2014, pp. 217–245.

- [50] A. Michou, A. Hilaire, F. Benboudjema, G. Nahas, P. Wyniecki, and Y. Berthaud, "Reinforcement-concrete bond behavior: Experimentation in drying conditions and meso-scale modeling," *Eng. Struct.*, vol. 101, pp. 570–582, 2015.
- [51] M. Mehdi Mirzazadeh and M. F. Green, "Fiber Optic Sensors and Digital Image Correlation for Measuring Deformations in Reinforced Concrete Beams," *J. Bridg. Eng.*, vol. 23, no. 3, p. 04017144, 2017.
- [52] D. Inaudi and B. Glisic, "Application of distributed Fiber Optic Sensory for SHM," in *2nd International Conference on SHMII*, 2006, pp. 163–172.
- [53] L. Thévenaz, M. Facchini, A. Fellay, P. Robert, D. Inaudi, and B. Dardel, "Monitoring of large structure using distributed Brillouin fibre sensing," in *Proceedings of the Optical Fiber Sensors OFS 13 Conference*, 1999.
- [54] B. Glisic, J. Chen, and D. Hubbell, "Streicker Bridge: A comparison between Bragg-grating long-gauge strain and temperature sensors and Brillouin scattering-based distributed strain and temperature sensors," in *Proceedings of SPIE*, 2011.
- [55] B. Glisic and D. Inaudi, "Development of method for in-service crack detection based on distributed fiber optic sensors," *Struct. Heal. Monit.*, vol. 11, no. 2, pp. 161–171, 2012.
- [56] B. I. N. Shi, H. Sui, J. I. E. Liu, and D. A. N. Zhang, "The BOTDR-based distributed monitoring system for slope engineering engineering," in *Proceedings of the 10th IAEG International Congress, Nottingham, UK*, 2006, no. December, pp. 6–10.
- [57] M. Iten, "Novel Applications of Distributed Fiber-optic Sensing in Geotechnical Engineering," Ph.D. Thesis, ETH Zurich, 2011.
- [58] P. Rajeev, J. Kodikara, W. K. Chiu, and T. Kuen, "Distributed Optical Fibre Sensors and their Applications in Pipeline Monitoring," *Key Eng. Mater.*, vol. 558, pp. 424–434, 2013.
- [59] C. Y. Gue, M. Wilcock, M. M. Alhaddad, M. Z. E. B. Elshafie, K. Soga, and R. J. Mair, "The monitoring of an existing cast iron tunnel with distributed fibre optic sensing (DFOS)," *J. Civ. Struct. Heal. Monit.*, vol. 5, no. 5, pp. 573–586, 2015.
- [60] N. Tachibana, Y. Kojima, T. Nakayama, and M. Tanabe, "Tunnel Monitoring System using Optical Fiber Sensor or Electric Conductible Paint," *Assiut J. Environ. Stud.*, p. 43, 2001.
- [61] M. Fajkus, J. Nedoma, P. Mec, E. Hrubesova, R. Martinek, and V. Vasinek, "Analysis of the highway tunnels monitoring using an optical fiber implemented into primary lining," *J. Electr. Eng.*, vol. 68, no. 5, pp. 364–370, 2017.
- [62] A. B. Huanga, J. T. Lee, C. C. Wang, Y. T. Ho, and T. S. Chuang, "Field Monitoring Of Shield Tunnel Lining Using Optical Fiber Bragg Grating Based Sensors," in *Proceedings of the 18th International Conference on Soil Mechanics and Geotechnical Engineering*, 2013, pp. 681–686.
- [63] L. W. V. LLC, "2019 Distributed and Single Point Fiber Optic Sensing Systems Forecast. A Photonic Sensor Consortium Market Survey Report," 2019.
- [64] Google and Institut Cartogràfic de Catalunya, "Imagery Google. Map data," 2019. [Online]. Available: <https://www.google.com/maps>. [Accessed: 10-Jun-2019].
- [65] Grup TMB, "Millores a la xarxa. Metro automàtic. Quines línies són?," 2019. [Online]. Available: <https://www.tmb.cat/ca/sobre-tmb/millores-xarxa-transport/metro->

automatic/quines-linies-son. [Accessed: 10-Jun-2019].

- [66] D. Guerrero, “El tramo central de la línea 9 de metro prepara su reactivación,” *La Vanguardia*, Barcelona, 2018.
- [67] D. Vicario Lara, “Obras de construcción de la Línea 9 del Metro de Barcelona. Tramo 4B. Sagrera-Gorg,” *Rev. Obras Públicas*, no. 3447, pp. 25–31, 2004.
- [68] MathWorks, “MATLAB.” .
- [69] A. Barrias, J. R. Casas, and S. Villalba, “Application study of embedded Rayleigh based Distributed Optical Fiber Sensors in concrete beams,” *Procedia Eng.*, vol. 199, no. 2017, pp. 2014–2019, 2017.
- [70] Z. Ding *et al.*, “Distributed optical fiber sensors based on optical frequency domain reflectometry: A review,” *Sensors (Switzerland)*, vol. 18, no. 4, pp. 1–31, 2018.
- [71] K. C. Lin and C. W. Lin, “Finite deformation of 2-D laminated curved beams with variable curvatures,” *Int. J. Non. Linear. Mech.*, vol. 46, no. 10, pp. 1293–1304, 2011.
- [72] S. Laroze, *Mécanique des structures. Tome 2: Poutres*. Paris, 1974.
- [73] C. Navarro, “Capítulo 2. Conceptos básicos del cálculo estructural (Curso en Ingeniería Estructural),” Departamento de Mecánica de Medios Continuos y Teoría de Estructuras, Universidad Carlos II de Madrid, 2009.
- [74] J. M. Canet, *Resistencia de Materiales y Estructuras*. Barcelona, 2012.
- [75] CIMNE, “GiD.” .
- [76] A. Secanell, “Determinació de desplaçament a partir de sensors continus de fibra òptica. Aplicació als ponts,” Universitat Politècnica de Catalunya, 2017.
- [77] L. Mosser, “Puente entre Francia y Reino Unido,” Universitat Politècnica de Catalunya, 2019.

Annexes

Annex 1. Site pictures

A1.1. Transversal monitoring (50-23m)

A1.2. Longitudinal monitoring (23-0m)

Annex 2. Fiber layout

A2.1. Building and tunnel

A2.2. Tunnel cross section

A2.3. Tunnel plan and elevation view

A2.4. Tunnel 3-D view

Annex 3. Model timeline

Annex 4. Matlab codes